X-ray Phase Contrast 3D virtual histology: evaluation of lung alterations after micro-beam irradiation

Mariele Romano M.Sc. , Dr. Alberto Bravin , Dr. Michael D. Wright , Laurent Jacques M.Sc. , Dr. Arttu Miettinen , Dr. Ruslan Hlushchuk , Julien Dinkel M.D. , Dr. Stefan Bartzsch , Jean Albert Laissue M.D. , Valentin Djonov M.D. , Dr. Paola Coan

PII: S0360-3016(21)02914-X
DOI: https://doi.org/10.1016/j.ijrobp.2021.10.009
Reference: ROB 27317

To appear in: *International Journal of Radiation Oncology, Biology, Physics*

Received date: 1 April 2021
Revised date: 20 September 2021
Accepted date: 5 October 2021

Please cite this article as: Mariele Romano M.Sc. , Dr. Alberto Bravin , Dr. Michael D. Wright , Laurent Jacques M.Sc. , Dr. Arttu Miettinen , Dr. Ruslan Hlushchuk , Julien Dinkel M.D. , Dr. Stefan Bartzsch , Jean Albert Laissue M.D. , Valentin Djonov M.D. , Dr. Paola Coan , X-ray Phase Contrast 3D virtual histology: evaluation of lung alterations after micro-beam irradiation, *International Journal of Radiation Oncology, Biology, Physics* (2021), doi: https://doi.org/10.1016/j.ijrobp.2021.10.009

XPCI-CT virtual histology on lungs after MRT

X-ray Phase Contrast 3D virtual histology: evaluation of lung alterations after micro-beam irradiation

Short running title: XPCI-CT virtual histology on MRT-treated lungs

M.Sc. Mariele Romano[1], Dr. Alberto Bravin[2+], Dr. Michael D. Wright[3], M.Sc. Laurent Jacques[1], Dr. Arttu Miettinen[4,5++], Dr. Ruslan Hlushchuk[6], M.D. Julien Dinkel[7], Dr. Stefan Bartzsch[8,9], M.D. Jean Albert Laissue[6], M.D. Valentin Djonov[6], Dr. Paola Coan[1,7]

[1] *Faculty of Physics, Ludwig Maximilian University, Am Coulombwall 1, München, Garching, Germany;*

[2] *European Synchrotron Radiation Facility, 71 Avenue des Martyrs, Grenoble, France, 38000;*

[3] *Avail Medical Devices is 301 Gibson Dr., Suite 312, Roseville, CA 95678 USA;*

[4] *Institute for Biomedical Engineering, University and ETH Zurich, Zurich, Switzerland;*

[5] *Swiss Light Source, Paul Scherrer Institut, Villigen, Switzerland;*

[6] *Institute of Anatomy, University of Bern, 2 Baltzerstrasse, Bern, Switzerland Department;*

[7] *Department of Clinical Radiology, Faculty of Medicine, Ludwig-Maximilians-Universität München, Munich, Germany;*

[8] *Department of Radiation Oncology, School of Medicine, Technical University of Munich, Klinikum rechts der Isar, Munich, Germany;*

[9] *Helmholtz Centre Munich, Institute for Radiation Medicine, Munich, Germany;*

[+] *Current affiliation: Department of Physics, University of Milano-Bicocca, Milan, Italy*

[++] *Present address: Department of Physics, University of Jyvaskyla, Jyvaskyla, Finland.*

Corresponding author: Prof. Dr. Paola Coan, E-mail: Paola.Coan@physik.uni-muenchen.de

Author responsible for statistical analysis: M.Sc. Mariele Romano, E-mail: Mariele.Romano@physik.uni-muenchen.de

Conflict of Interest Statement:
The biological samples utilized in this study were generated in a previous work funded by Varian Medical Systems, Inc. Author Alberto Bravin at the European Synchrotron Radiation Facility, who was involved in the previous work, declares that a grant from Varian Medical Systems, Inc., to the

ESRF for services related to the housing of animals, realization of *in-vivo* protocols, and use of the X-ray irradiation facility, resulting in the biological samples used in both studies, constitutes a potential conflict of interest. Author Michael D. Wright declares that two U. S. patents related to microbeam radiotherapy issued to him as Inventor and to Varian Medical Systems, Inc., as Assignee constitutes a potential conflict of interest.

M. Romano report grants from Deutsche Forschungsgemeinschaft and non-financial support from Deutsche Forschungsgemeinschaft - GRK2274, during the conduct of the study. P. Coan discloses non-financial support from Deutsche Forschungsgemeinschaft - GRK2274, during the conduct of the study.

L. Jacques, A. Miettinen, R. Hlushchuk, J. Dinkel, S. Bartzsch, J. A. Laissue and V. Djonov have nothing to disclose.

Funding Statement:

This study was supported by the German Research Foundation (DFG) within the Research Training Group GRK2274 which provided a grant for M. Romano.

Data sharing:

Research data are stored in the European Synchrotron Radiation Facility repository and will be shared upon request to the corresponding author.

Acknowledgements:

This study was supported by the German Research Foundation (DFG) within the Research Training Group GRK2274. We would like to thank the SLS for providing the beamtime for the imaging experiments and in particular Christian Matthias Schlepütz, Margie Olbinado and Goran Lovric from the TOMCAT beamline for their support. Authors wish to thank the ESRF for the provision of the beamtime, for the animal irradiation and the BMF for animals housing and care. We would also like to thank Sam Bayat and Luca Fardin from the ESRF for fruitful discussions and Eveline Yao from the University of Bern for the realization of the histologic procedures.

Abstract

Purpose: This study provides the first experimental application of multiscale three-dimensional (3D) X-ray Phase Contrast Imaging Computed Tomography (XPCI-CT) virtual histology for the inspection and quantitative assessment of the late stage effects of radio-induced lesions on lungs in a small animal model.

Methods and Materials: Healthy male Fischer rats were irradiated with X-ray standard broad beams and Microbeam Radiation Therapy (MRT), a high dose rate (14 kGy/s), FLASH spatially-fractionated X-ray therapy to avoid the beamlets smearing due to cardiosynchronous movements of the organs during the irradiation. After organ dissection, *ex-vivo* XPCI-CT was applied to all the samples and the results were quantitatively analysed and correlated to histologic data.

Results: XPCI-CT enables the 3D visualization of lung tissues with unprecedented contrast and sensitivity allowing alveoli, vessels and bronchi hierarchical visualization. XPCI-CT discriminates in 3D radio-induced lesions such as fibrotic scars, Ca/Fe deposits and, in addition, allows a full-organ accurate quantification of the fibrotic tissue within the irradiated organs. The radiation-induced fibrotic tissue content is less than 10% of the analyzed volume for all the MRT treated organs while it reaches the 34% in the case of irradiations with 50 Gy using a broad beam.

Conclusions: XPCI-CT is an effective imaging technique able to provide detailed 3D information for the assessment of lung pathology and treatment efficacy in a small animal model.

Introduction

Accurate methods for monitoring the efficacy of treatments are key in radio-oncology. The aim of this study was to investigate and characterize, for the first time, the effects of both standard and novel radiotherapy (RT) methods using a label-free three-dimensional (3D), *ex-vivo* X-ray imaging-based virtual histology technique. This method provides volumetric high-resolution datasets from tissue samples up to full organs and allows investigating tissue anatomy and pathological states. The current gold standard for an accurate diagnosis on excised tissue, in both preclinical research and clinical routine, is histology (1; 2). Histological investigations are indispensable to identify and classify several types of tissues and pathological states providing a multitude of staining protocols for labelling and recognizing the different structures. However, histology presents also important drawbacks in that (i) it is a destructive macroscopic analysis method, (ii) it is laborious, time demanding and highly relying on skilled operators (3), and (iii) it provides, intrinsically, two-dimensional (2D) information. Histological resolution is only achievable in 2D, while, in the third dimension, the thickness of the cut slice determines the sampling step and thus the spatial resolution (3). In addition, localisation and histological analysis of regions of interest within the specimen are hampered by the poor visibility of the tissue embedded within the paraffin block (4). This limitation can only be overcome with serial sectioning and staining that are, anyhow, very time

consuming. To allow for a more detailed analysis of the tissue, an accurate 3D reconstruction of the volume, based on histological sections, is needed. However, during the slicing phase, tissues can be damaged leading to inhomogeneous deformations and artefacts like tearing, shrinking, stretching or other morphological rearrangement of the tissues (5). Thus, when creating a 3D atlas of an organ by stacking the 2D histological slices, morphological inconsistencies in the reconstructed volume will appear. 3D virtual histology has recently appeared as able to overcome these limitations and provide datasets of images that can be virtually sectioned in any direction. Several so-called virtual histology approaches have recently emerged (1), each with their own limitations: confocal microscopy, light sheet microscopy, micro-magnetic resonance imaging (μMRI) and micro-computed tomography (μCT). Among all, synchrotron X-ray based virtual histology has been shown to provide datasets down to sub-micron isotropic spatial resolution even for soft tissue samples by means of X-ray Phase Contrast Imaging Computed Tomography (XPCI-CT) (6; 7). An overview of the main characteristics of XPCI-CT is presented in the "XPCI-CT" section of the supplementary material.

Over the years, XPCI-CT has been applied to many biomedical cases. Among the different examined tissues, lungs have proved to have characteristics that are particularly suitable to be investigated by XPCI-CT. Lung tissue is ideally suited to XPCI because it consists of air sacs (approximately 80% by volume at end of expiration), separated by thin tissue layers (mainly water) (8). The air–tissue interfaces produce significant phase shifts (i.e. X-ray refraction) and thus small airways are visualized with high contrast despite of their weakly X-ray absorbing power. Small animal lungs have been investigated via XPCI-CT in several applications as dynamic identification of airway liquid clearance in new-born rabbits (9; 8) and quantitative imaging of airway structure and regional lung ventilation with spatial resolution down to ~1.0 μm, allowing *in-vivo* and *ex-vivo* (10) studies in small animal models (11; 12) and in new-born piglets (13).

Lung cancer has been the most common cancer in the world for several decades and still remains among the most frequent types worldwide (11.6% of the total) (14). It is the most frequent cause of death from cancer worldwide, estimated to be responsible for nearly one in five deaths (1.8 million

deaths in 2018 (15) and its survival globally remains low; the 5-year relative survival rate has been estimated to be about 19% in the United States in 2019 (16). For this reason, there is a very high interest in new and more effective treatments for lung cancer and follow-up imaging tools.

In this study, we applied standard broad beam RT and X-ray Microbeam Radiation Therapy (MRT), which delivers synchrotron spatially fractionated, quasi-parallel beamlets produced by means of a multislit collimator that reshapes the original laminar beam into an array of micrometres-wide beamlets with centre-to-centre (c-t-c) distances ranging from hundreds to thousands of micrometres. MRT exploits the dose-volume effect of normal tissue tolerance (17) allowing the delivery of collimated beams of peak doses up to hundreds of Gray, using dose rates of ~14000 Gy/s, (FLASH irradiation (18)) while keeping the valley dose below the tolerance threshold of normal tissues (19). We focussed on the effects of different X-ray beam geometries on healthy rat lungs, being the radio-tolerance of normal tissue the limiting factor of any cancer treatment. A previous proof of concept experiment on a mouse model already showed no acute response after the MRT irradiation with peak doses up to 400 Gy by monitoring physiological parameters and using immunohistochemistry (dose rates between 10700 Gy/s and 13900 Gy/s (20)). Up to now, the potential of XPCI-CT to investigate RT effects has been proven on MRT-treated rat brains. A pilot study successfully visualized by *ex-vivo* XPCI-CT the anatomy of MRT-treated rat brains without administering any contrast agent (21). The effects of microbeam irradiation throughout the target areas were visible as micrometre-thick radiation-induced tissue ablation mainly in the cortex, tissue necrosis and intra-tumour accumulation of iron and calcium deposits. Based on these successful studies, we aimed at establishing XPCI-CT as a 3D imaging technique for the *ex-vivo* follow up study of spatially fractionated X-ray radiotherapy for lung tumour treatment.

The final goal is (i) to visualize and (ii) compare via XPCI-CT the effects of MRT and conventional broad beam (BB) RTs on healthy lung tissue by discriminating the radio induced lesions that are specific of the applied beam geometries and delivered doses as well as (iii) identify, thanks to the

comparison with histology, the limits of XPCI-CT sensitivity to the anatomical alterations induced by the different delivered doses.

Methods and Materials

The lung samples for this study were obtained from an earlier experiment (22) investigating the effect of FLASH-MRT on normal lung tissue. Thirty-three healthy male Fisher rats, weighting approximately 300 g, were used and divided into 11 groups that were either irradiated or left as control group. The irradiation was performed *in-vivo* at the XXX XXX XX of the XXX XXX XX XXX (XXX, XXX, XXX). Animals were then housed and daily monitored until their sacrifice occurred 12 months post-irradiation. Lungs and heart of each animal were dissected out as single block of tissue and immersed into 4% paraformaldehyde in phosphate buffered saline solution for the fixation. Lung organs were finally embedded in paraffin.

All procedures related to animal care conformed to the guidelines of the XXXX government (licenses XXX and YYY), the XXX and were approved by the XXXX Internal Evaluation Committee for Animal Welfare and Rights.

Irradiation

The animal irradiations were performed in the MRT experimental hutch (23) of the XXX beamline delivering three different radiotherapy beam patterns: BB and two MRT settings with different peak doses. The irradiation target was set to 1x1 cm^2 within the right lung with the beam delivered in the antero-posterior direction. In each rat, the identification of the target area was guided by a radiograph delivering ~350 mGy; this procedure allowed sparing vital organs in the surroundings like liver, heart and spinal cord. During the beam centring and irradiation procedures, animals were anesthetized by isoflurane inhalation (5%) followed by an intraperitoneal injection xylazine/ketamine (64.5/5.4 mg/kg). For the irradiation, animals were placed on a stereotactic frame (24) and connected to a respirator to control the breathing and to arrest the organ motion during

the beam delivery. The animals of the 11 groups received, in a single fraction, a treatment according to Table 1.

The beam reshaping for MRT_{50} and MRT_{500} cases was achieved by using a custom made multislit collimator (25) delivering respectively 25 and 3 microbeams within the irradiation field. The radiotherapy beam spectrum was characterised by a peak energy of 81 keV, a mean energy of 107 keV and a 14 kGy/s maximum dose rate.

XPCI-CT imaging experiment

The XPCI µ-CT experiment was performed at the XXXX - XXX beamline (26; 27) of the XXX XXX XXX in XXX, XXX. A propagation-based phase contrast CT setup was used to image *post-mortem* the 33 paraffin embedded lung samples. X-ray photons, coming from a 2.9 T superbend source, were filtered by a fixed-exit double crystal multilayer monochromator allowing the sample to be illuminated by a 20 keV quasi-coherent monochromatic beam.

The sample was placed on a remotely controlled, automatized system that allows for sample centring, movement and alignment with the detector. For every CT scan, 20 electronic noise images, 50 reference (beam) images and 1801 angular projections over 180º were recorded by a PCO.Edge 5.5 camera equipped with a 20 µm thick LuAG:Ce scintillator screen and UPLAPO4x/UPLAPO10x microscopes with sample to detector distances of 20 and 5 cm, respectively. The two magnifications lead to 1.63^3 and 0.65^3 μm^3 isotropic voxel sizes. For every sample a mosaic image was obtained by acquiring a grid of nxm 1.63^3 μm^3 voxel size micro-CTs distributed in the horizontal plane (parallel to the beam direction) that were subsequently reconstructed and stitched together by using the NRStitcher software (28) resulting in a high-resolution wide-field tomographic dataset. Each pair of subsequent CT dataset where acquired with an overlap of 15%, allowing a good match of the structures on the borders: e.g. a 2x2 stitching procedure gives a 7.2x7.2 mm^2 CT image. A single 1.63 μm^3 voxel-size CT image has a field of view (FOV) of 4.2x4.2 mm^2 thus, the n and m values for the

stitched procedure were evaluated and decided for each sample, according to its horizontal dimensions. One CT stage (corresponding to a 3.35 mm vertical FOV, i.e. perpendicular to the beam direction) was sufficient to cover the full sample thickness. The 10x magnification microscope was used to image selected features of interest within the examined tissues. Details on the image processing and analysis methodologies are given in the supplementary material “Methods” section.

Results

XPCI-CT for healthy lung anatomy

The capability of XPCI-CT to depict lung anatomic detail with high sensitivity is shown in the 1.63^3 μm^3 – voxel images of two control (healthy, non-irradiated) rat samples (

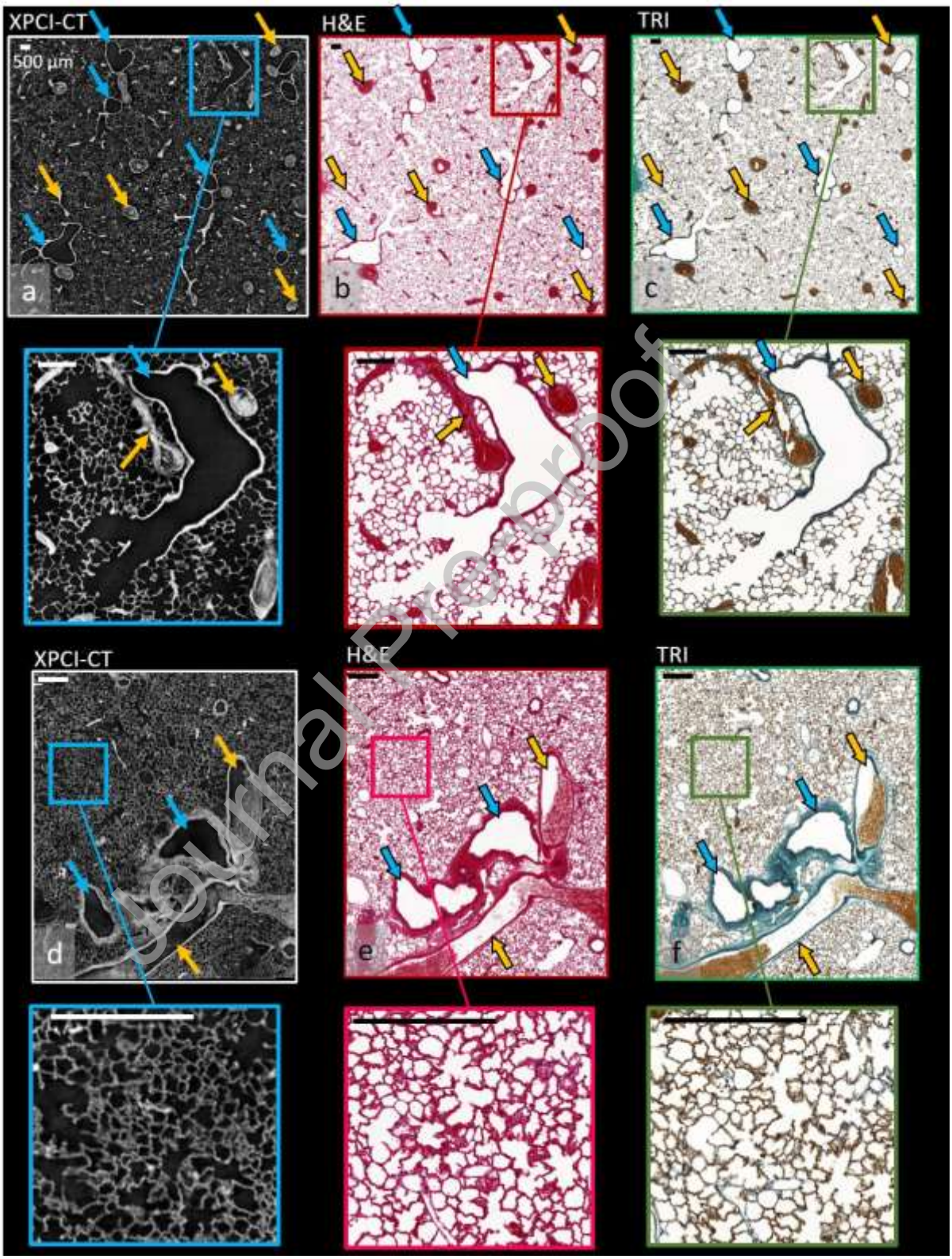

Figure **1**). The comparison between XPCI-CT and Haematoxylin and Eosin (H&E) and Masson-Goldner trichrome (TRI) stainings allows a validation of the structures visualized with XPCI-CT. Small variations between the structures visible in XPCI-CT and histology images are due to the histologic cutting procedures and a possible angular misalignment between the two slices. In the 1.63^3 μm^3 –

voxel XPCI-CT coronal image (

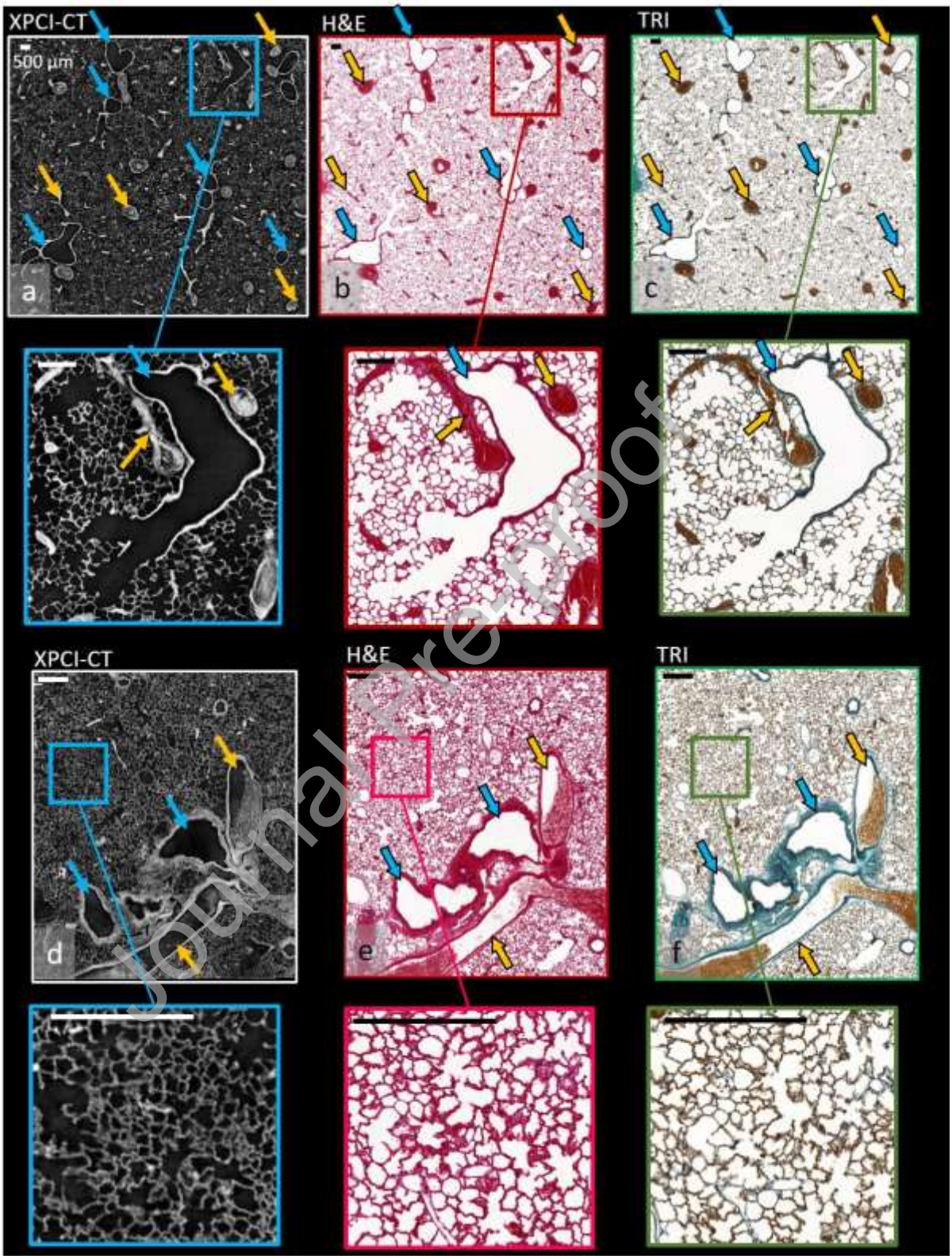

Figure **1**a), the uniform alveolarization of the tissue with regular septa is clearly visualized and blood vessels (yellow arrows, as in all figures) and airways (sky-blue arrows, as in all figures) of different

dimensions are depicted, as validated by histology (

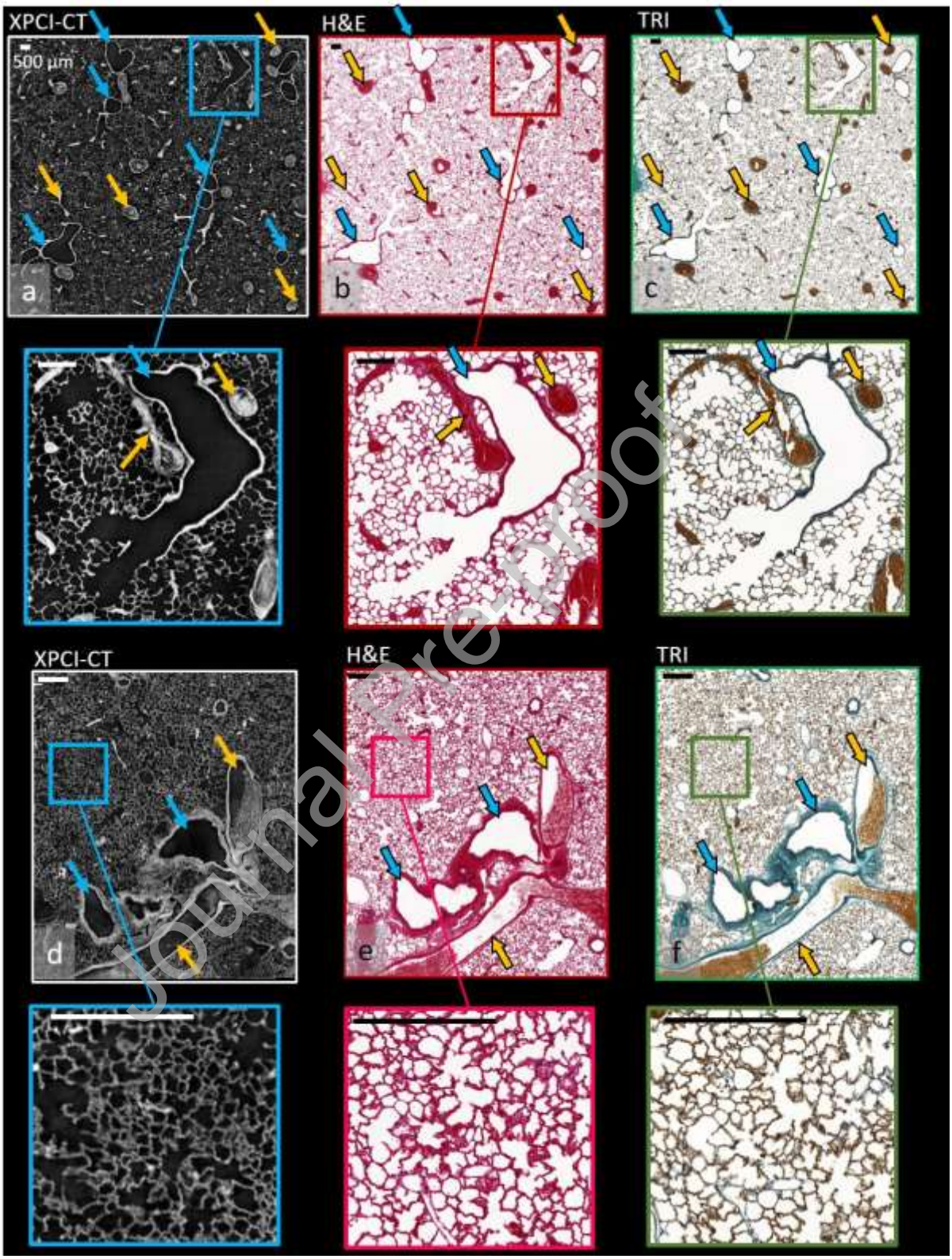

Figure 1b-c) confirming the absence of pathological signs. At different anatomical levels, based on the appearance of their inner surface, the XPCI-CT technique can distinguish between blood vessels

(smooth walls) and airways (wrinkled walls). This can be seen in the insets of

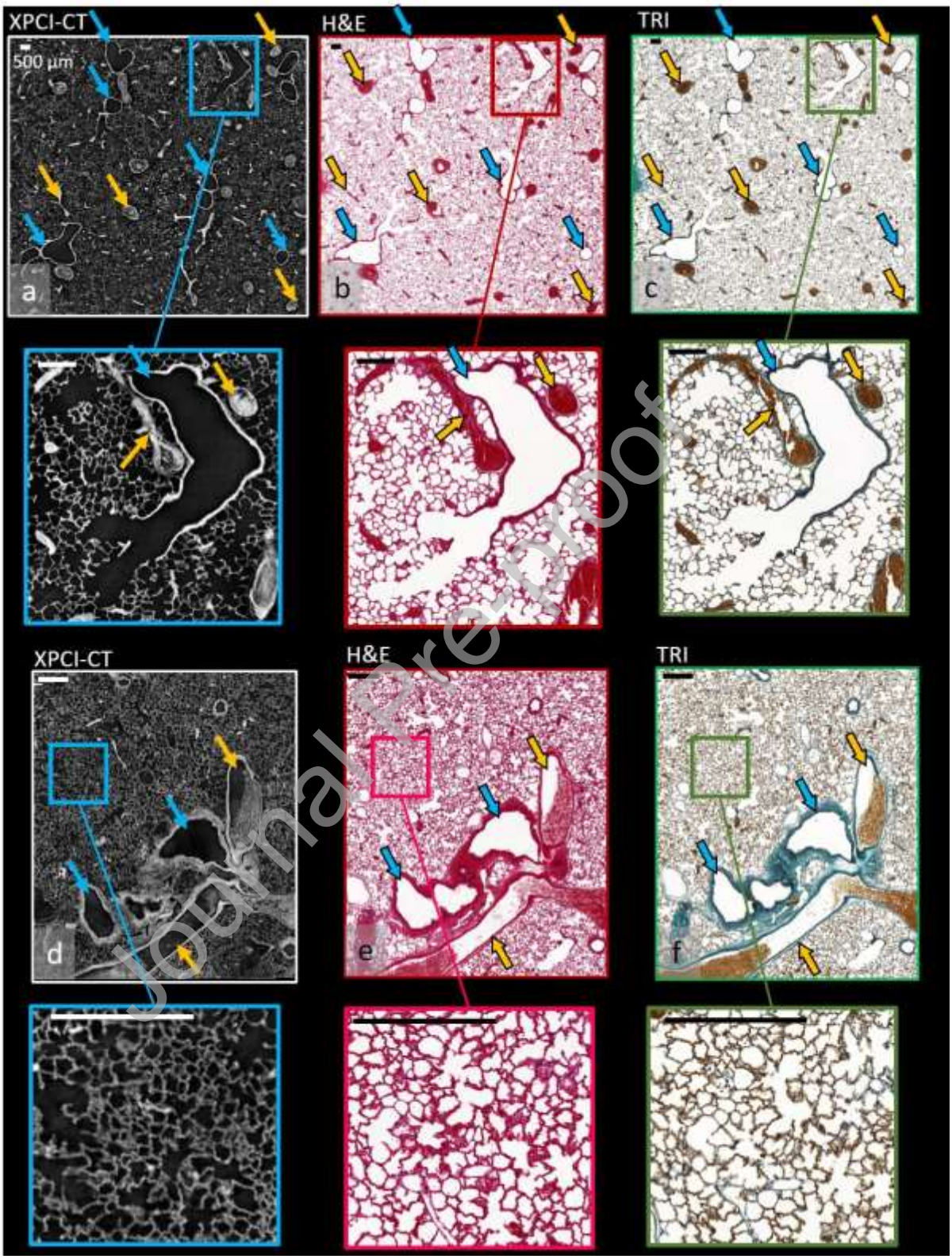

Figure 1a-c, where the development of a bronchiole into alveolar duct and alveolar acini is presented next to a blood vessel. Blood filled vessels appear in XPCI-CT as bright structures and are intense red

in H&E images (

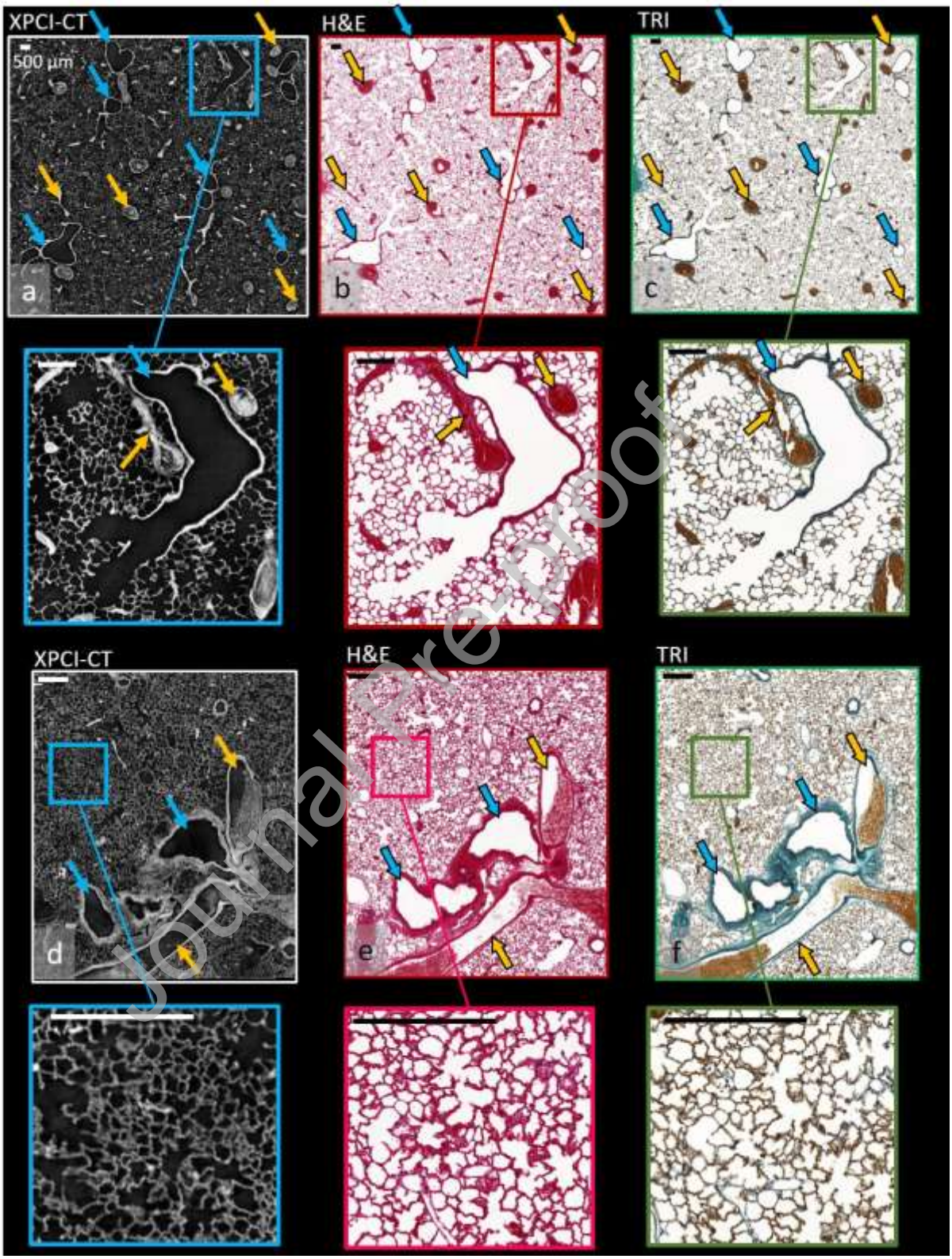

Figure 1b) while airways appear to be empty cavities with green walls in TRI images (

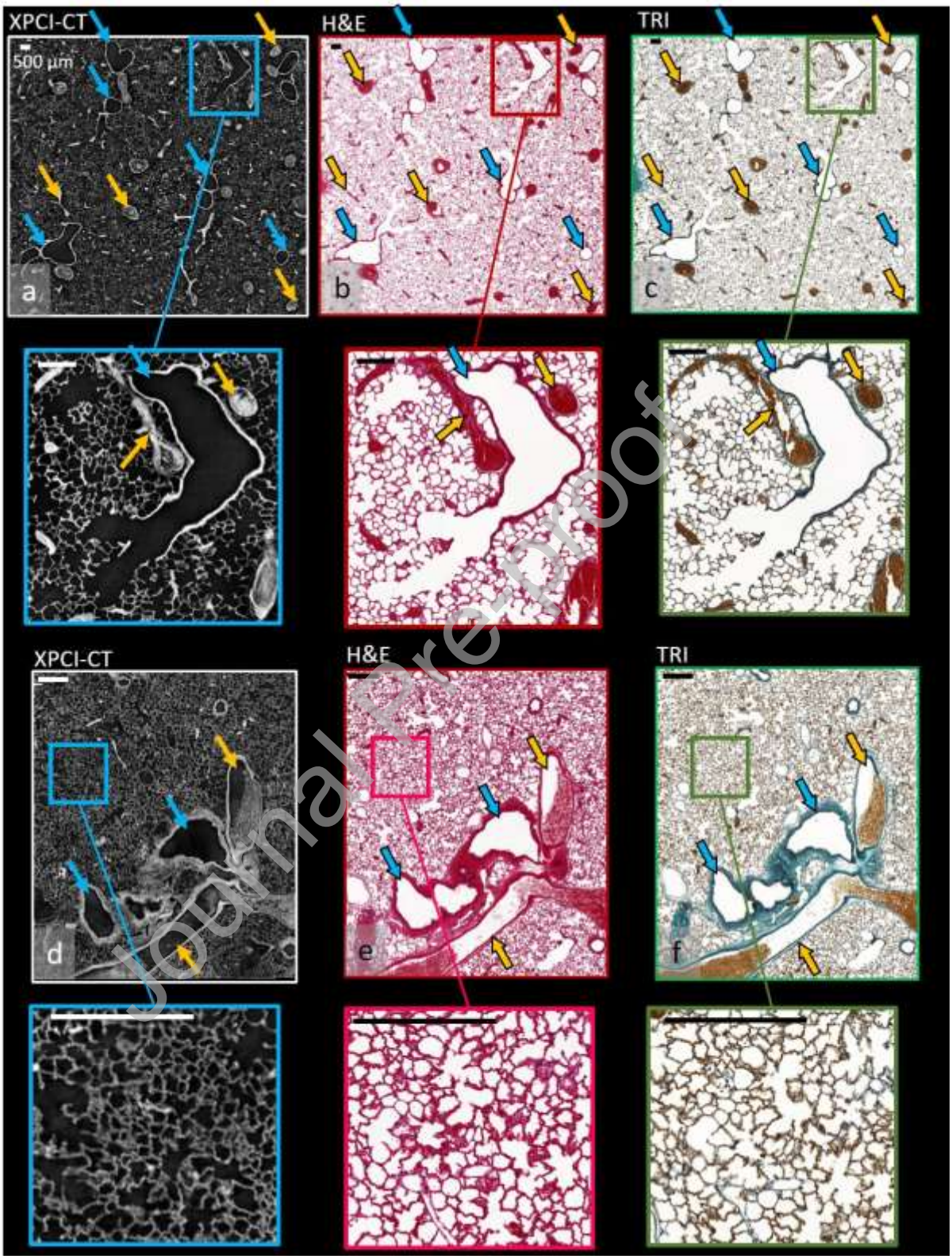

Figure 1c). Generally, vessels are blood filled since no perfusion was applied before euthanasia, while airways are paraffin filled.

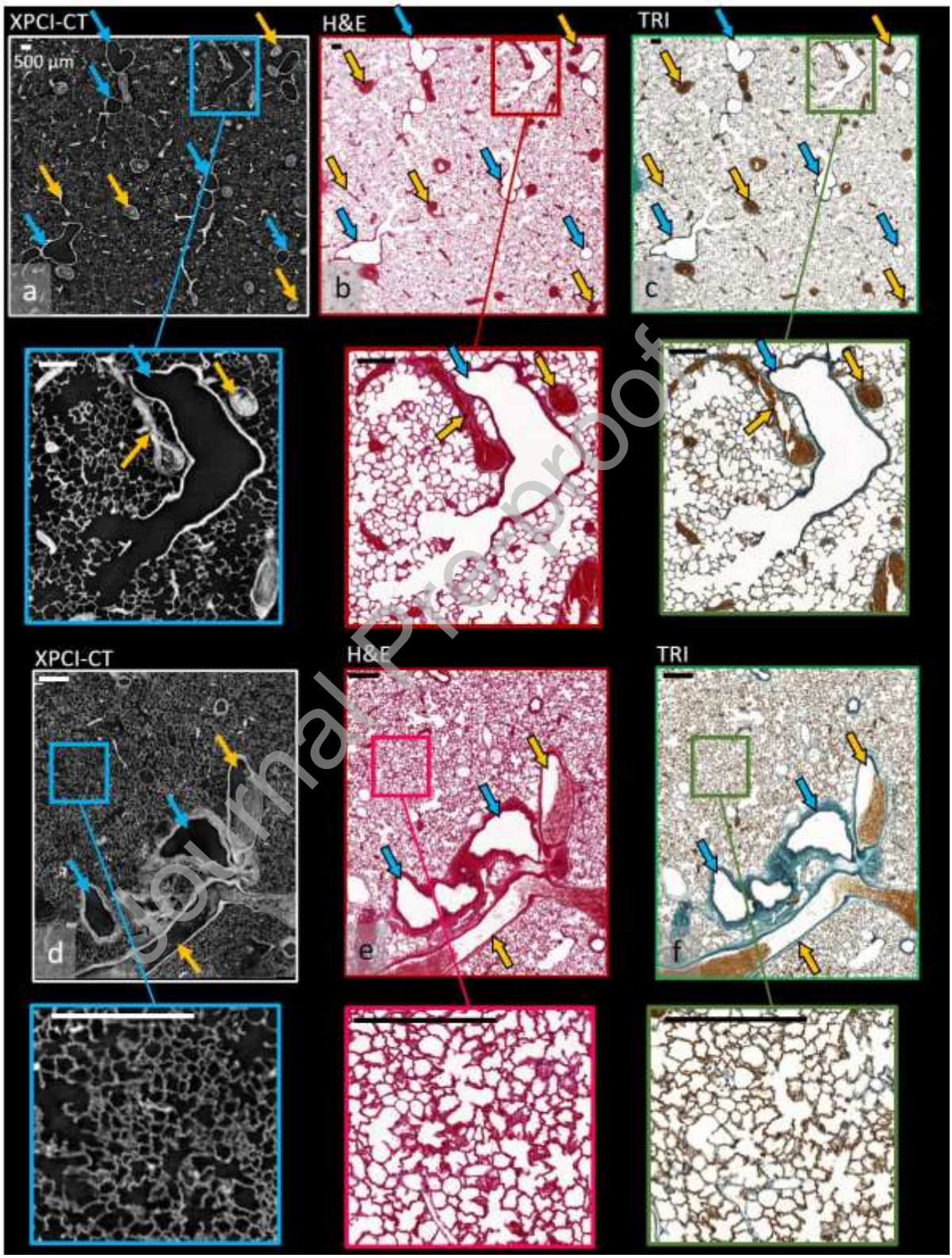

Figure **1**d shows a portion of a 1.63^3 μm^3 – voxel XPCI-CT coronal image of another control lung tissue and

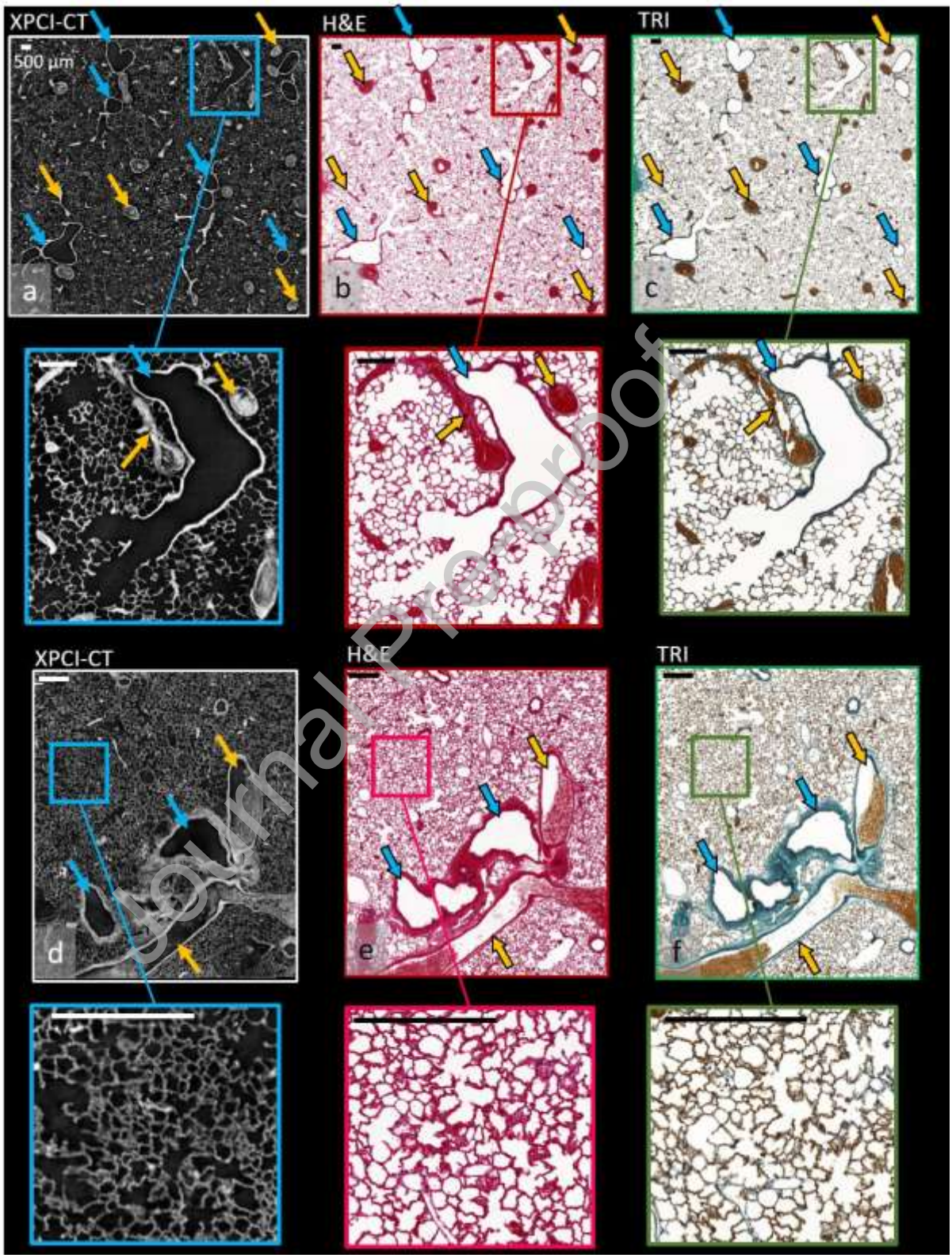

Figure **1**e-f are the correspondent H&E and TRI histologies. Here, a big blood vessel is displayed entangled to a bronchus. The regular alveolar pattern (typical of a normal, no pathological condition) is better visualized in the magnified insets. The XPCI-CT features of

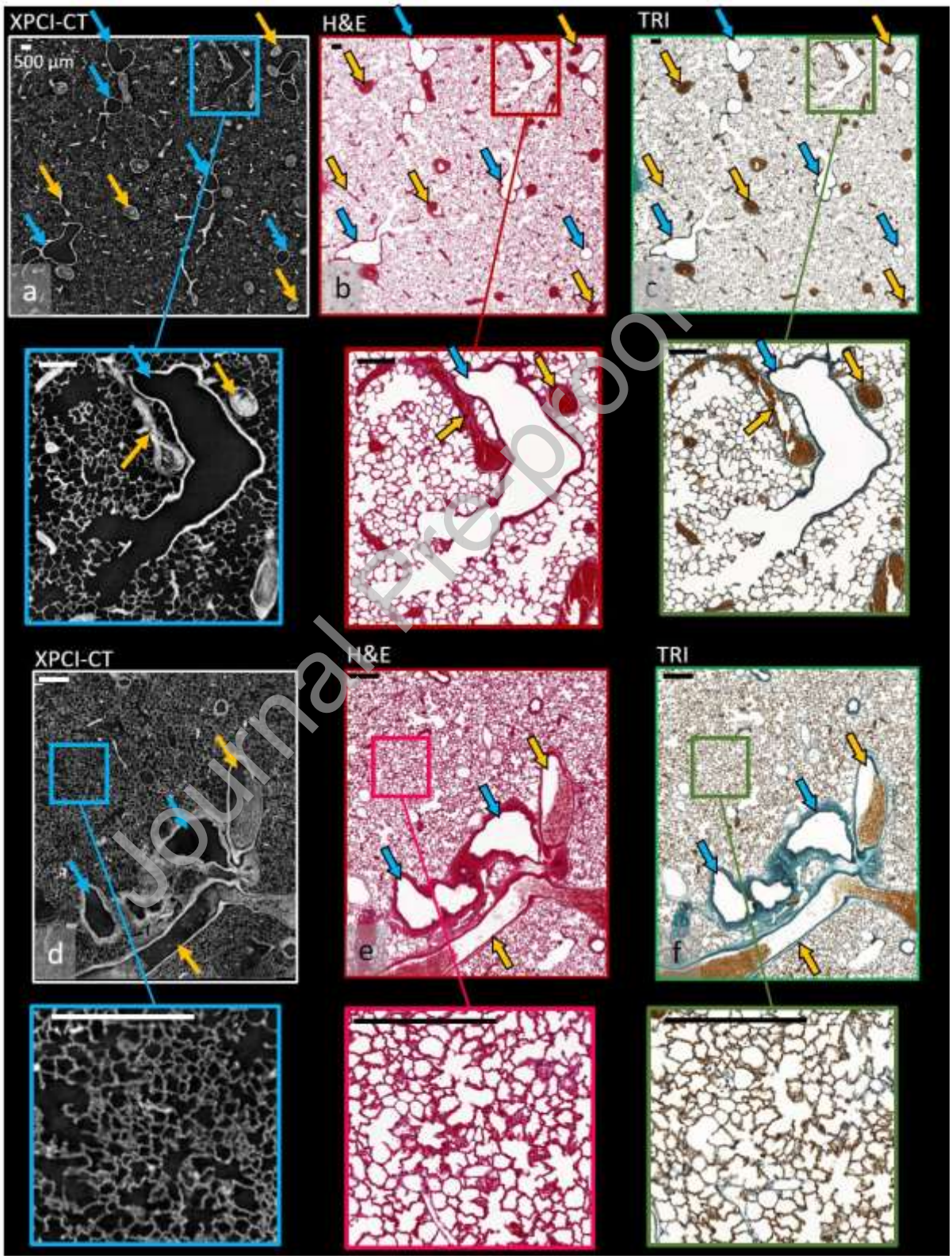

Figure **1** are also shown in Figure S1 (supplementary material) together with the comparison with Fe stained histology revealing no pathological areas but only small deposits (~ 25 µm large) between blood vessels and bronchi walls.

Imaging of the effects of MRT_{50} on lungs

1.63^3 μm^3 voxel XPCI-CT images of MRT_{50} treated rat lungs are reported in

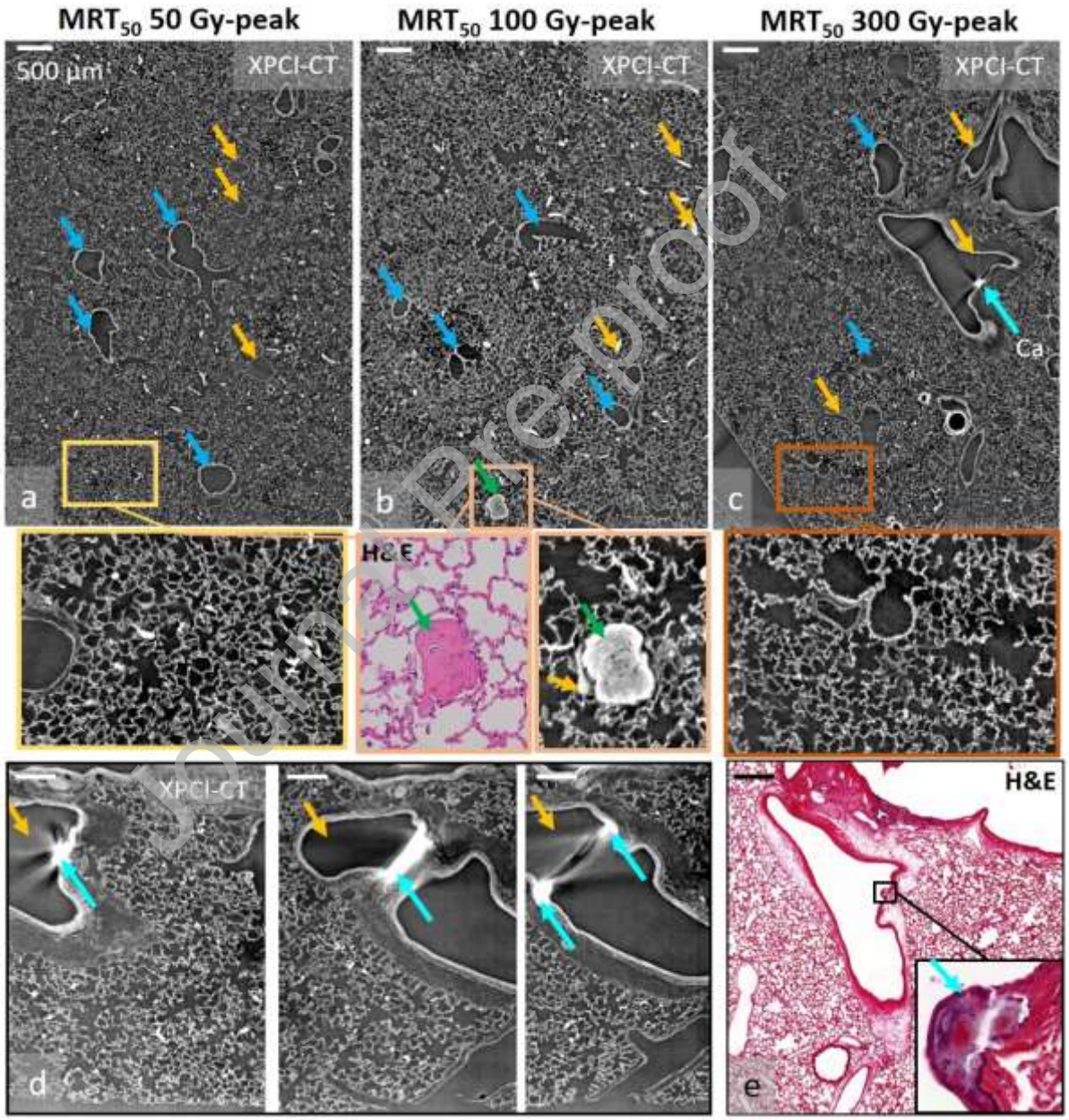

Figure 2 and

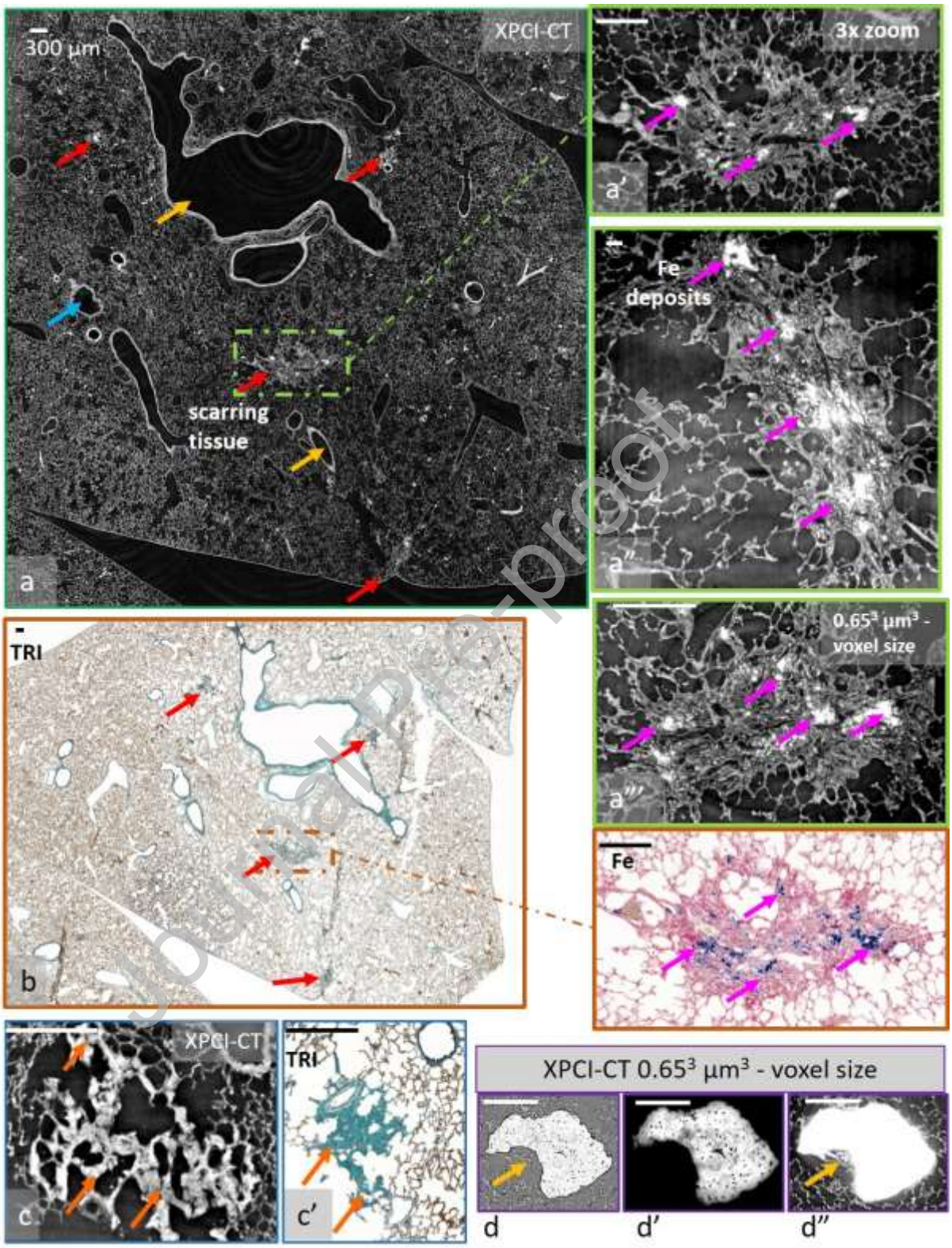

Figure 3. Within those samples, as confirmed by histology, only isolated scars with Fe mineralization are visible together with some collagen noduli and the calcification of the vessel endothelium. The

three specimens of each MRT_{50} irradiation group show similar structures and representative findings are reported in

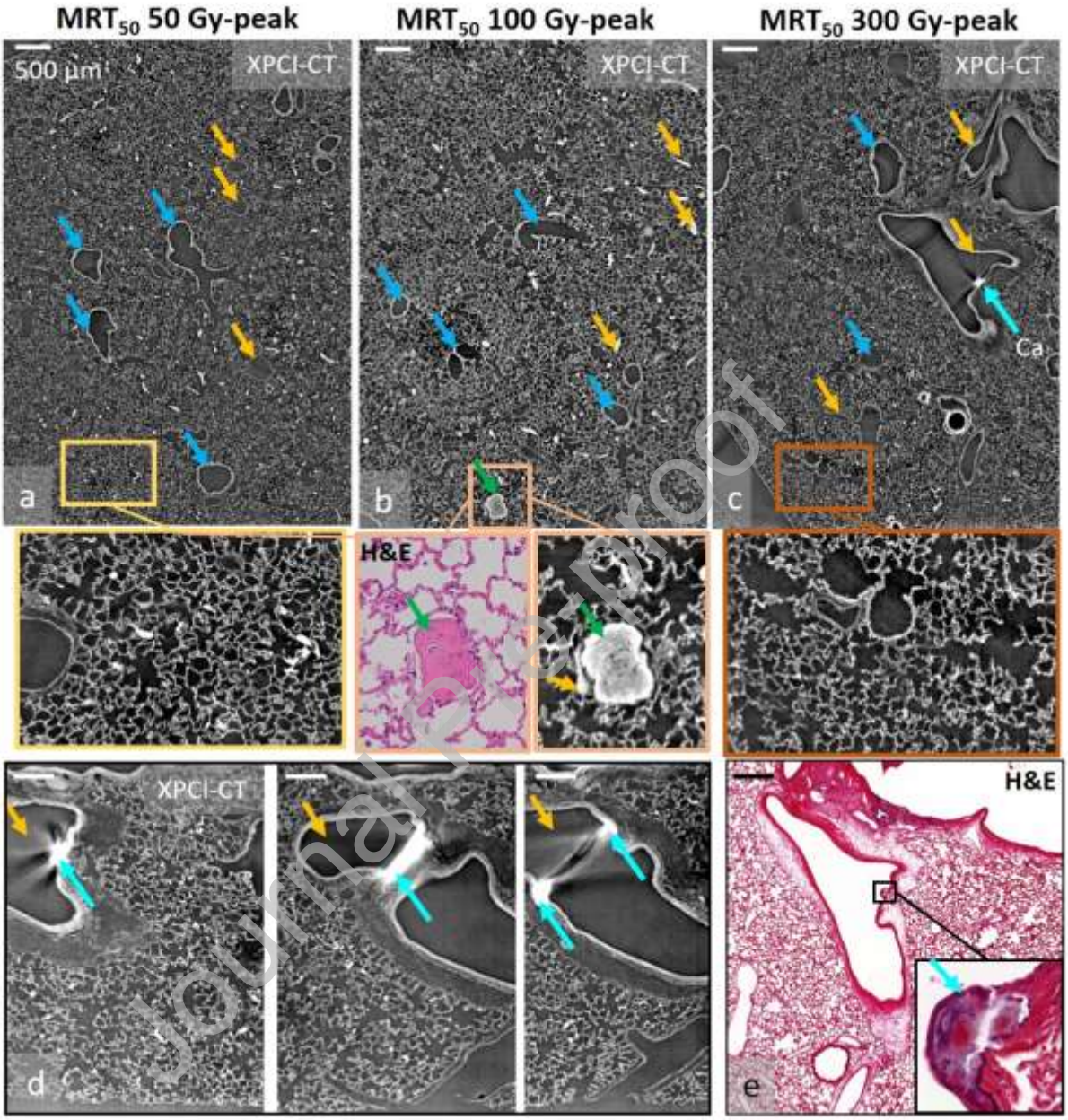

Figure 2 and

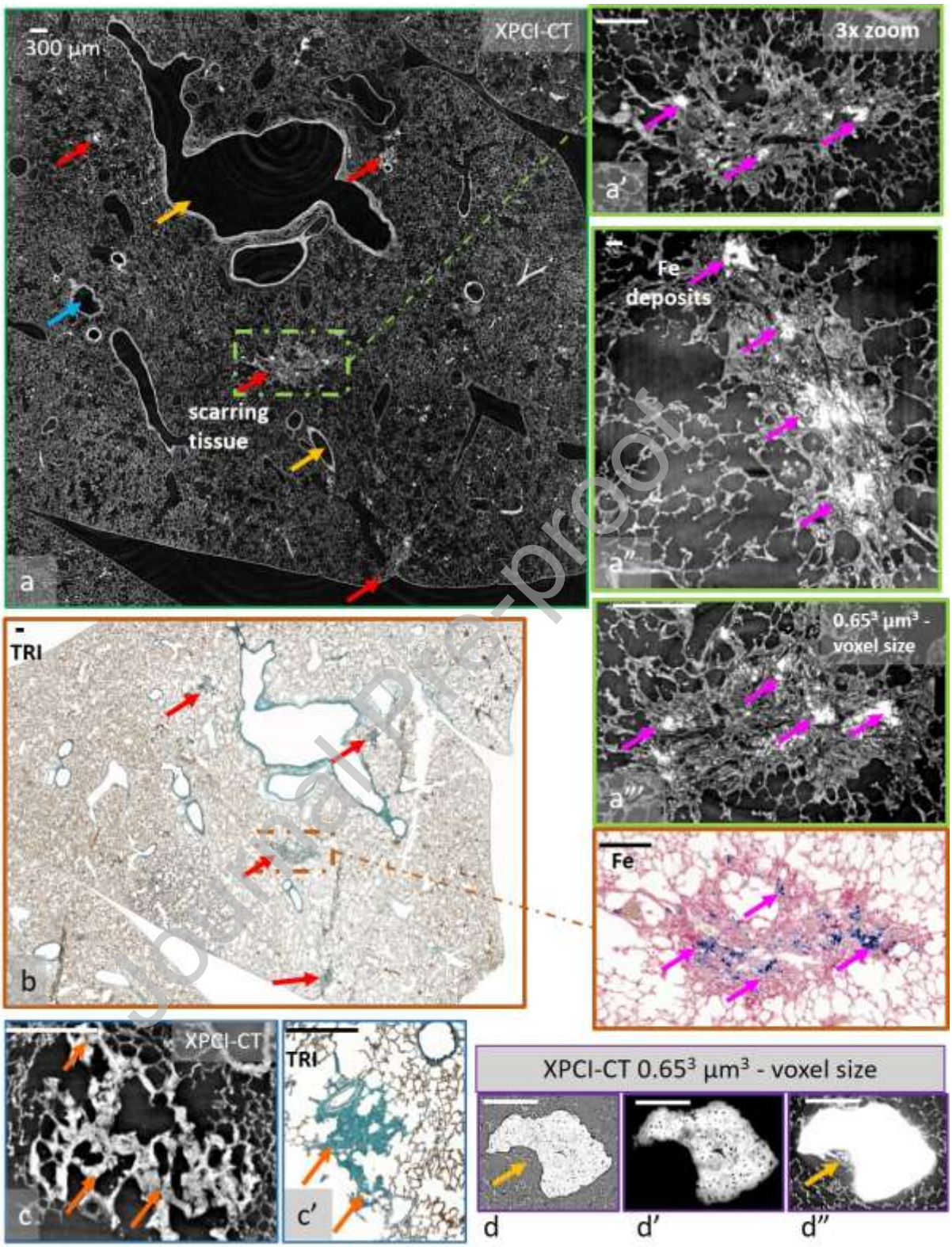

Figure 3. The tissue anatomy of all the three examined MRT_{50} 50 Gy-peak treated lungs appears very similar to the one of control animals: no significant evidence of the irradiation was found (see

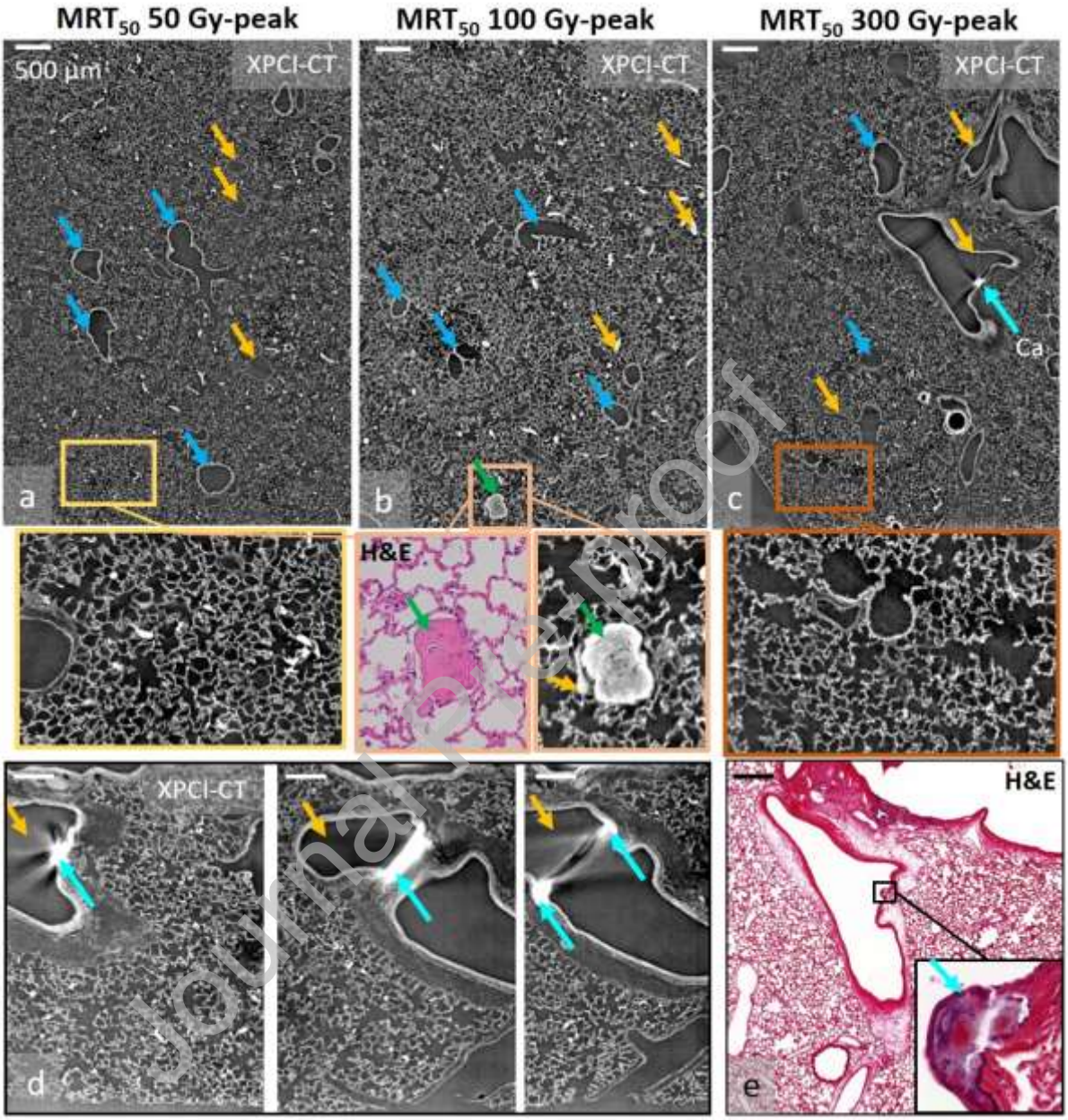

Figure 2a). The effects of the irradiation with MRT_{50} 100 Gy-peak on the lungs are shown in the XPCI-CT coronal image in

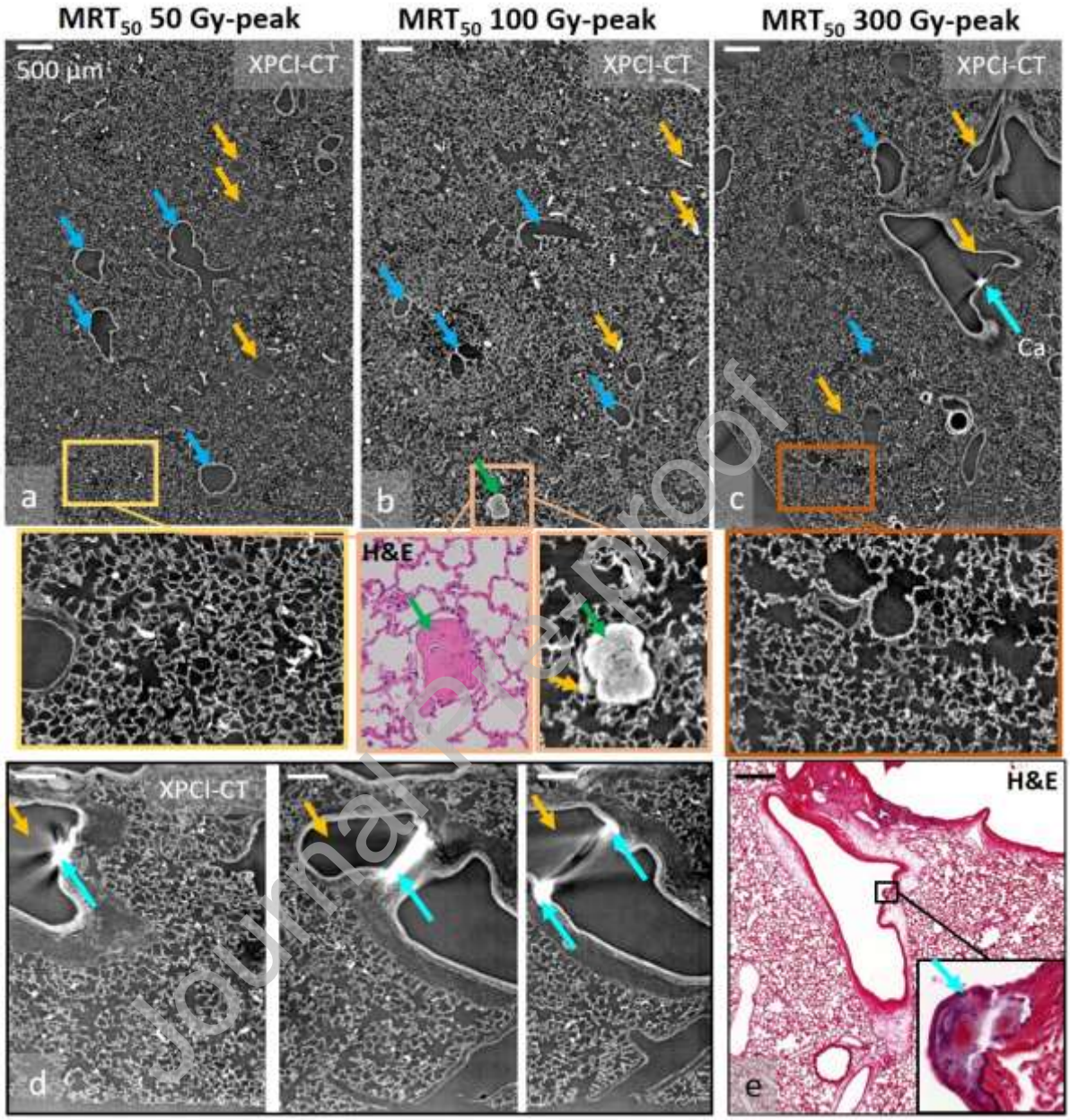

Figure 2b: overall the tissue appears as the one of healthy untreated samples, but a small collagen nodulus (volume of ~$2 \cdot 10^{-3}$ mm^3) is present, as proved by H&E histology (insets of

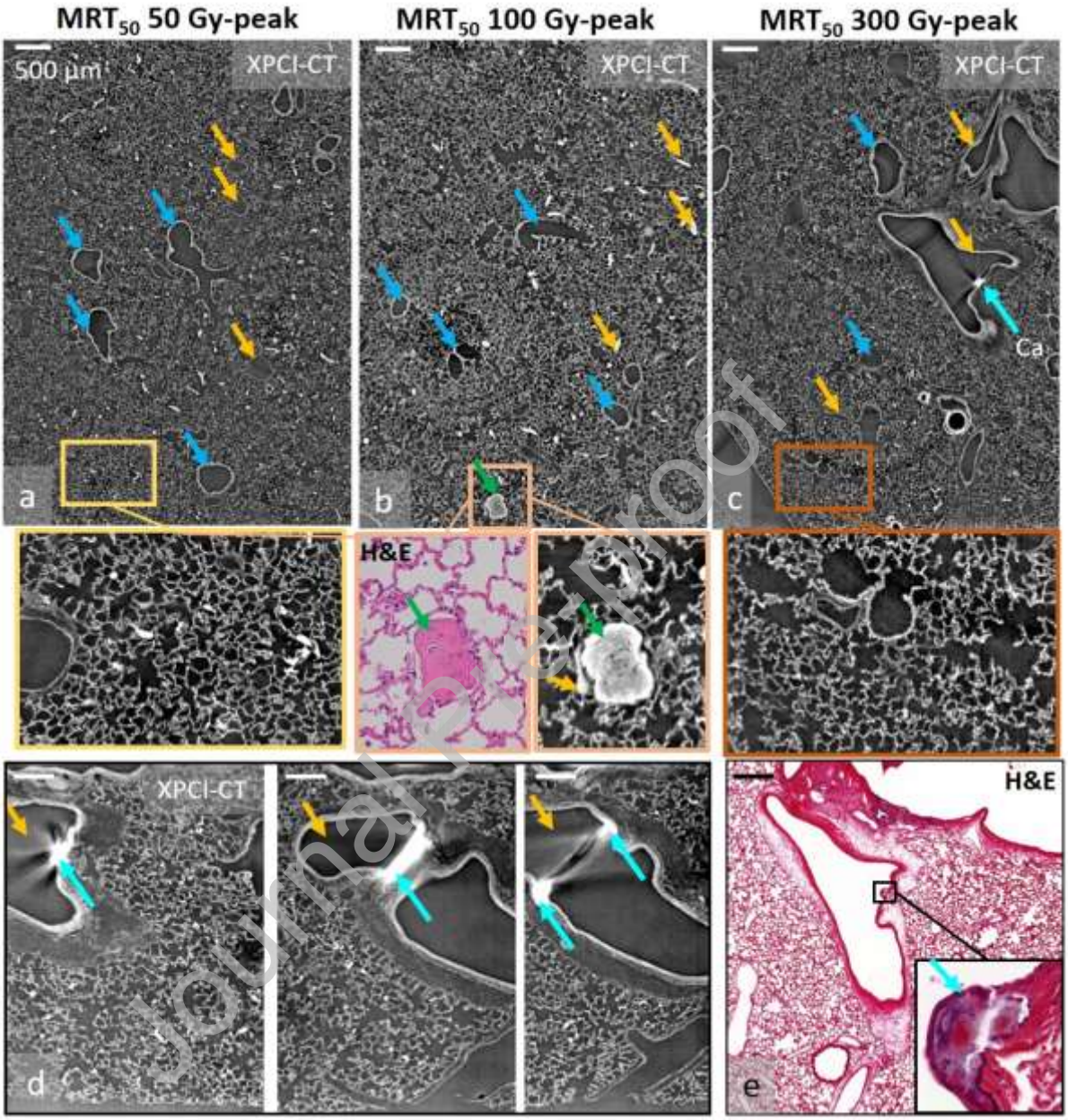

Figure 2b). Within the same specimen, another nodulus of similar dimensions was found. These two collagen noduli both grow in the vicinity of a blood vessel (yellow arrows in

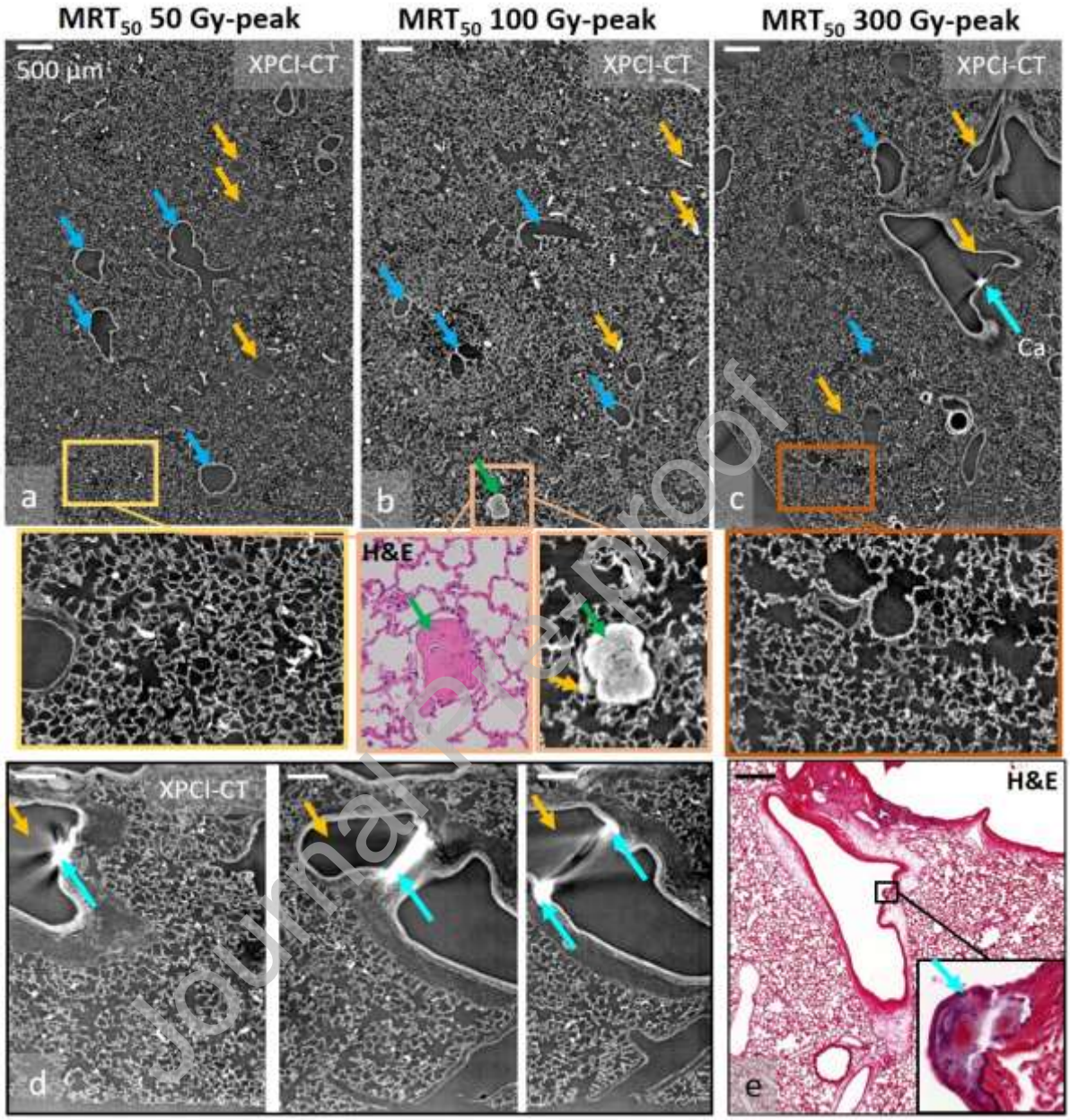

Figure 2b). Images in

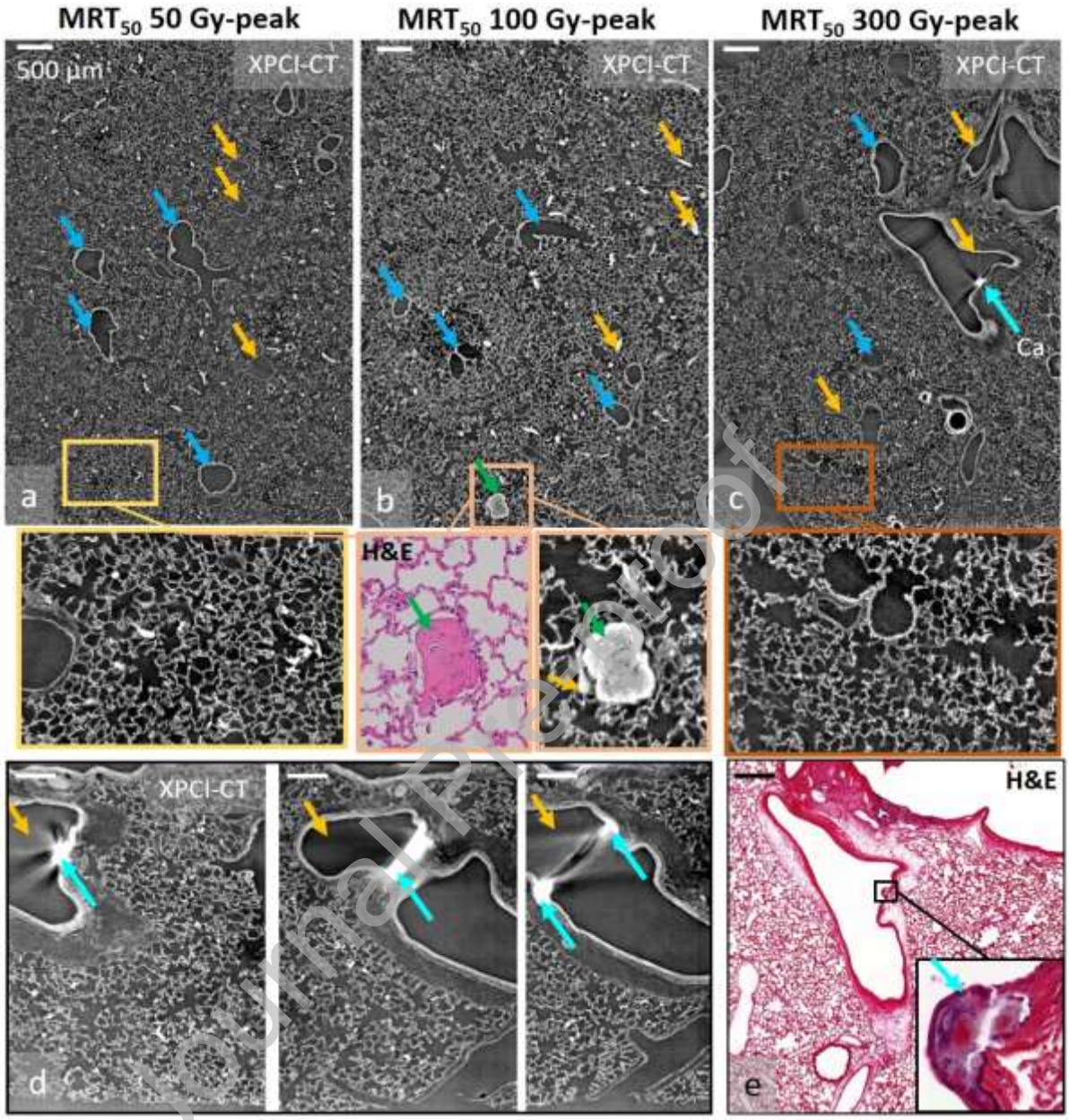

Figure 2c-d represent a MRT_{50} specimen irradiated with 300 Gy-peak dose. In the coronal image in

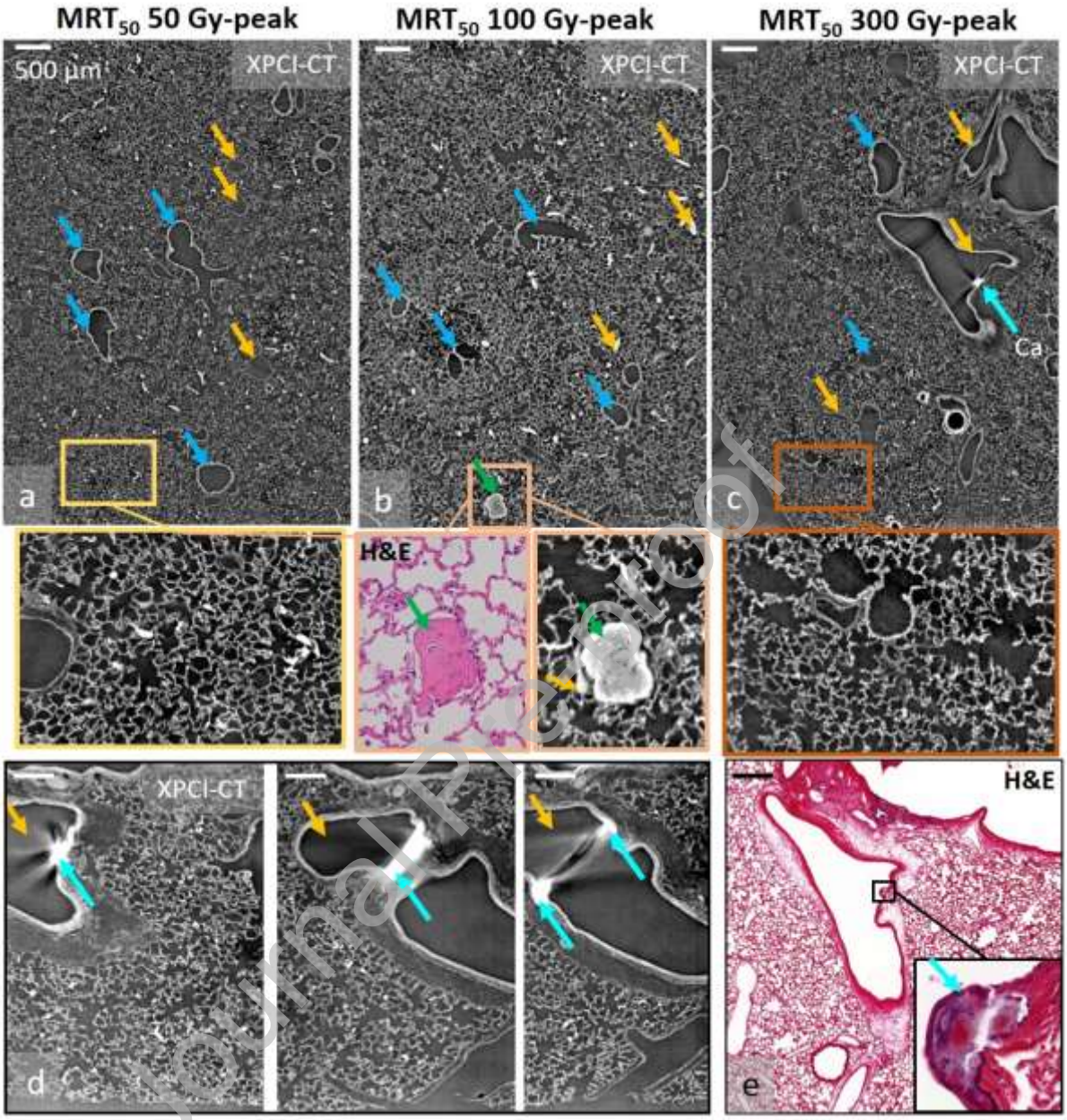

Figure 2c the only feature recognizable as an effect of the treatment is a hyperdense structure laying on the endothelium of a blood vessel. The H&E histologic analysis (

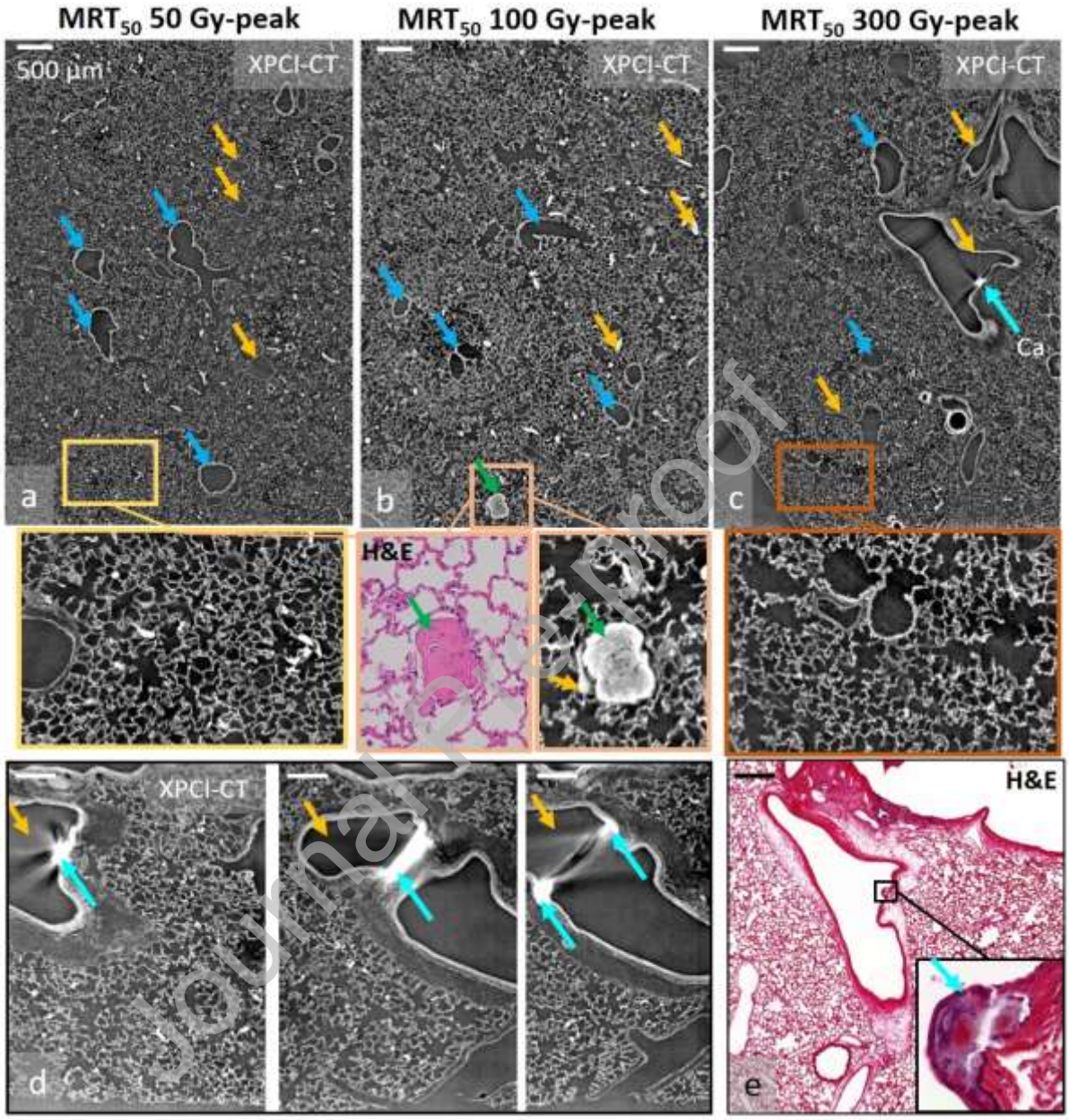

Figure 2e) identifies this dense structure as a calcification that replaced a part of the endothelium. This is a clear sign of a radiation-induced damage that can be followed in 3D along the endothelium,

as shown in the sagittal planes at three different depths within the sample (

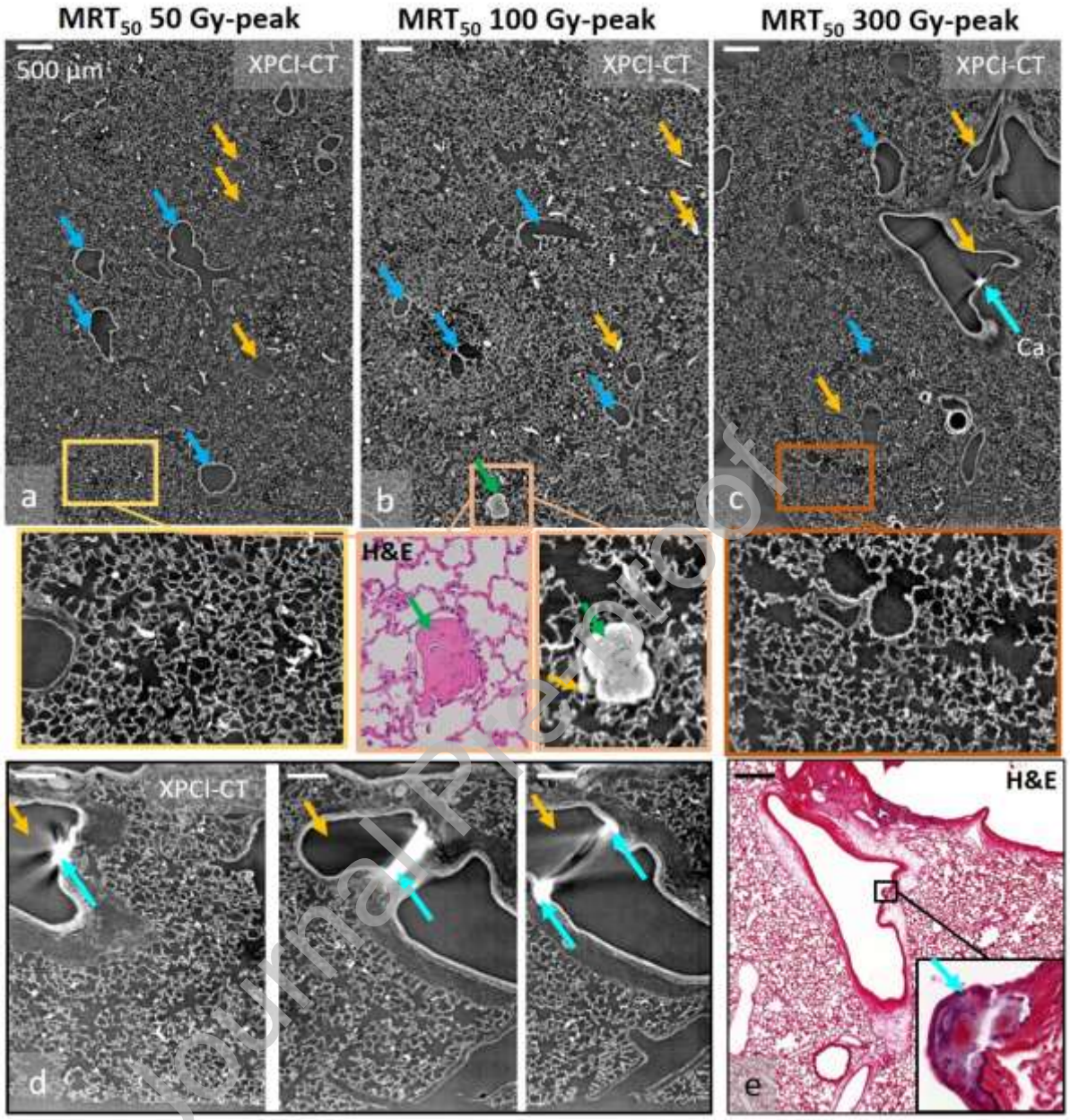

Figure 2d). In each of these figures, we see blood vessels and calcifications that appear as white spots (cyan arrows) indicating that the feature is much denser than the surrounding tissue. The streak–like artefacts on the image background originate from the abrupt variation in the refractive index between the soft tissue and the calcification.

XPCI-CT images in

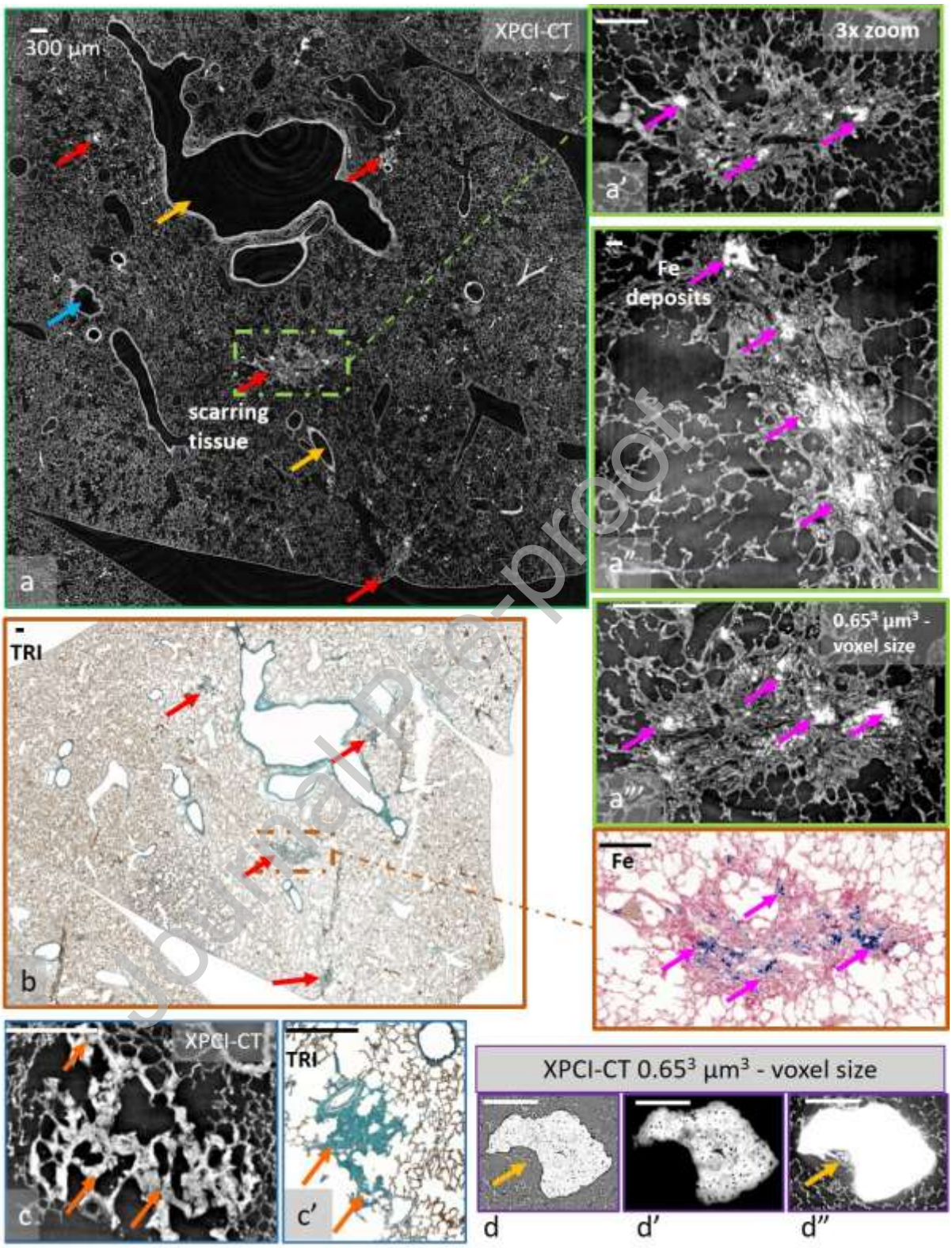

Figure 3 showcase the radiation-driven features detected in one of the samples of the MRT_{50} 600 Gy-peak group. The 1.63^3 μm^3 – voxel XPCI-CT coronal image (

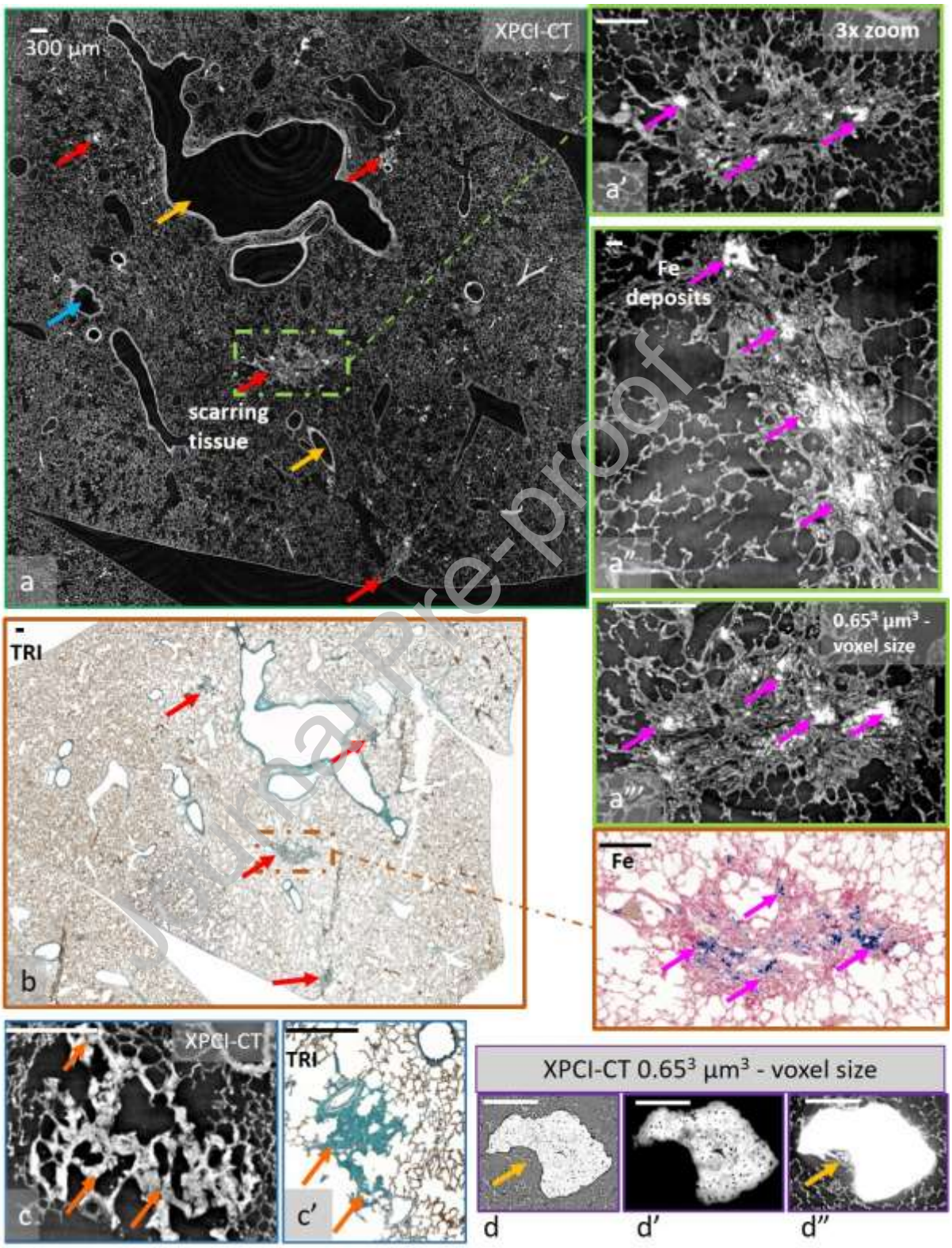

Figure 3a) shows isolated scars (red arrows) within the lung tissue. Images in

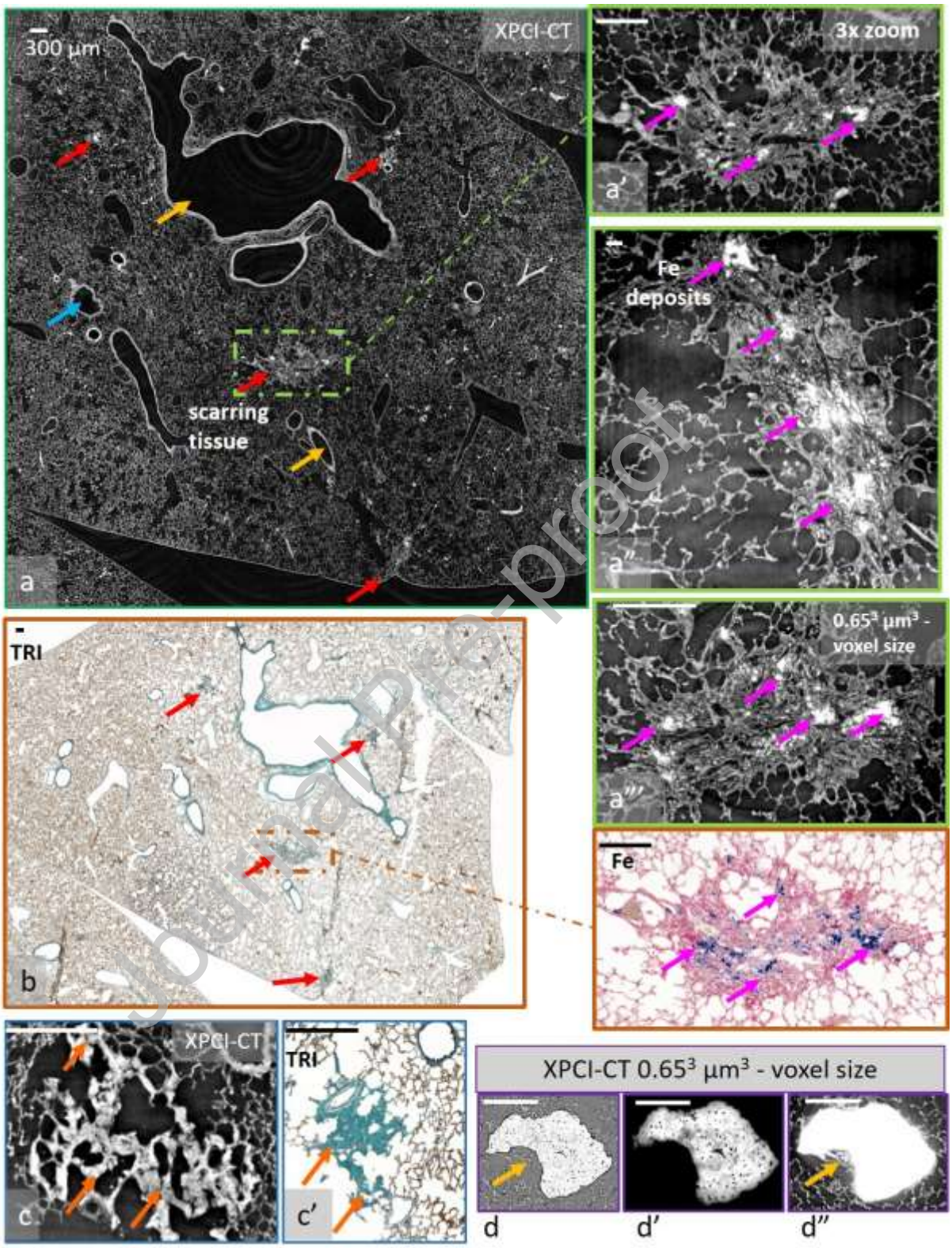

Figure 3a'-a"' report, respectively, the 3x zoom of the scar visible in the centre of

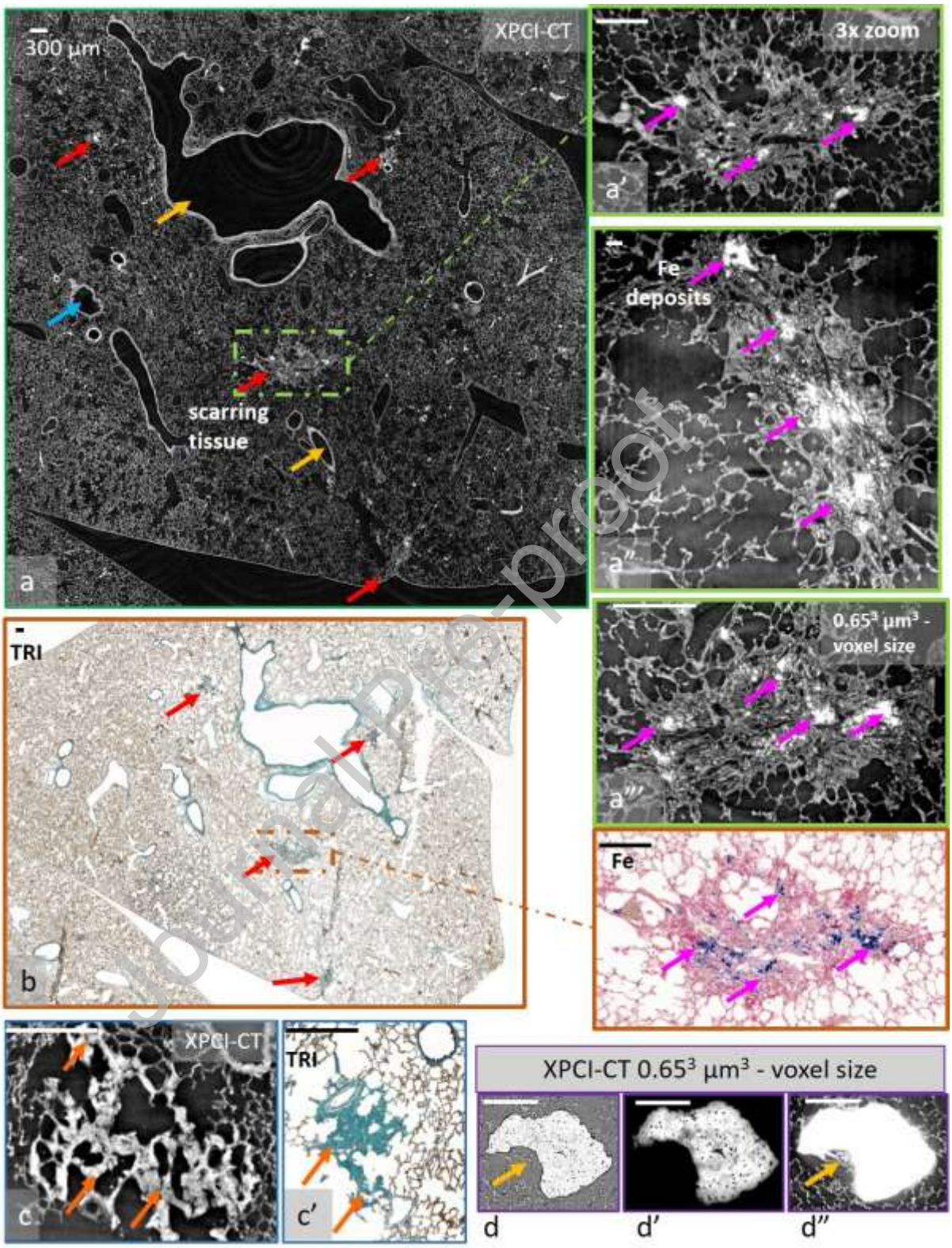

Figure 3a (green dashed box), its axial view and a 0.65^3 μm^3 voxel XPCI-CT coronal image of the same feature at a different depth with respect to Figure 3a within the lung tissue. The fibrotic nature of

the visualized scars is validated by the TRI histology of

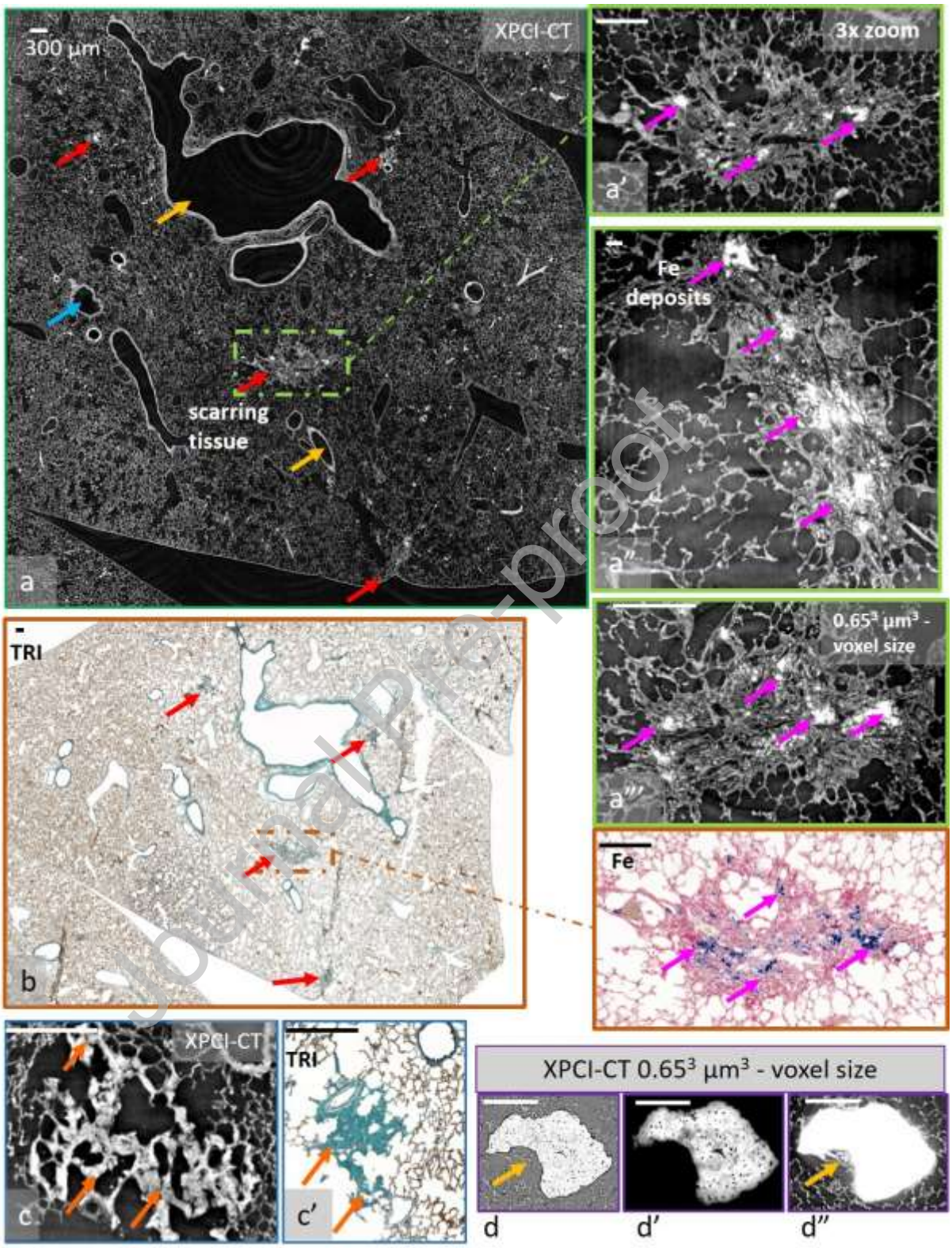

Figure 3b. The intra-scar Fe deposits, as identified by histology (

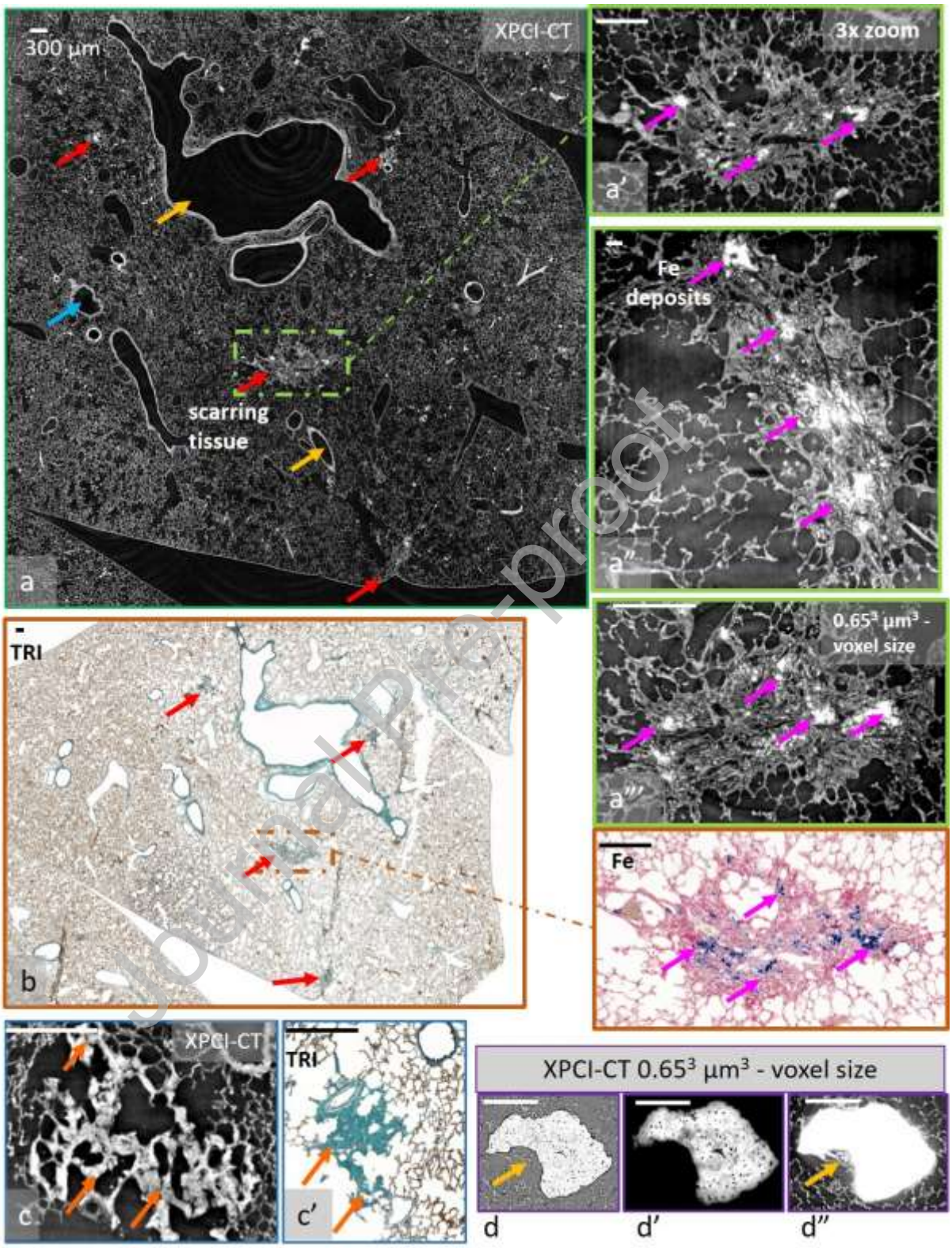

Figure 3b), are pointed out by magenta arrows and appear as blue after Fe staining. Other visible effects of the irradiation are the thickening of the alveolar septa (

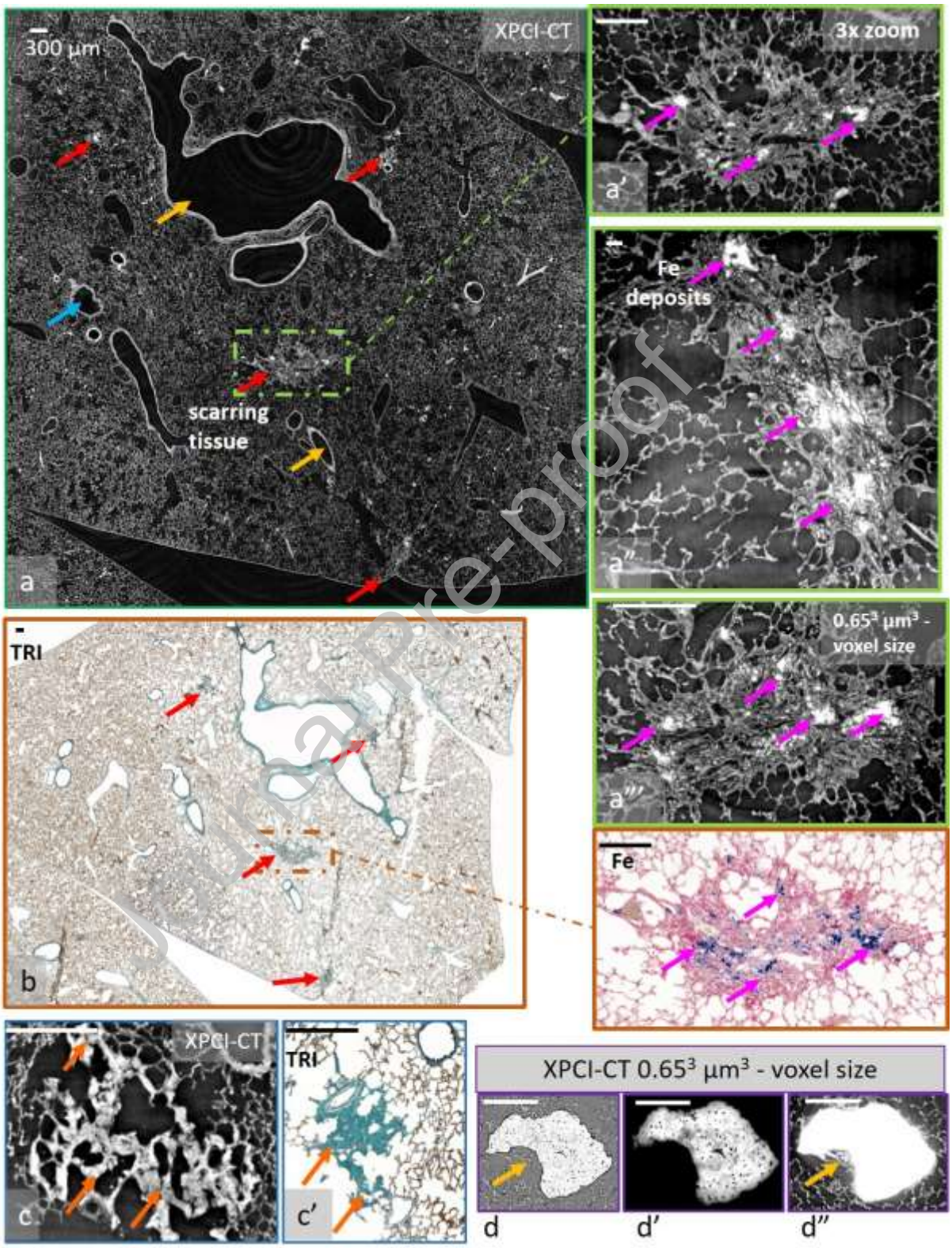

Figure 3c and corresponding TRI histology in

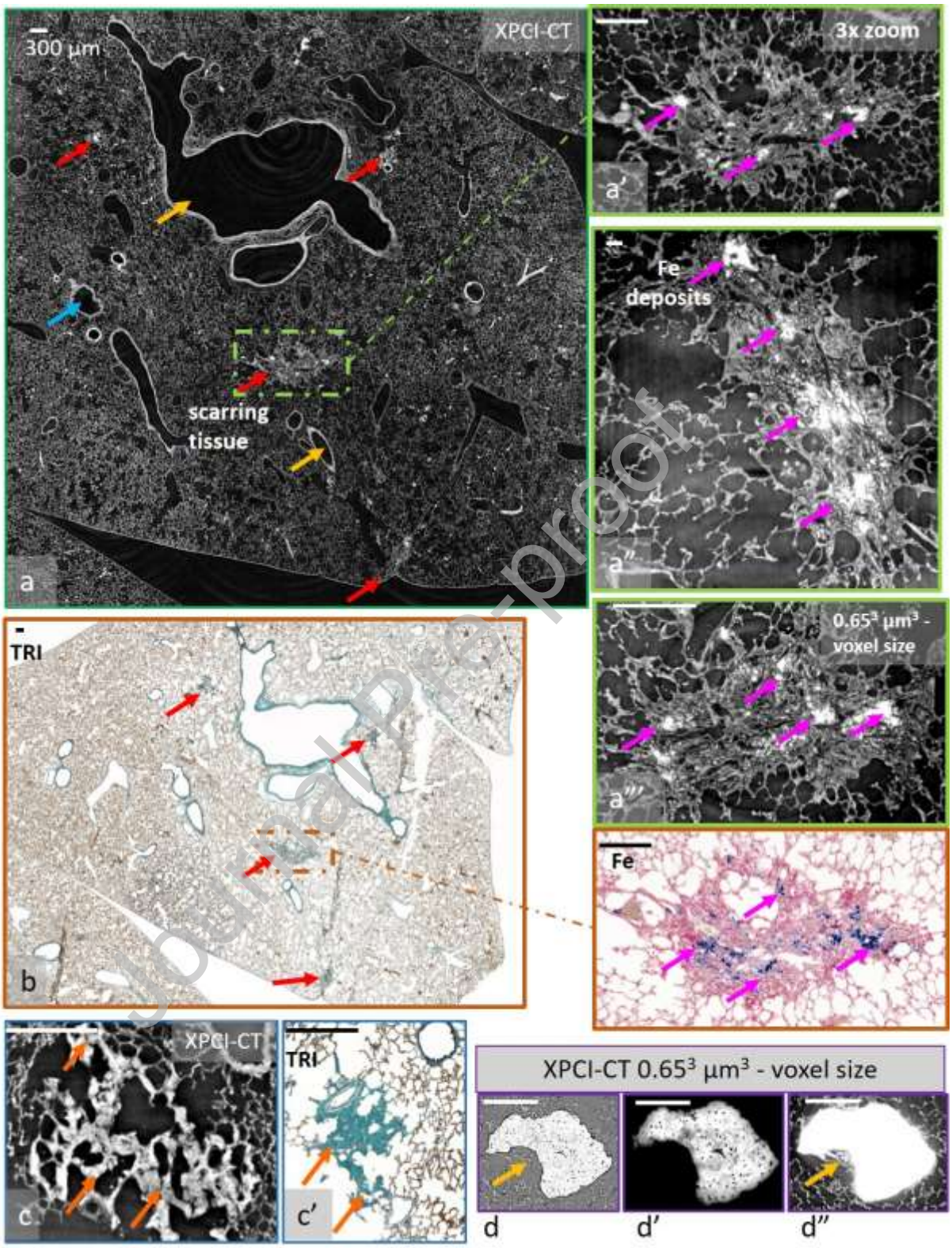

Figure 3c') and again the formation of collagen noduli, visualized in the 0.65^3 µm^3 voxel CT images in

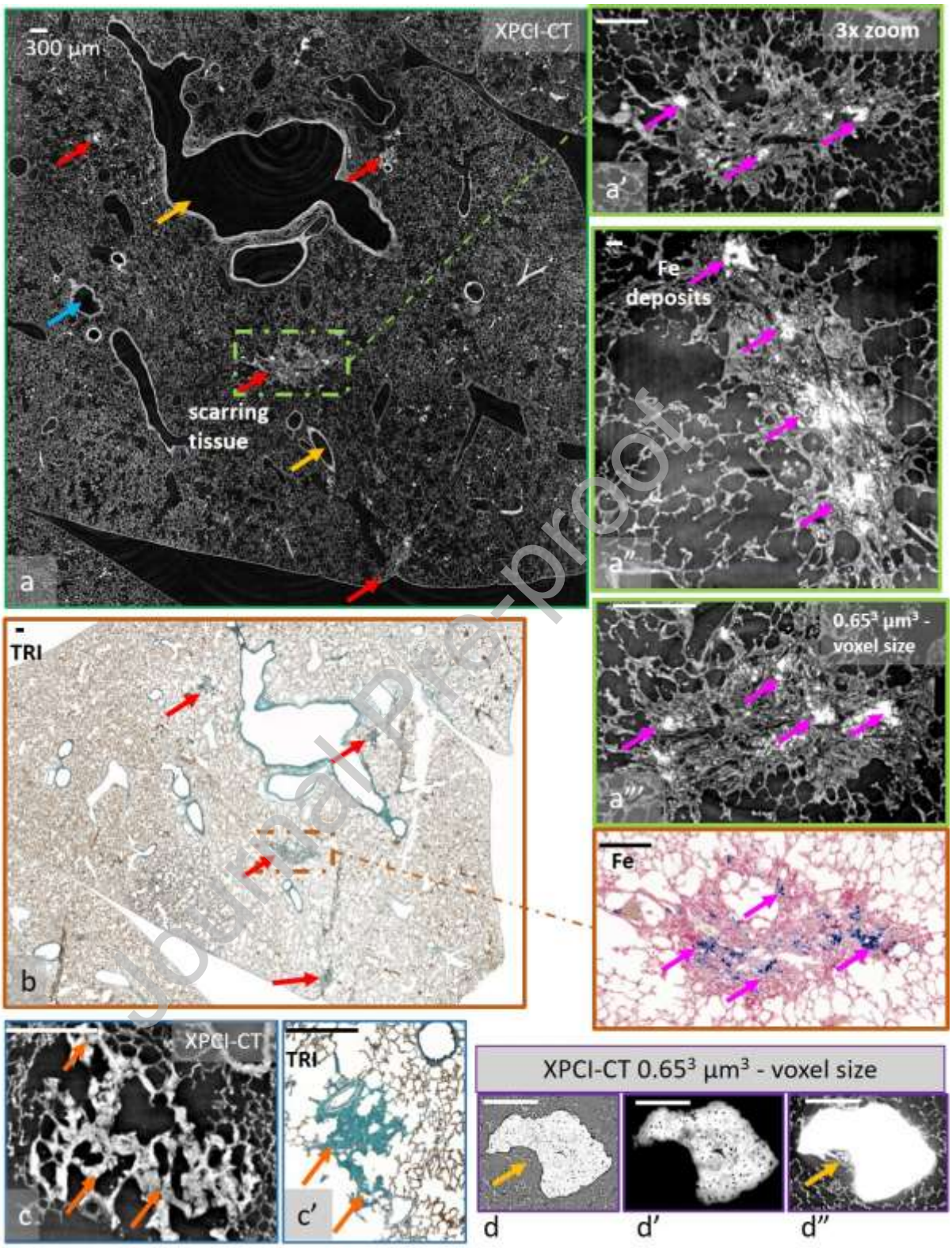

Figure 3d-d''. Those subfigures show the same CT slice with and without phase retrieval and for the latter case, with two different windowing. The noduli structure appears different among these

images. In the no-phase retrieved image (

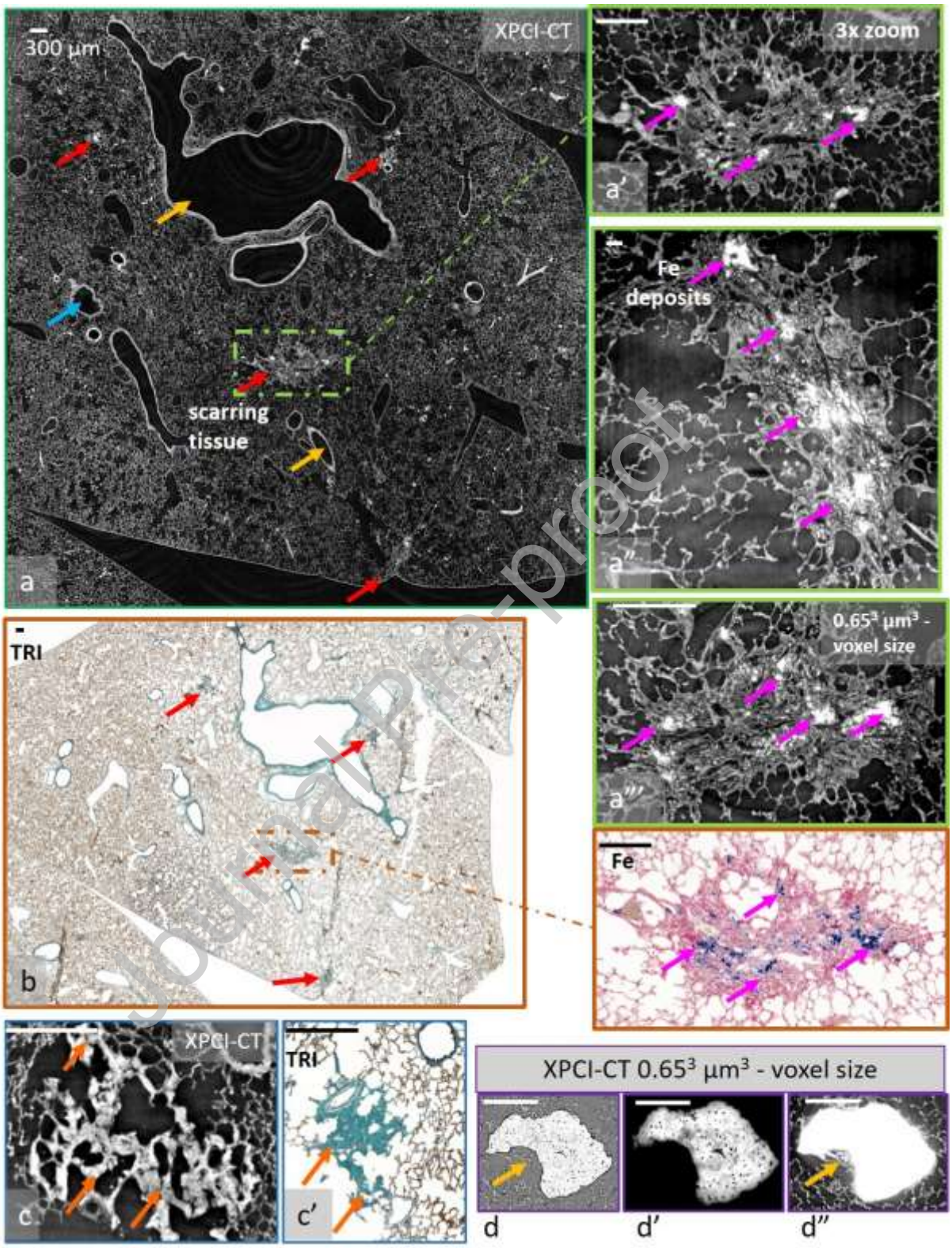

Figure 3d) the edges of the nodulus and of the different morphological details (such as alveoli and vessels) are enhanced and visible at once. The phase retrieved images provide a better area contrast

and depending on the windowing adjustment, it is possible to clearly visualize either the collagen part and cells (small dark spots) of the nodulus (

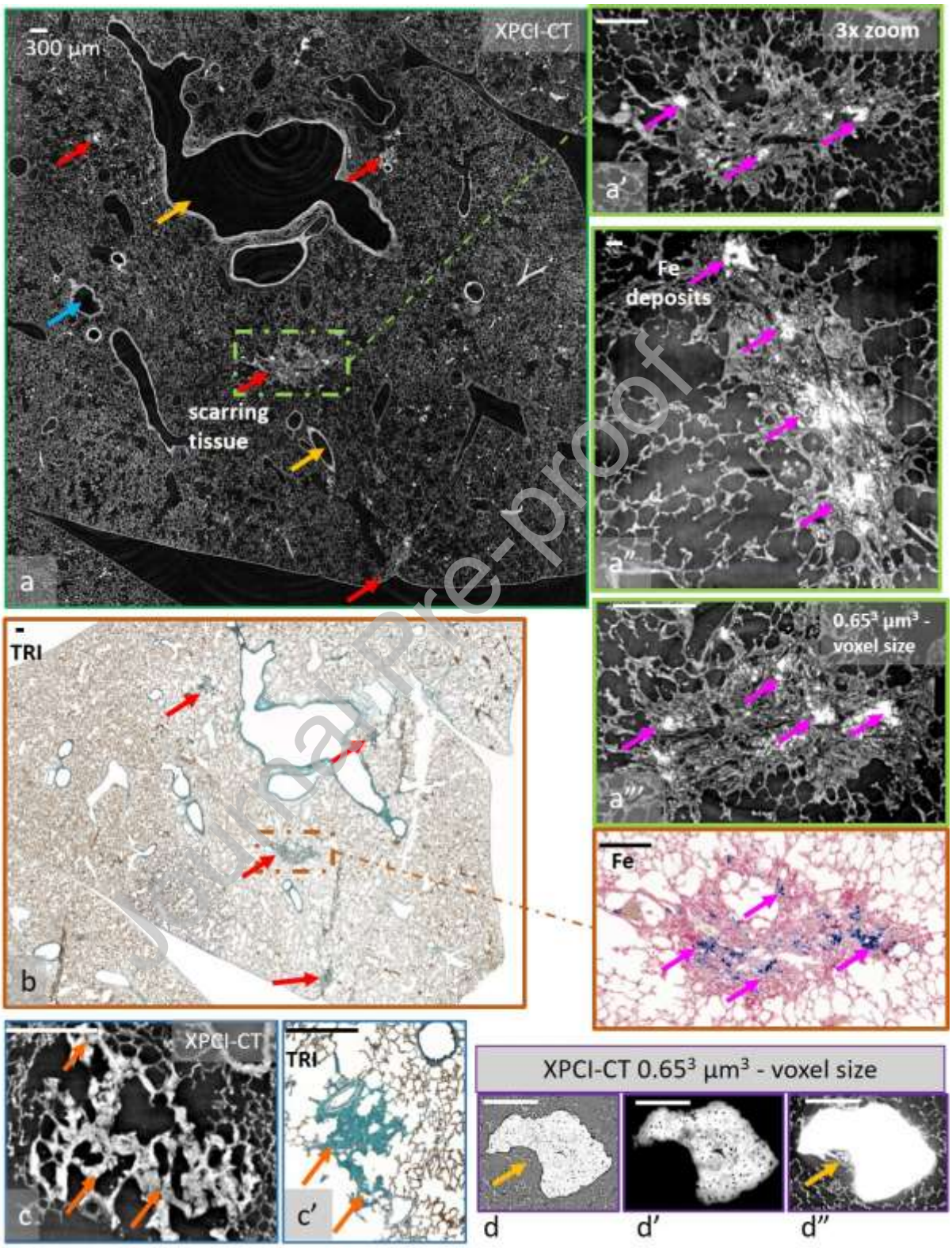

Figure 3d') or the surrounding tissues (

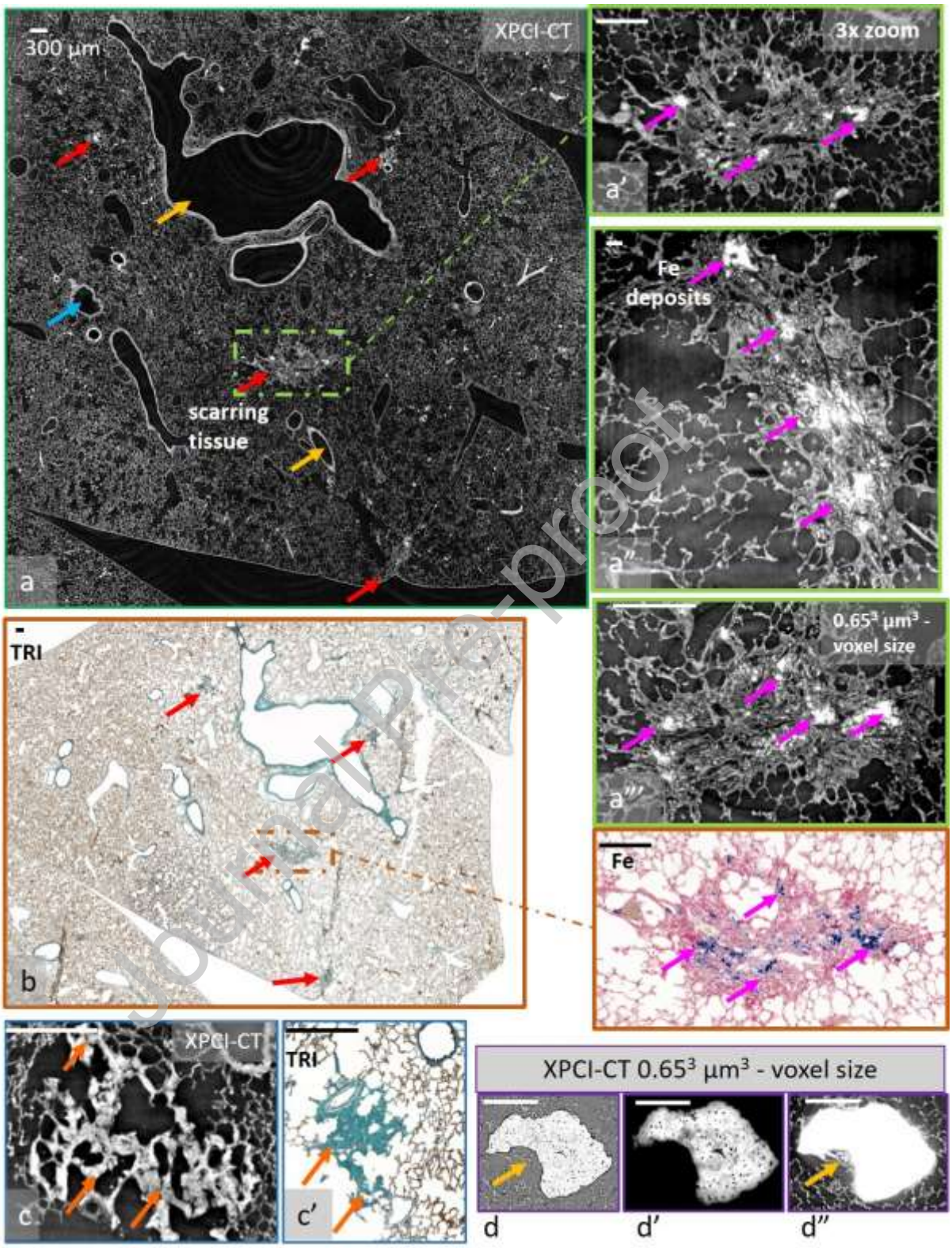

Figure 3d").

Imaging of the effects of MRT_{500} irradiation on lungs

Findings in the lung samples of rats irradiated by MRT_{500} are reported in 1.63^3 μm^3 voxel XPCI-CT images in

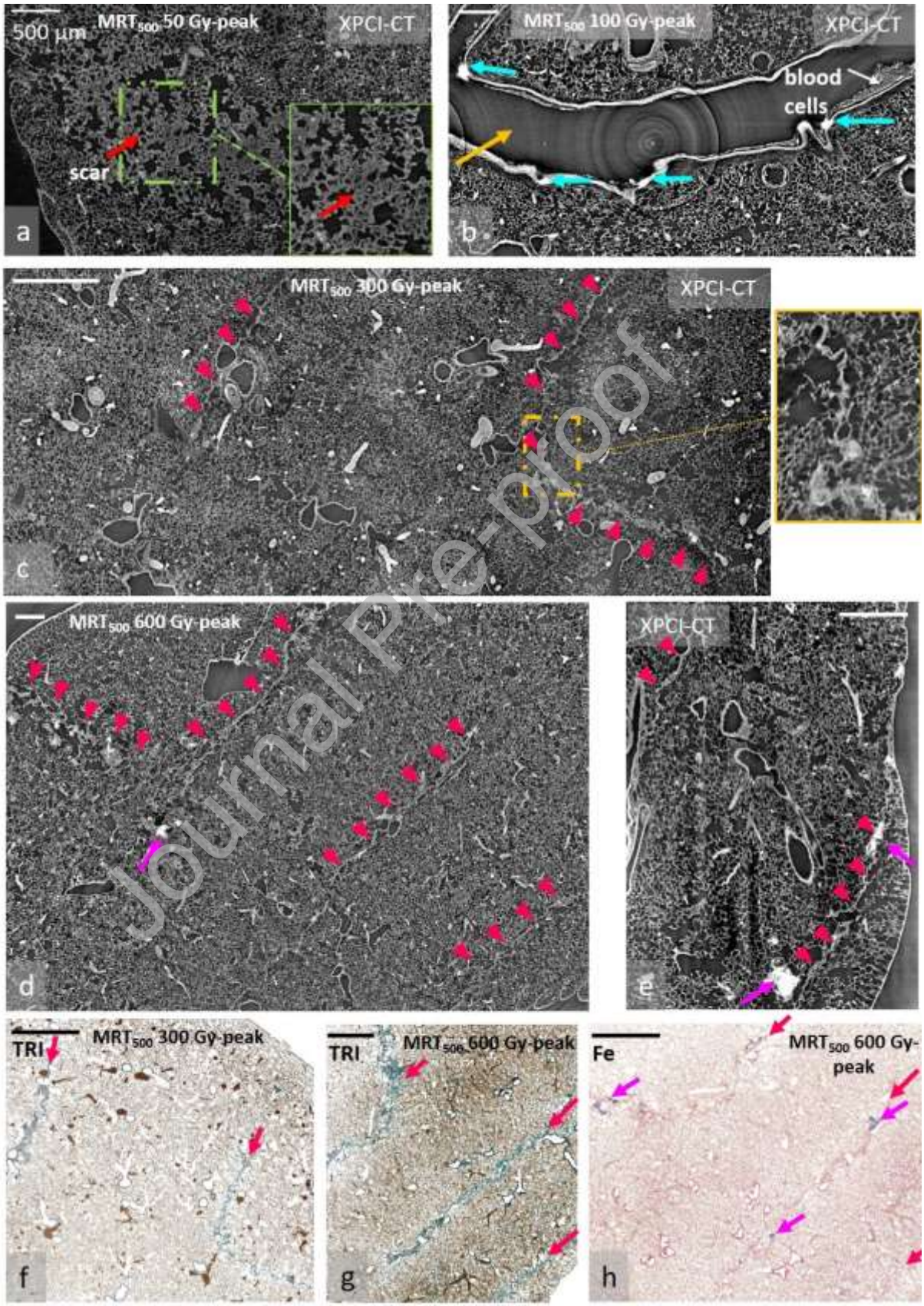

Figure *4*, where one representative sample is shown for each RT group, showing the three samples of each group similar the radio-induced morphological alterations. An extended scarring area within

the tissue of a MRT_{500} 50 Gy-peak treated rat lung is visible in the coronal image (

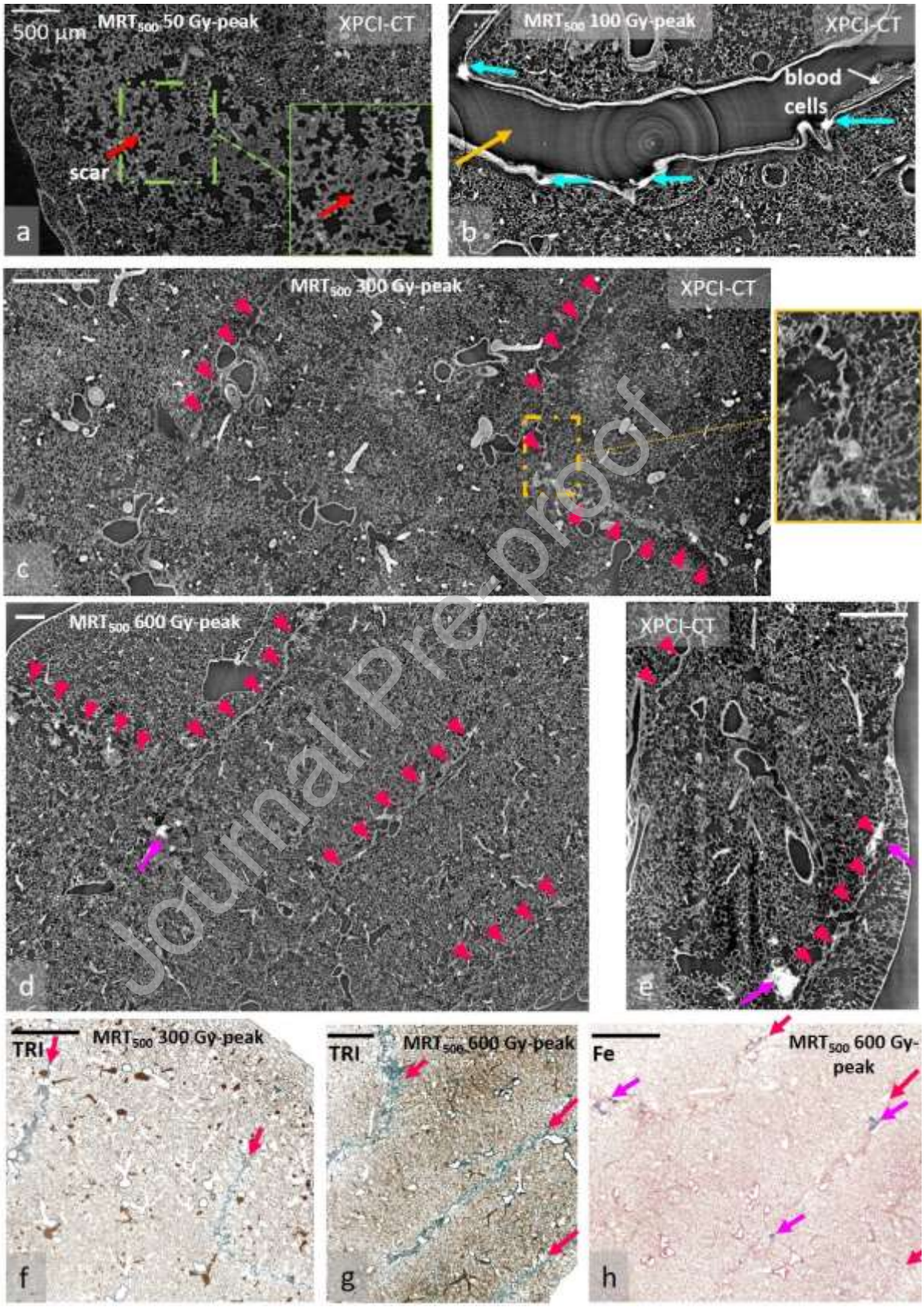

Figure 4a red arrow) together with its 2x zoom inset. The complete rearrangement of the alveolar spaces and the septa thickening are depicted, while, in the rest of the sample, the overall structure of the lung tissue seems preserved and looks similar to the one of control rats (

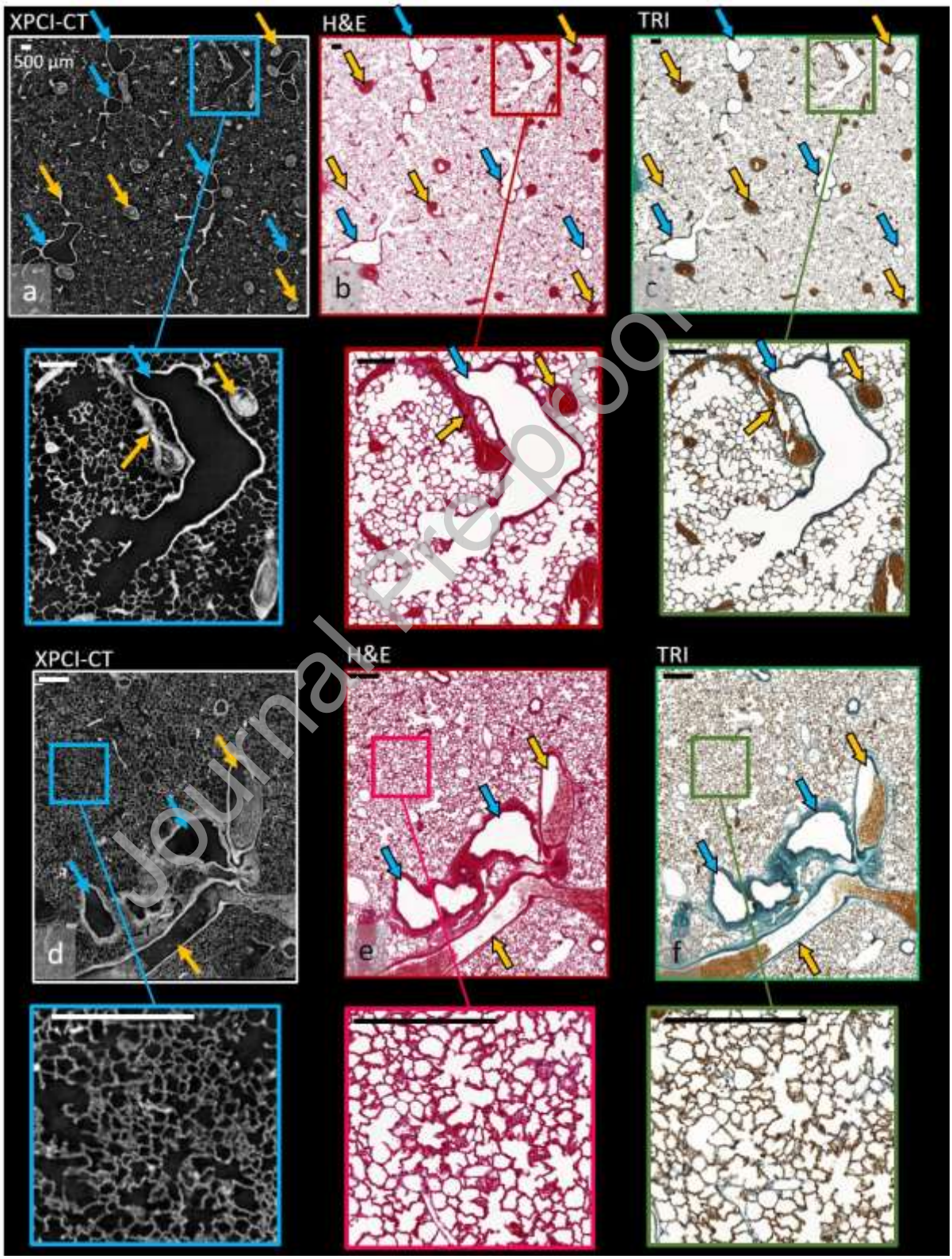

Figure 1). In the coronal XPCI-CT image in

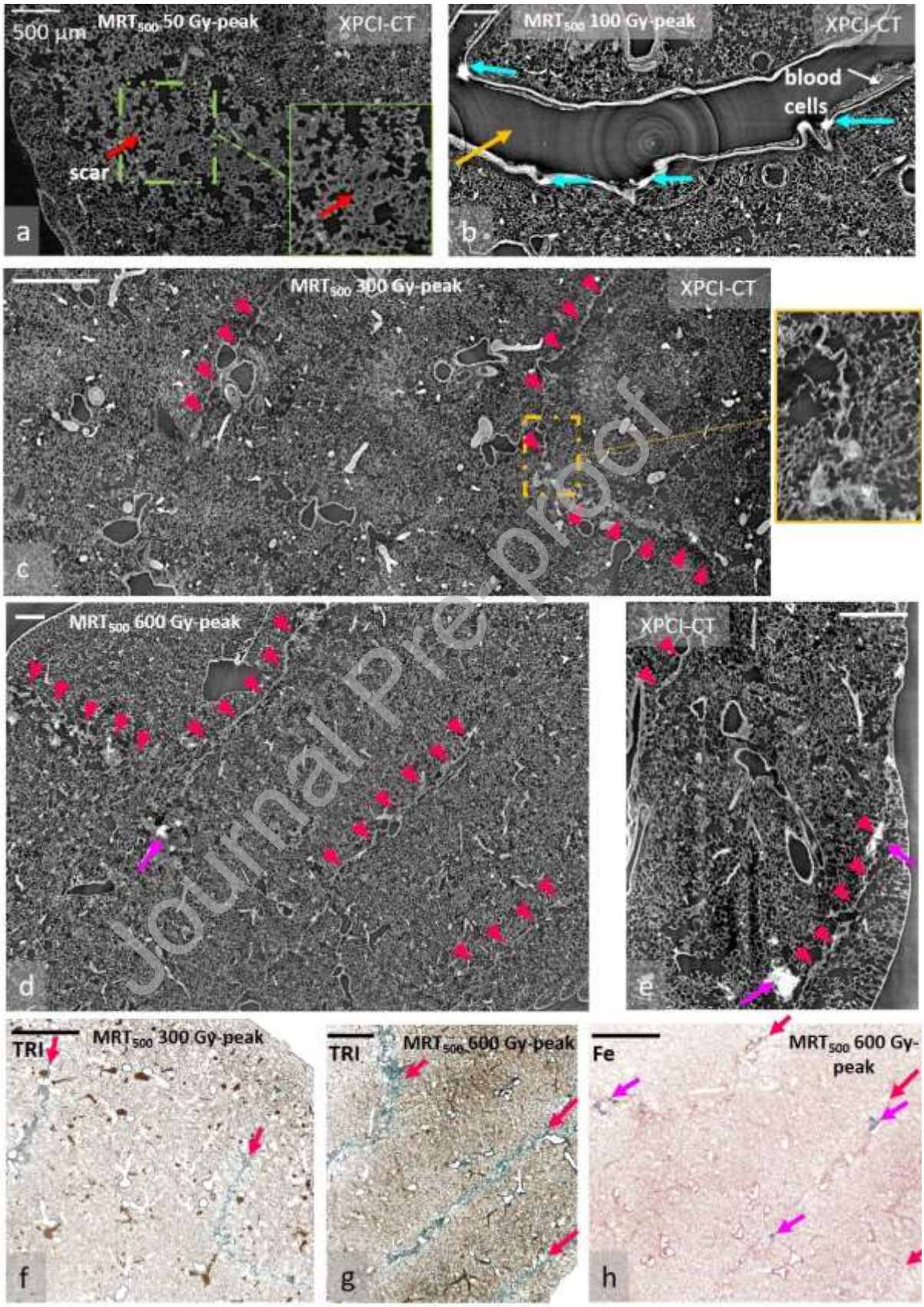

Figure 4b, a large blood vessel within a sample belonging to the MRT_{500} 100 Gy-peak group is observable. This image includes four dense structures on the endothelium layer (cyan arrows) that can be identified as Ca formations as in

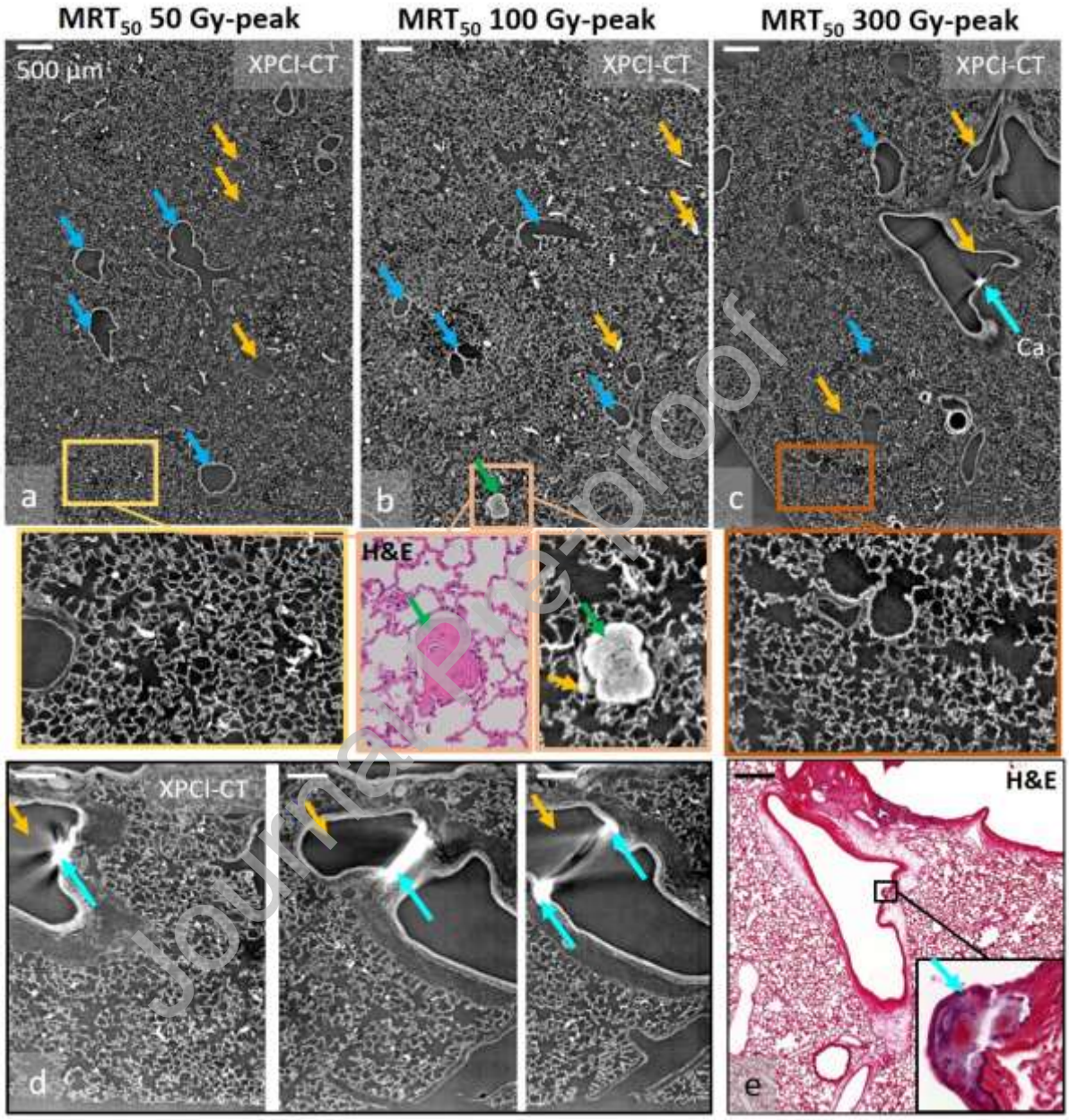

Figure 2c. The cyan arrows indicate the direction of the MRT_{500} paths, i.e. the two parallel lines lying horizontally on the coronal plane, along which calcifications are visible.

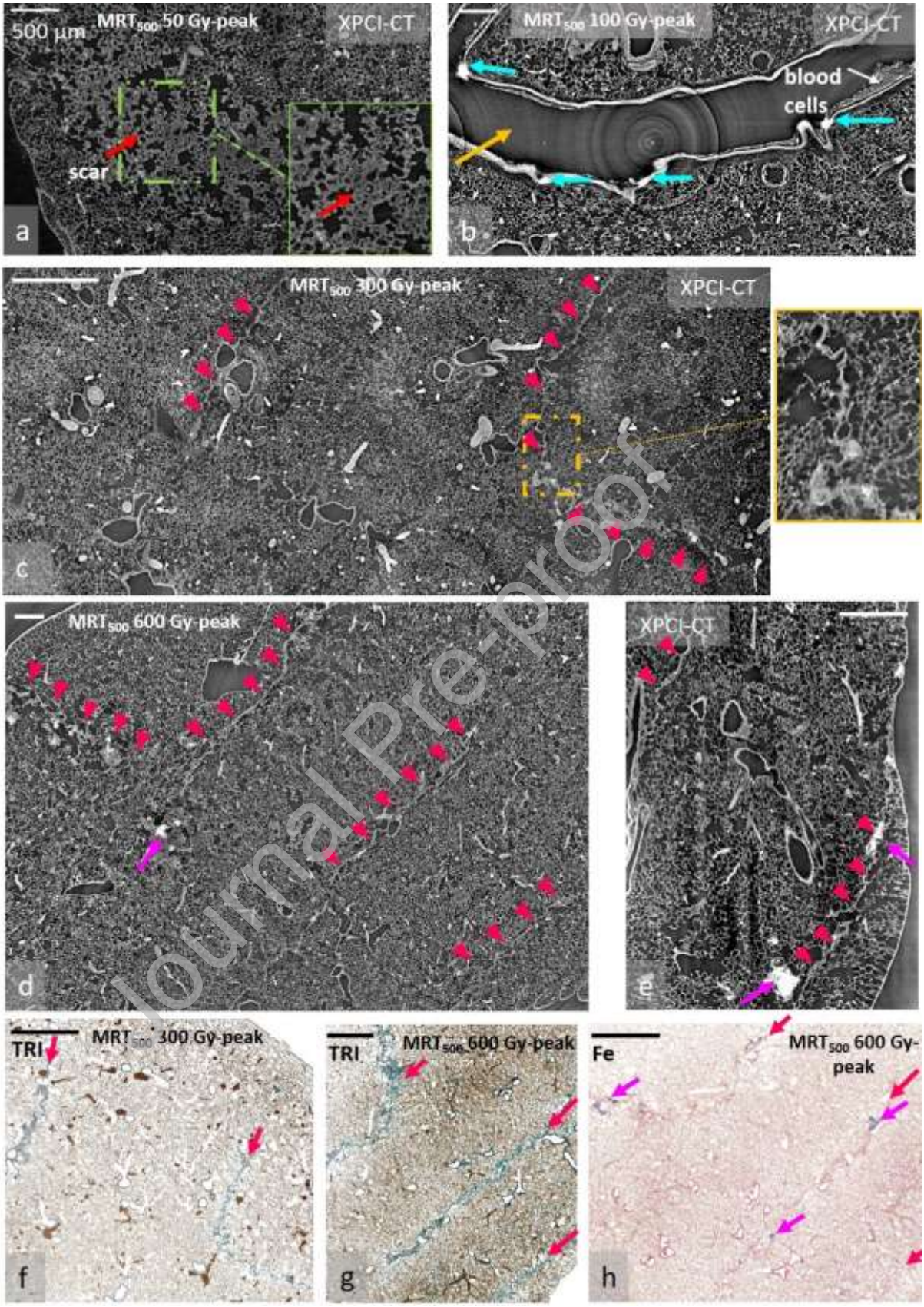

Figure 4c shows a 1.63^3 μm^3 – voxel XPCI-CT coronal image of a sample of the MRT_{500} 300 Gy-peak group. The amaranth arrowheads help identifying the stripe-scars.

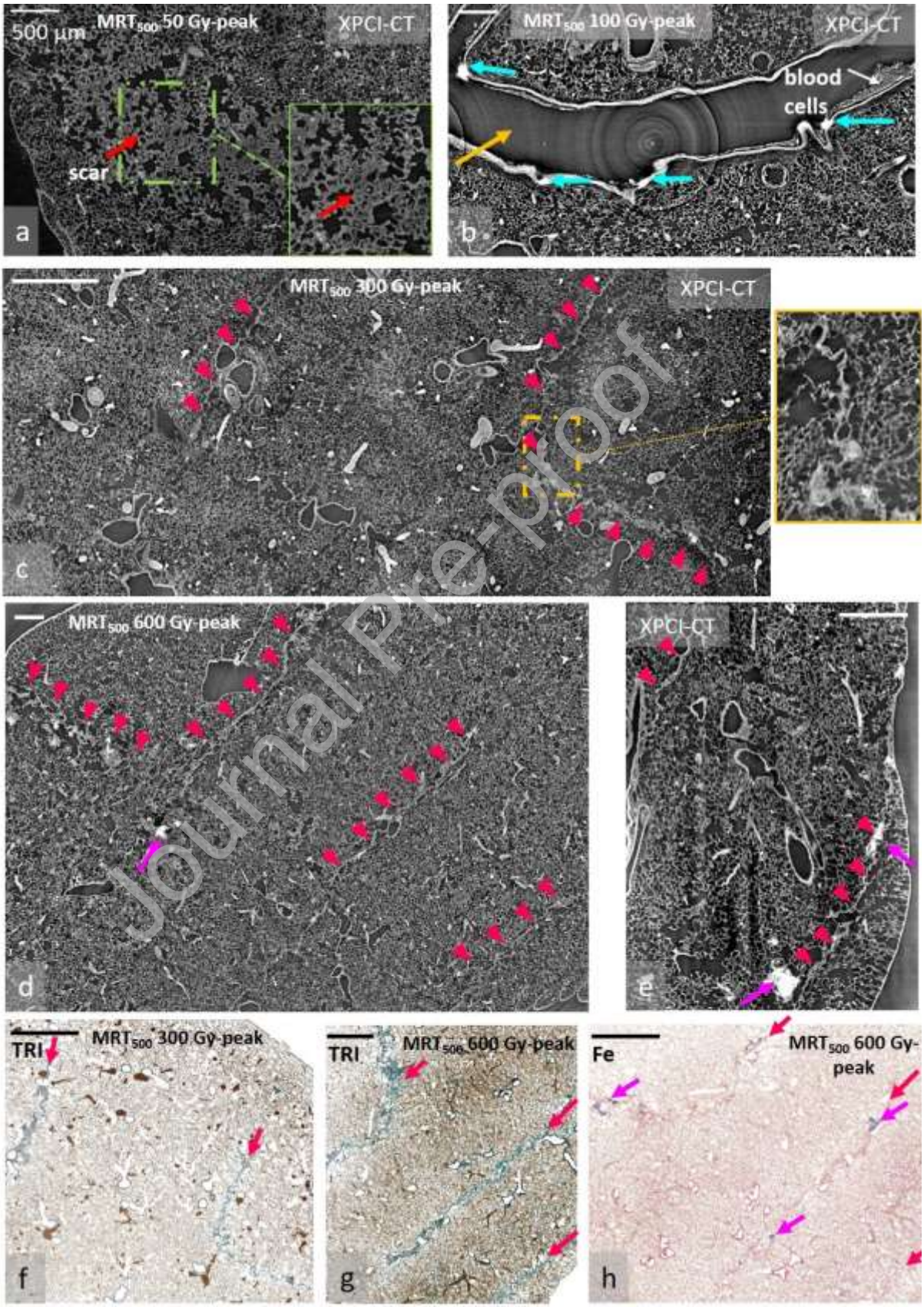

Figure 4c reports only two out of the three MRT_{500} scars and the magnified view in the inset shows details within the scar. In the XPCI-CT image of a MRT_{500} 600 Gy-peak irradiated lung (

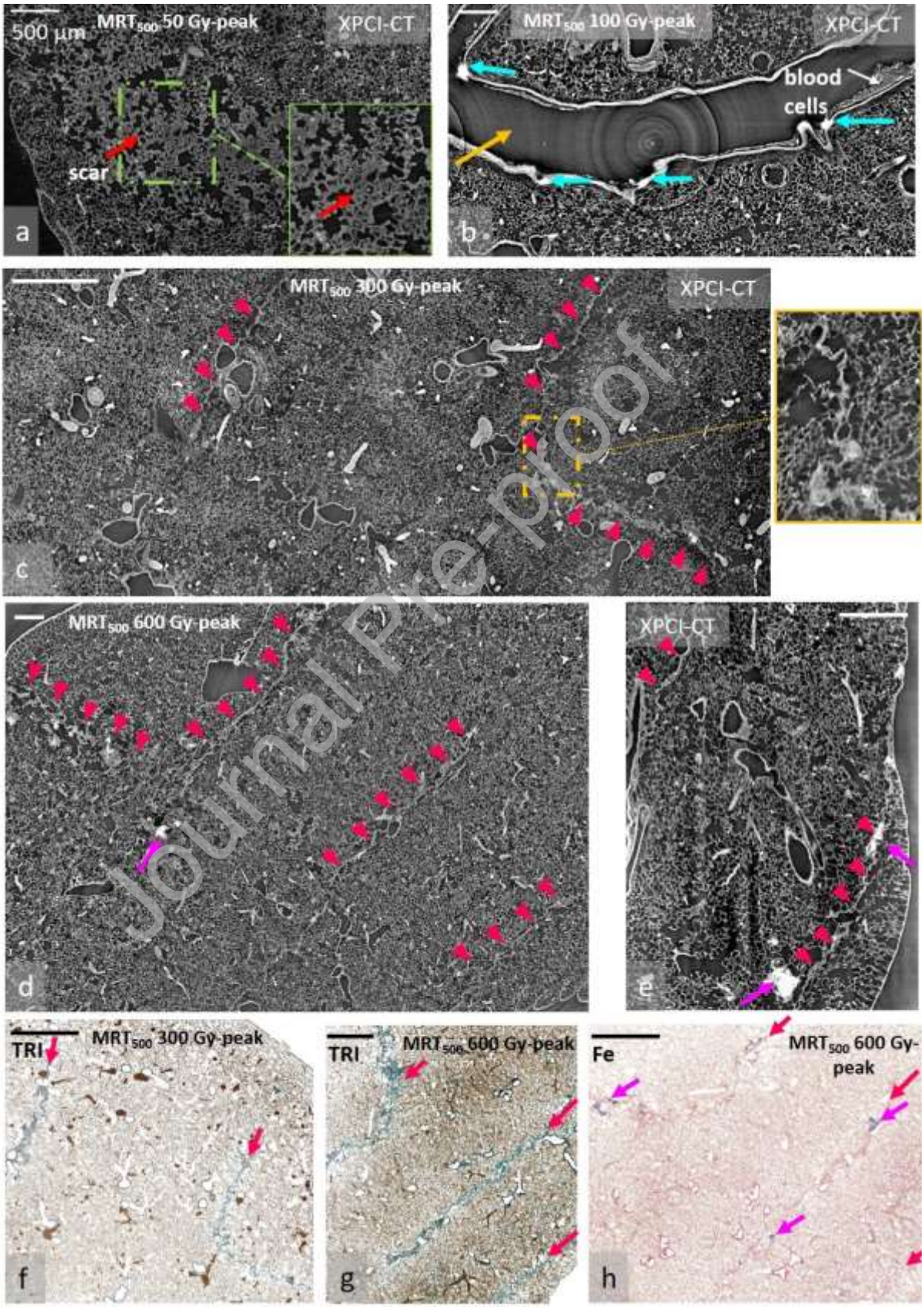

Figure 4d) all the microbeam paths are visible as stripe-shaped scars that develop straight in depth as visualized in the oblique reslicing (

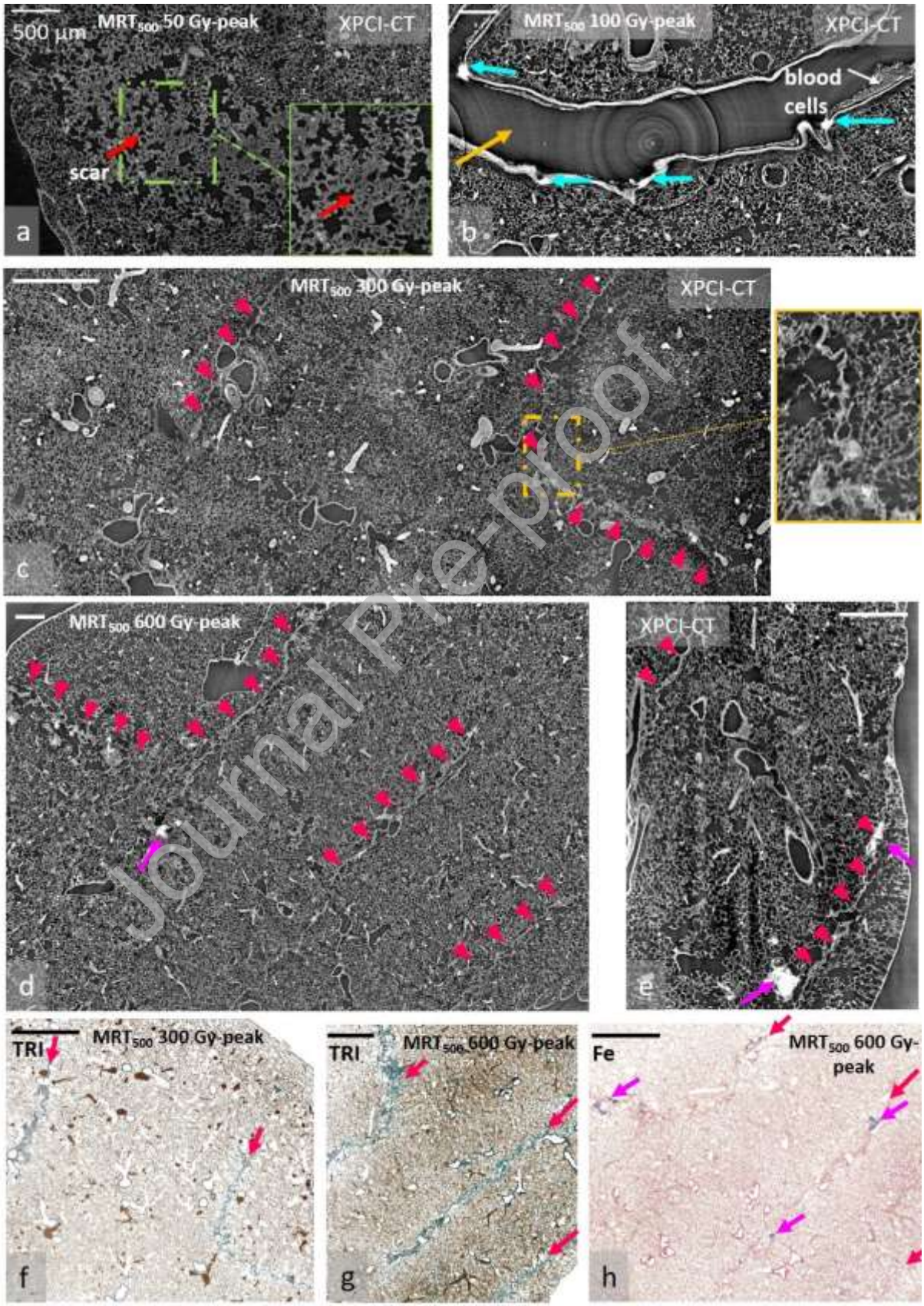

Figure 4e). In some cases, as also visible in the showcases of the MRT_{500} 300 and 600 Gy-peak groups, microbeam scars do not appear always as a straight line but as “bent” “L”- shaped one. The scars

within the tissue due to the microbeams are recognizable in the TRI histologies as green structures (

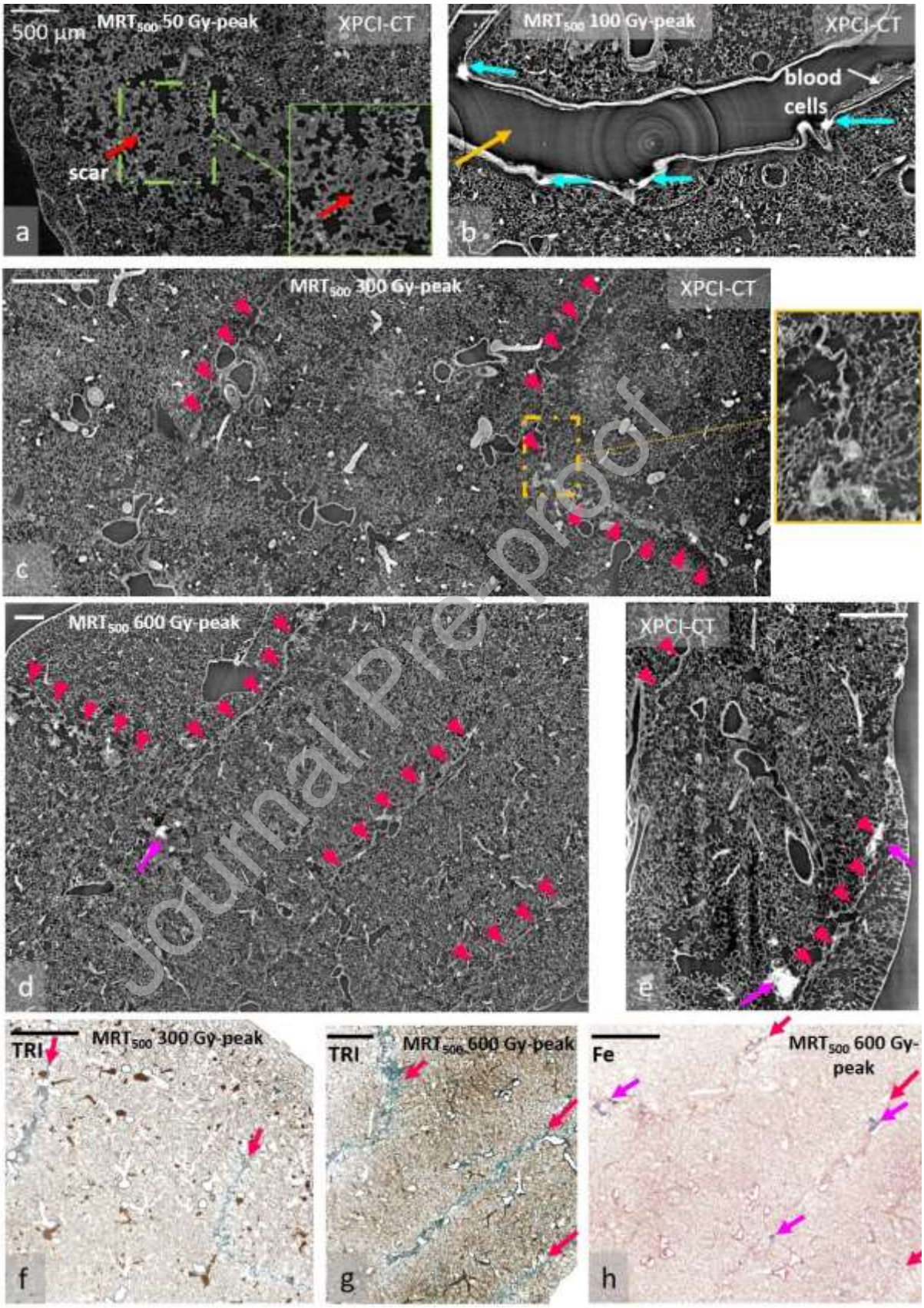

Figure *4*f-g). These results were used to interpret the XPCI-CT images of

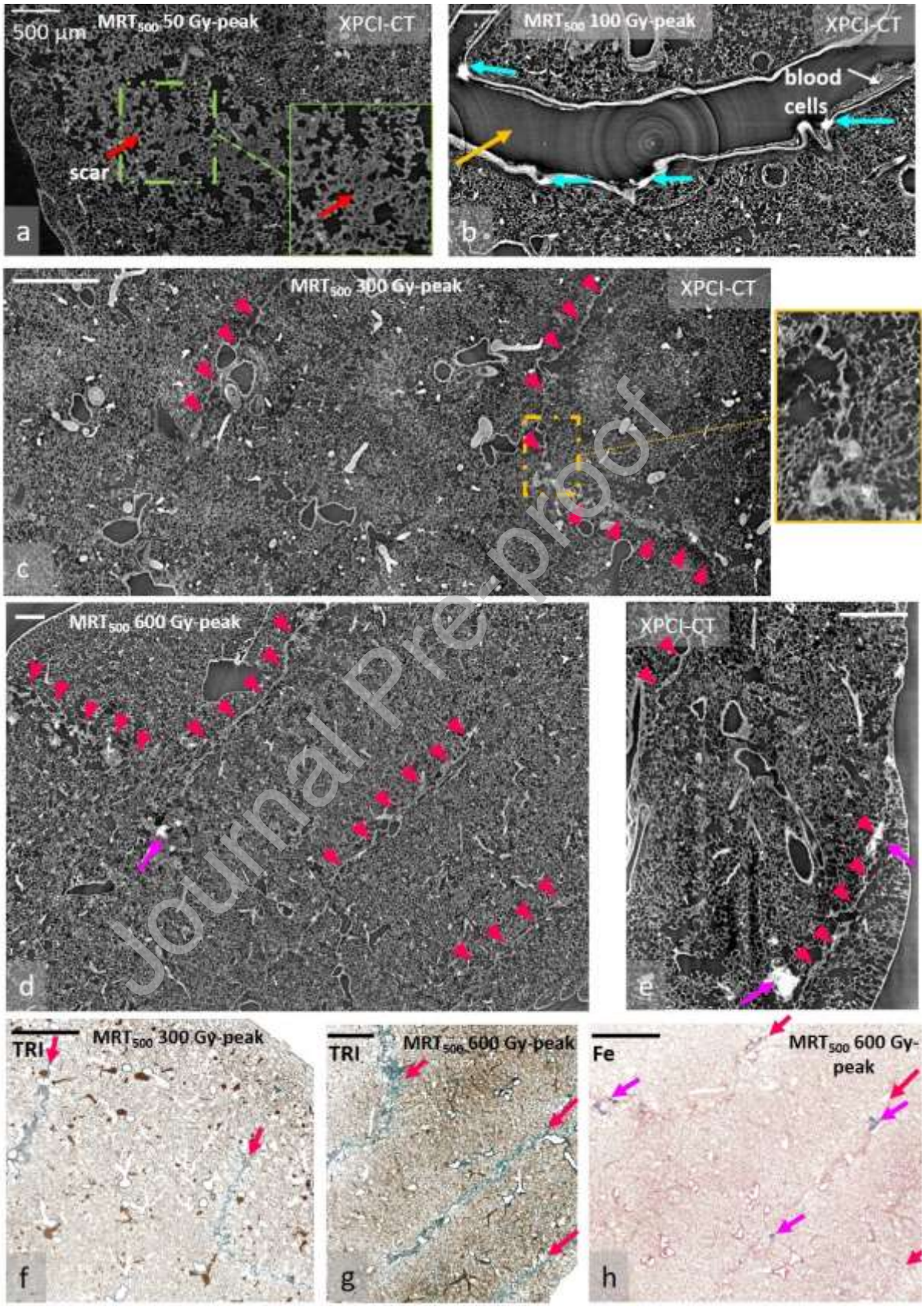

Figure 4c and

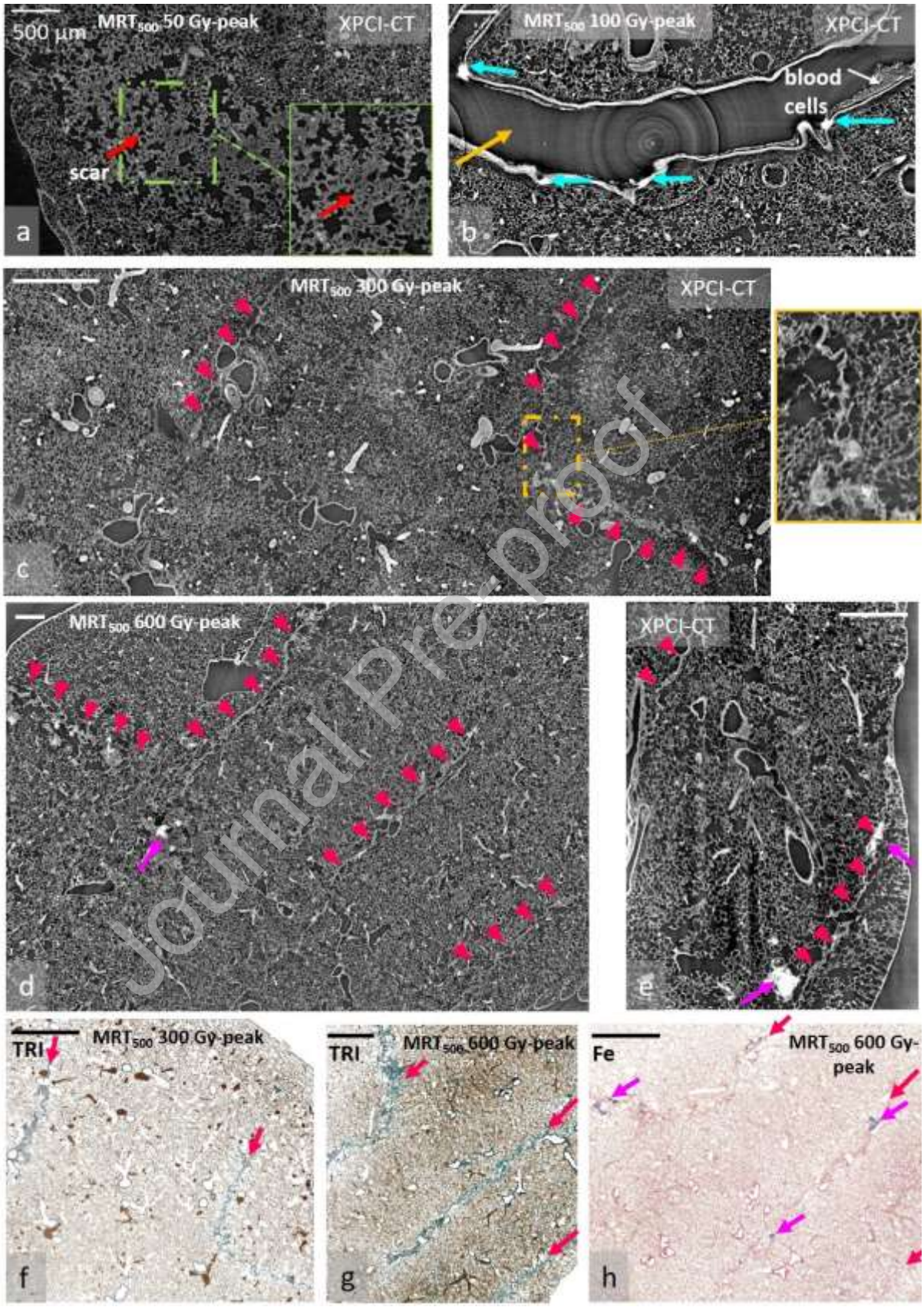

Figure 4d. In the samples of the MRT_{500} 600 Gy-peak group, Fe deposits within the scars are detected by XPCI-CT (

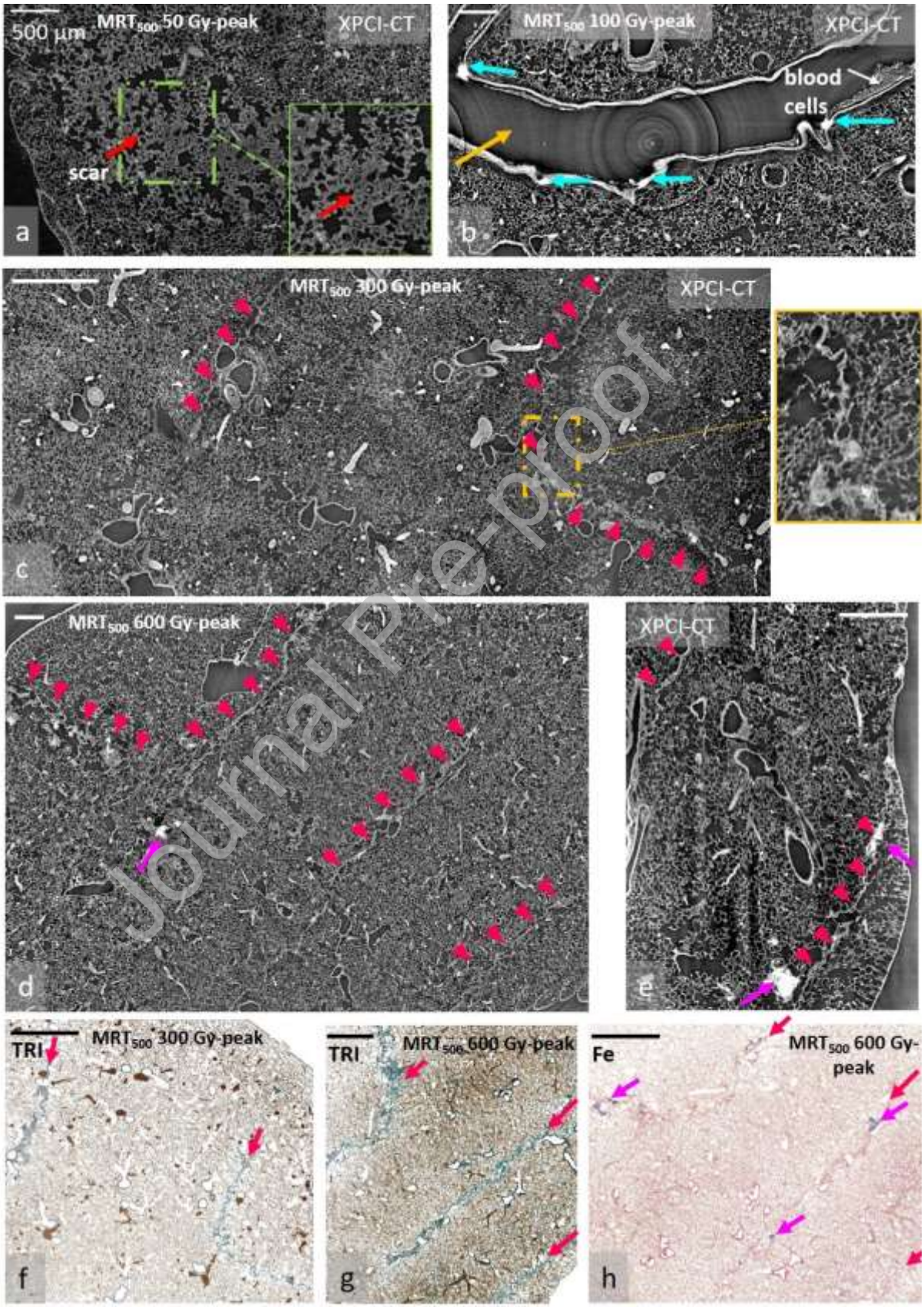

Figure 4d) as confirmed by the Fe-stained histology (

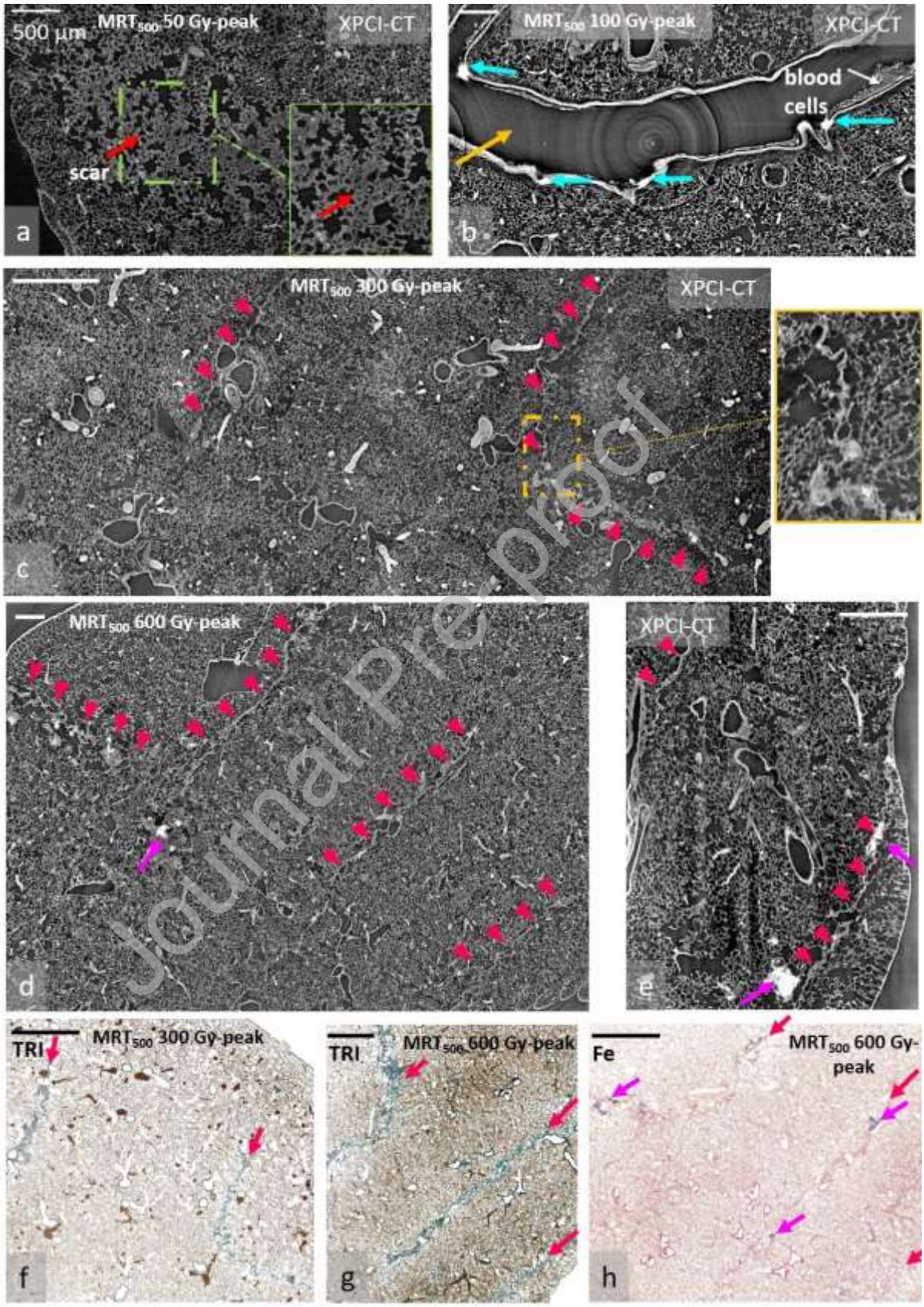

Figure 4h).

Imaging of the effects of BB radiotherapy on lungs

The lung tissue alterations due to BB irradiation with doses of 30 and 50 Gy are reported in Figure 5. Here, findings of one sample for each delivered dose are reported since the chosen specimens are representative of the RT group. The scarring tissue induced by irradiation with BB and 30 Gy is shown on the coronal and sagittal images in Figure 5a-b. The irradiated tissue presents a quasi-uniform alveolarization with scars appearing in limited regions and the 3x zoom image in the inset of

Figure 5a reveals a thickening of the alveolar walls with respect to the case of healthy alveoli (see

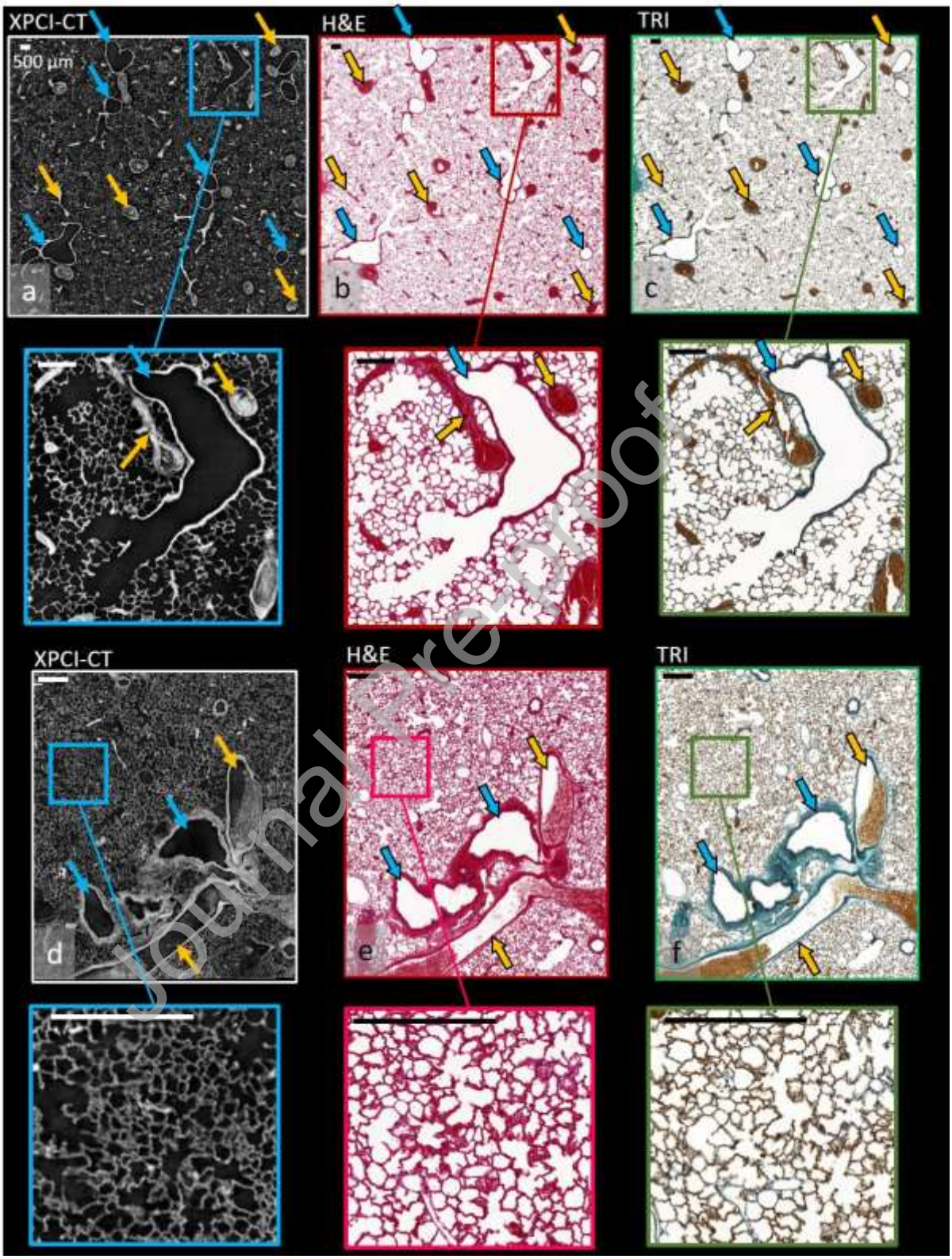

Figure **1**). In the sagittal view, we can also observe an extended tissue damage appearing as a reshaping of the alveolar spaces (white arrows). Images in Figure 5c-e present XPCI-CT data of a 50

Gy lung tissue irradiated in BB mode: a more invasive damage is visible with respect to the 30 Gy case. The morphological changes within the lung tissue are clearly discernible in XPCI-CT images: the interface and discontinuity between the irradiated and non-irradiated portions of the tissue is marked by the dashed red line in Figure 5d. In the irradiated region, the alveolar sacs are destroyed and the typical regular tissue structure is lost. Within this scarred tissue, highly absorbing features are detected (magenta arrows), identified as Fe deposits. The non-irradiated portion of the tissue presents more regular alveoli and septa similarly to the control cases. The reslicing (Figure 5e) of the XPCI-CT dataset, obtained along the cyan line of Figure 5c, shows that the scar presents thicker alveolar walls on the surface of the sample. As we move inside the lung, another highly absorbing feature (green arrow) is visible. By adjusting the image windowing (inset of Figure 5e), it is possible to recognize the inner structure of a collagenous nodulus. The correlation with histology is not given for these samples since the XPCI-CT signal arising from the presented radio-induced lesions has been

already validated with histology for the MRT-treated samples (

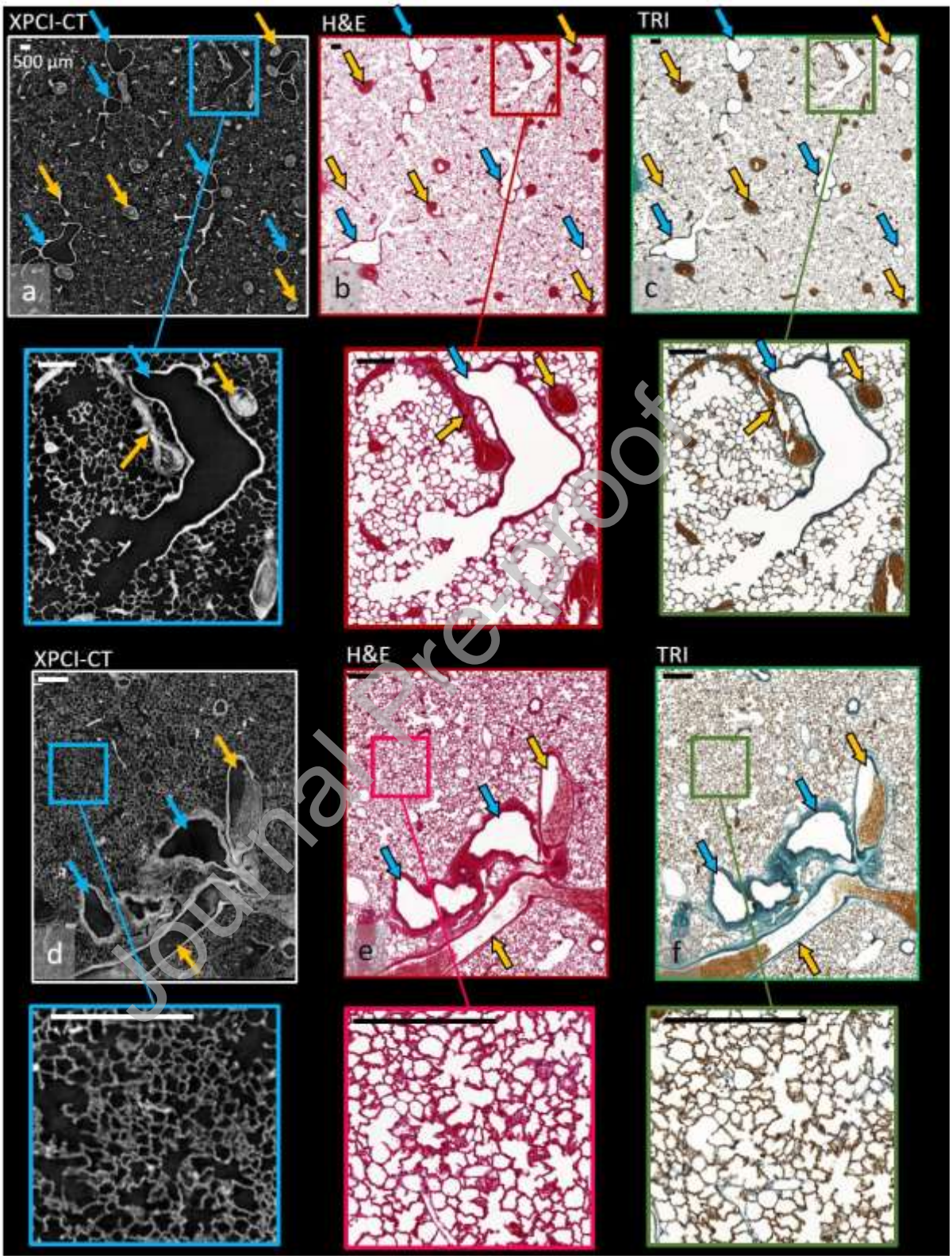

Figure **1-**

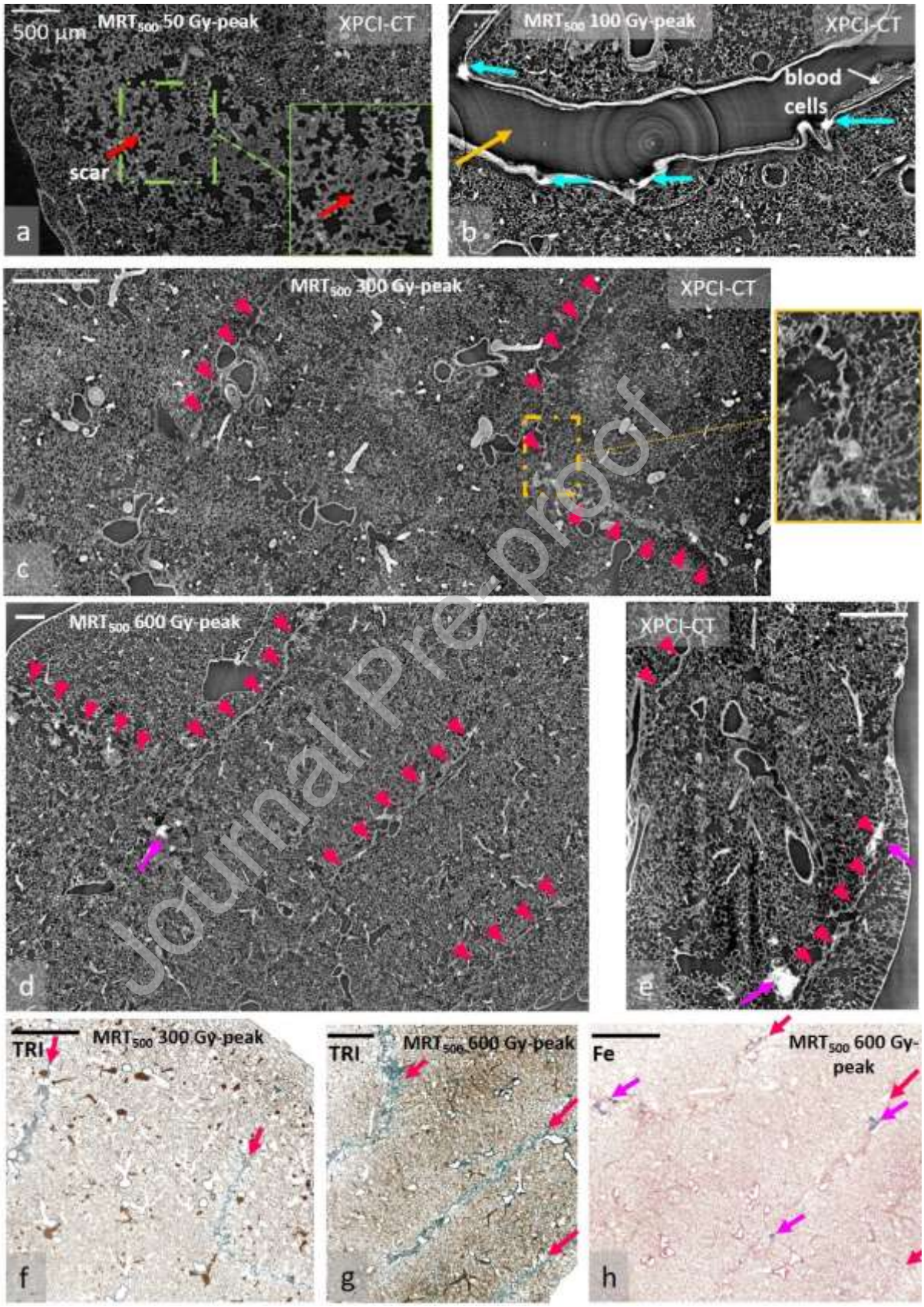

Figure *4*).

Segmentation of the scarring tissue

The quantification of the total amount of fibrotic tissue over the available imaged volume was performed on all the three samples of each group following 3D segmentation and rendering of the segmented scars over the surrounding tissue (

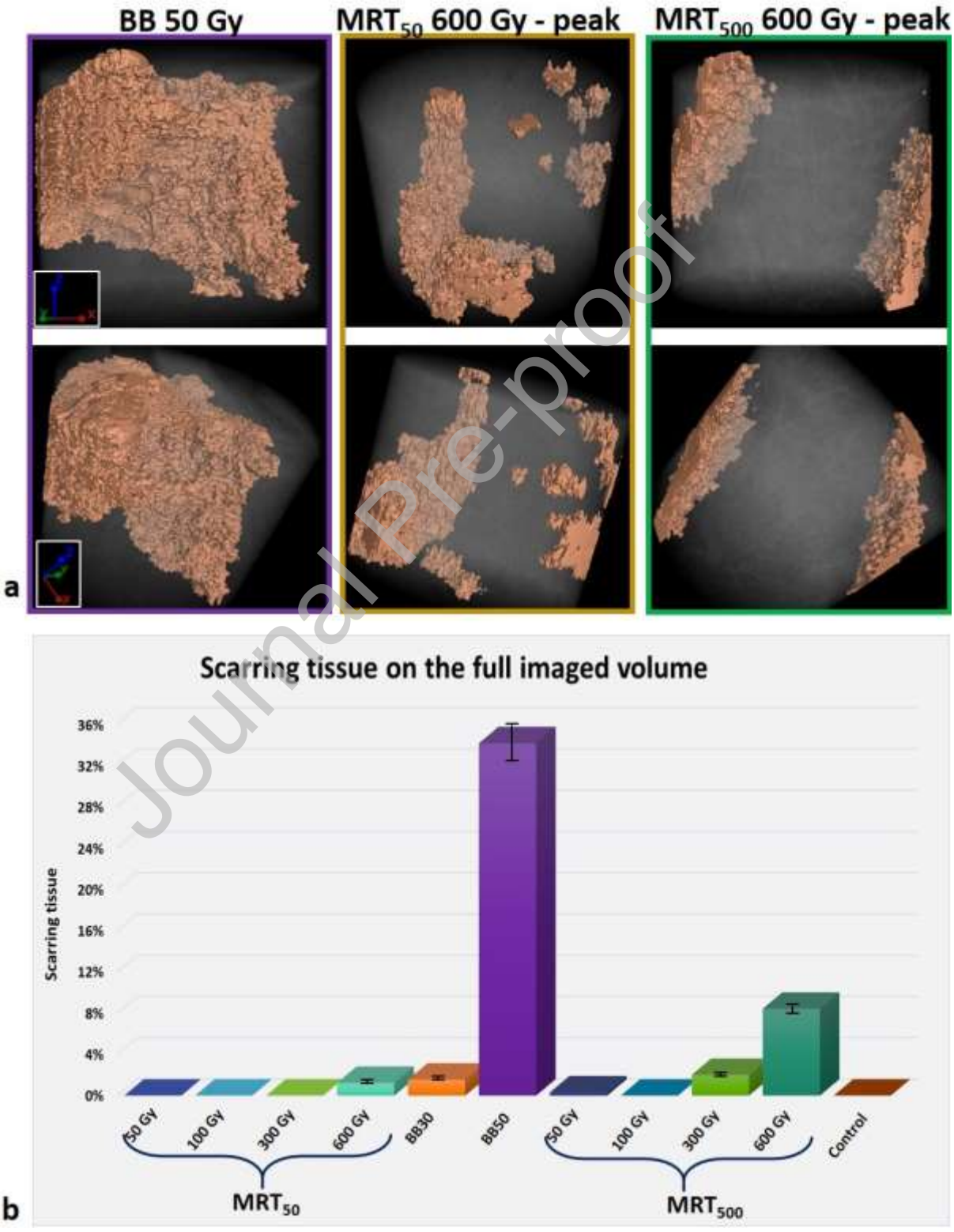

Figure **6**a). The segmentation discriminated both the extended scar produced by a BB, isolated spot-like and planar shaped scars typical of MRT_{50} and MRT_{500}.

One representative sample per group was chosen to build a chart of the fibrotic tissue detected over the full imaged volume (

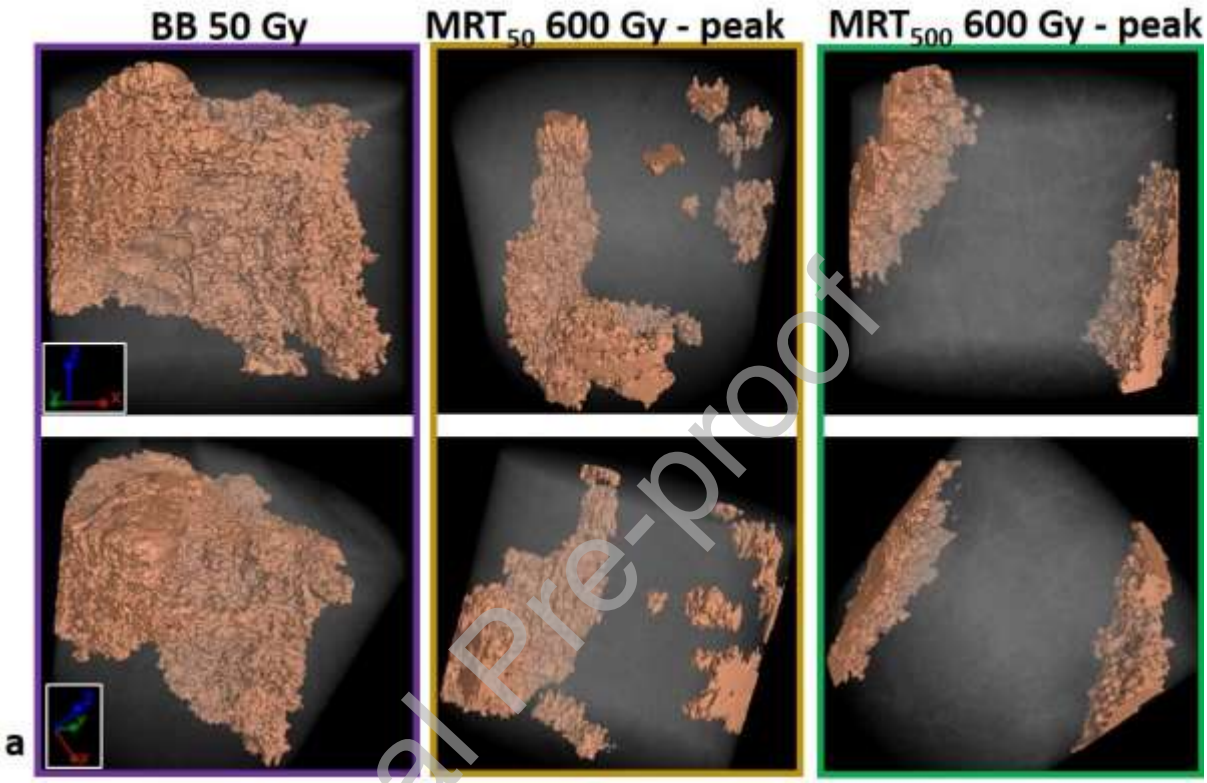

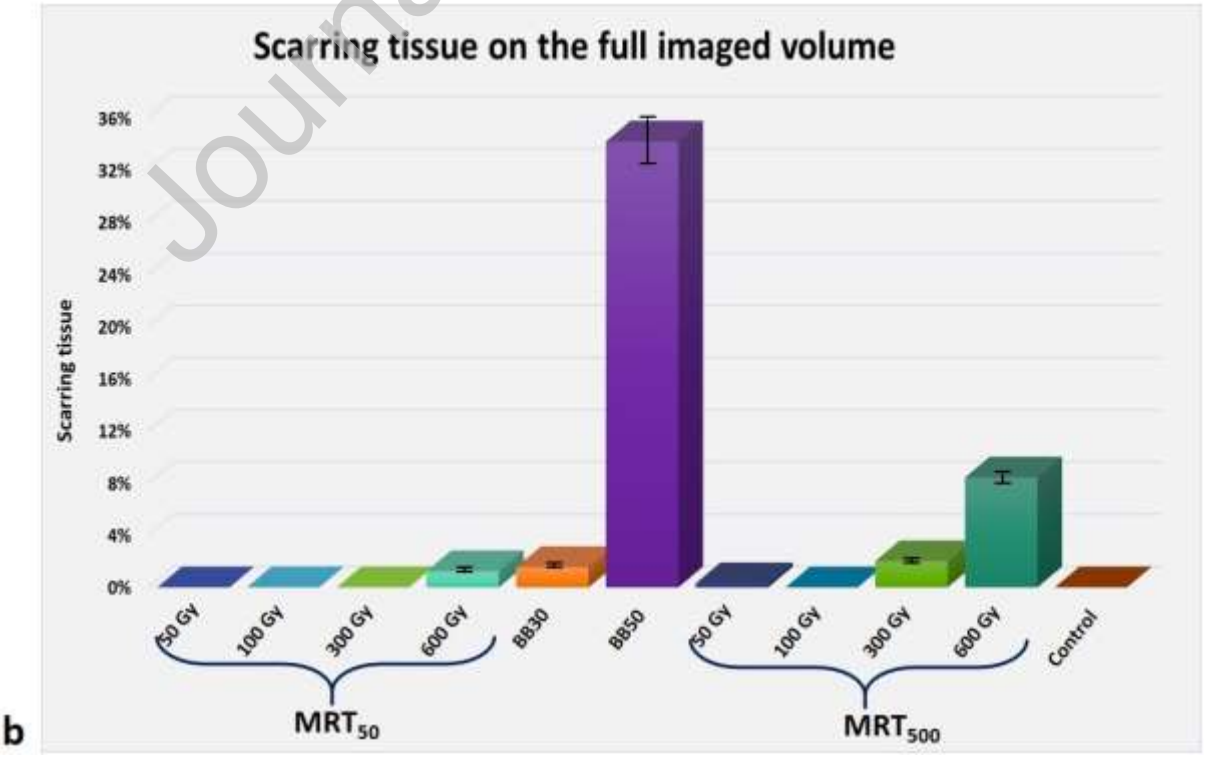

Figure **6**b). The chart of

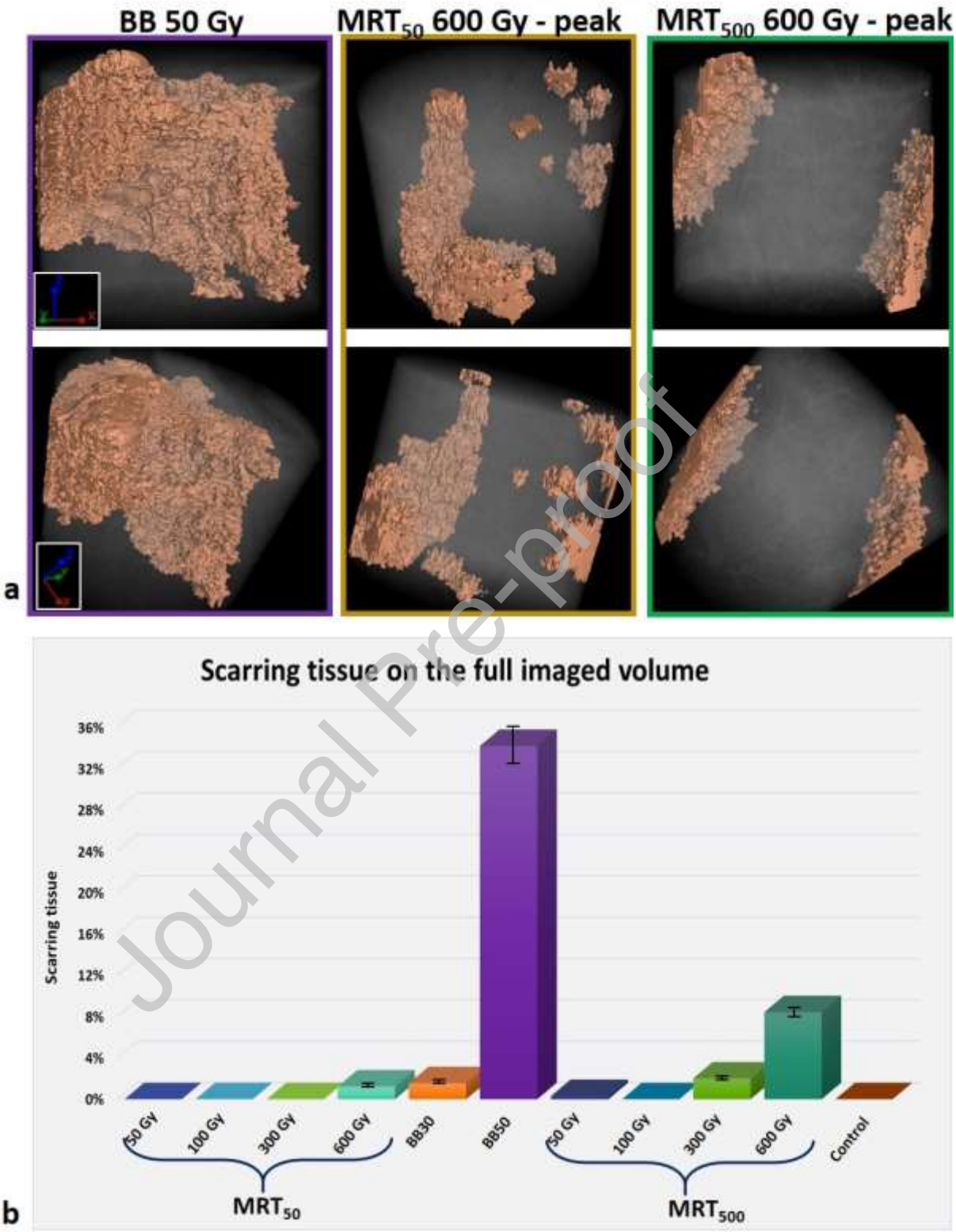

Figure **6**b confirms that the BB 50 irradiated samples are the ones showing the largest amount of fibrotic tissue while for MRT_{50} and MRT_{500} treated samples, the highest peak doses produce the most severe damage.

Discussion

XPCI-CT enables 3D imaging of lung tissue from full organs down to a sub-micrometric resolution, showing, with high detail, the tissue anatomy from acini volumes down to alveolar levels (

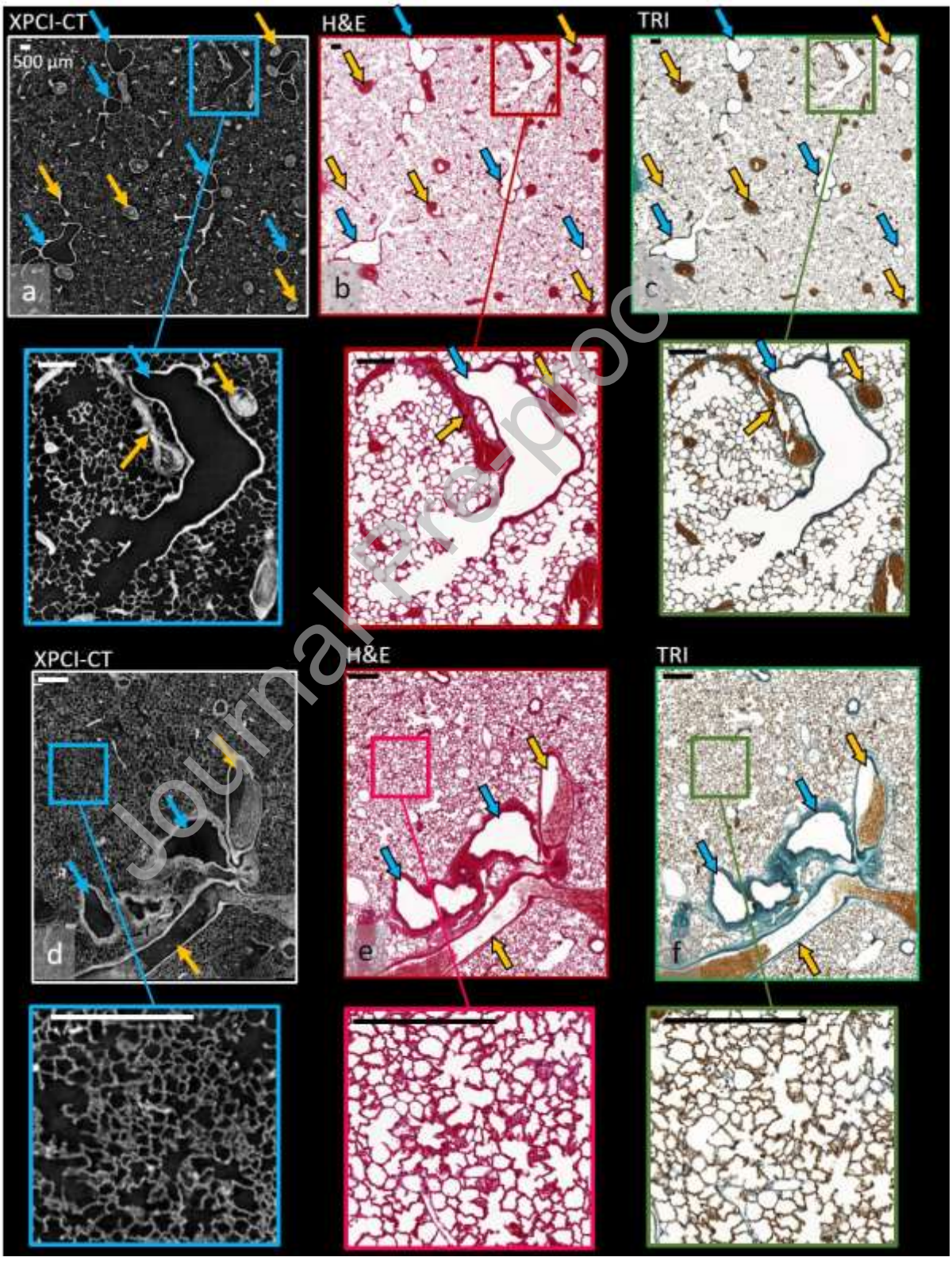

Figure **1**). Airways and blood vessels can be followed in 3D and alveolar septa are clearly resolved. The highly detailed lung XPCI-CT data allow sophisticated 3D quantitative examinations (12) enabling as well saccular volume computation and topological analysis of the air-to-tissue surface (29). We applied *post-mortem* semi-quantitative XPCI-CT as a label-free density-based 3D morphological technique for high resolution and high sensitivity lung imaging. We investigated and visualized the distinctive effects on the tissue following the administration of RTs characterized by different beam geometries.

This study shows for the first time XPCI-CT data of the effects of BB, MRT_{50} and MRT_{500} RTs on lung tissue delivered *in-vivo* using both 1.63^3 μm^3 and 0.65^3 μm^3 voxel XPCI-CT images with a resolution similar to histology, demonstrating the high diagnostic power of this technique. Overall, the 1.63^3 μm^3 voxel size allows detecting and distinguishing several features within the irradiated tissue, while the 0.65^3 μm^3 voxel images show the same details but with an increased quality of the image in terms of sharpness. Nevertheless, the field of view (FOV) of CT images decreases as the spatial resolution increases and 1.63^3 μm^3 voxel size was found as the optimum compromise between image quality and FOV for rat lung tissue analysis.

XPCI-CT showed that BB irradiation induces scars within the treated lung areas with dimensions extending as the dose increases. Overall, the alveolarization appears less regular in BB-irradiated

lung with respect to control tissues (Figure 5 vs

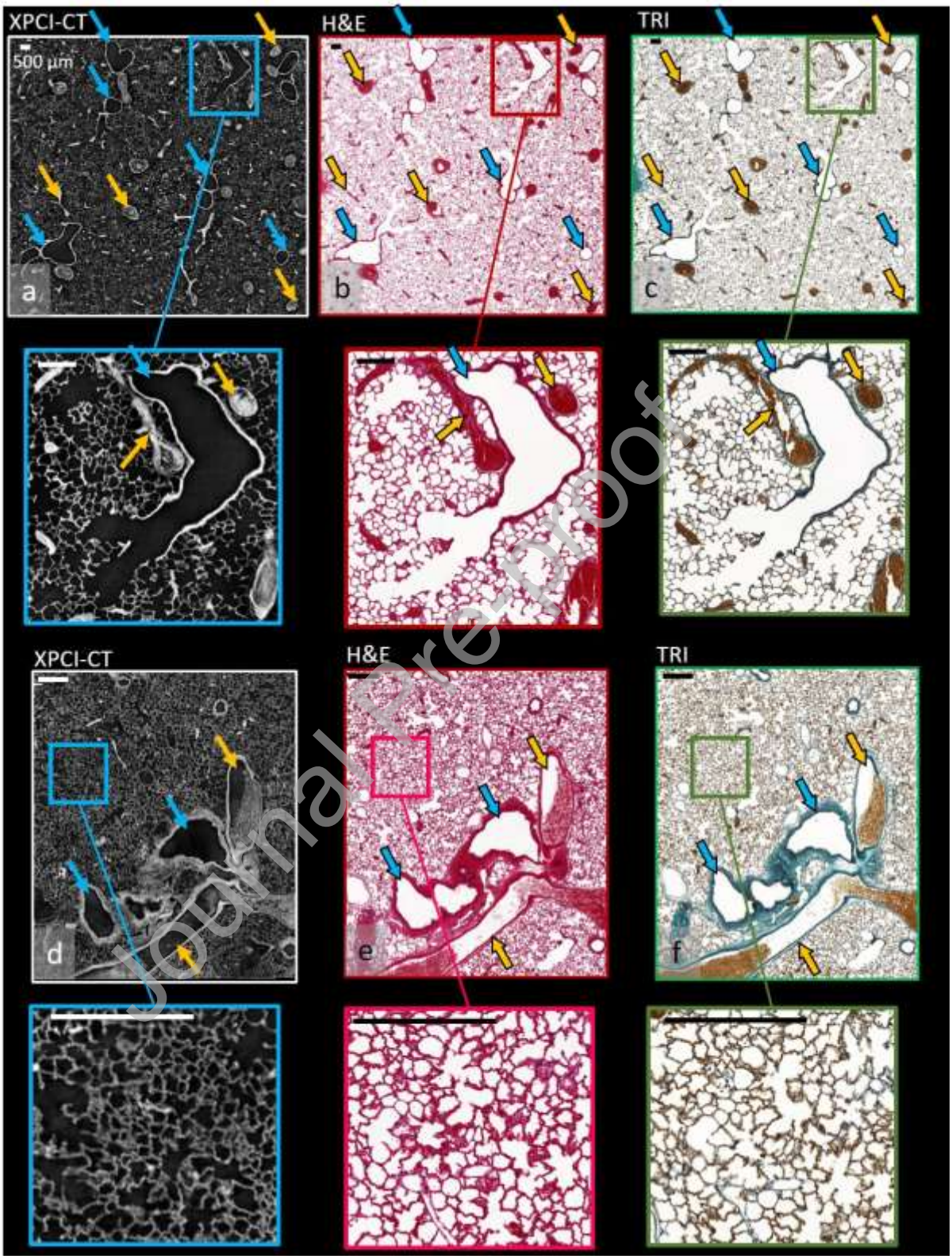

Figure **1**). The interface between the irradiated and not-irradiated areas is clearly demarked as a sharp edge in the BB 50 Gy case (Figure 5c-d). The collagen nodulus of the BB 50 Gy sample in Figure

5e is ~10 times bigger than those detected in the MRT_{50} and MRT_{500}-treated lungs, thus confirming that BB irradiation at 50 Gy is the most aggressive among the here presented ones. This result is also confirmed by the fibrosis segmentation study, (

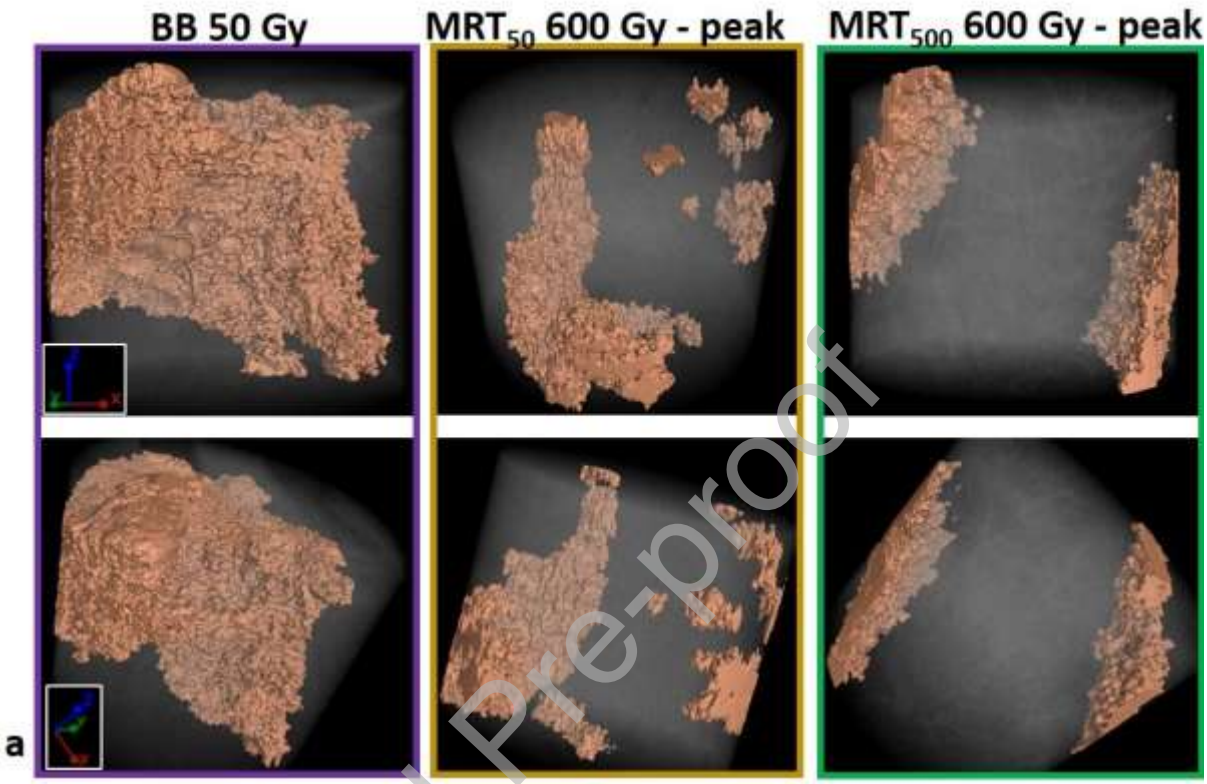

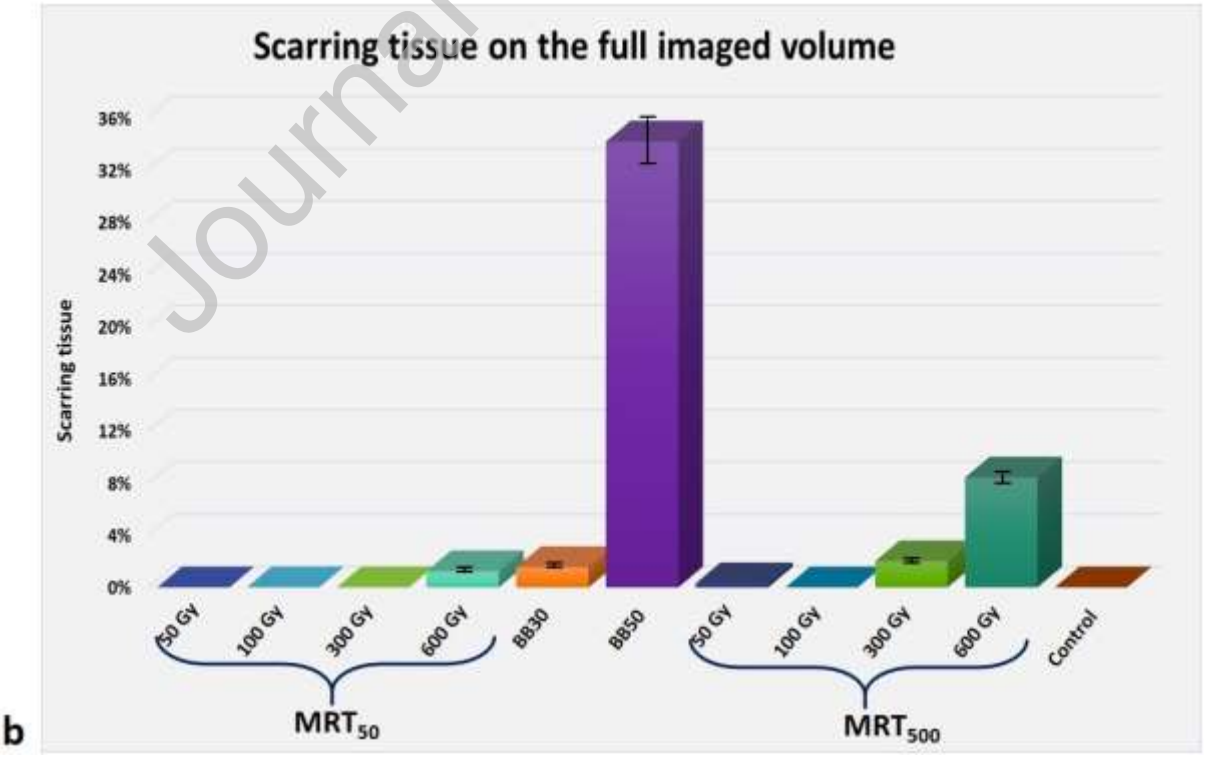

Figure **6**a) and by the histogram of

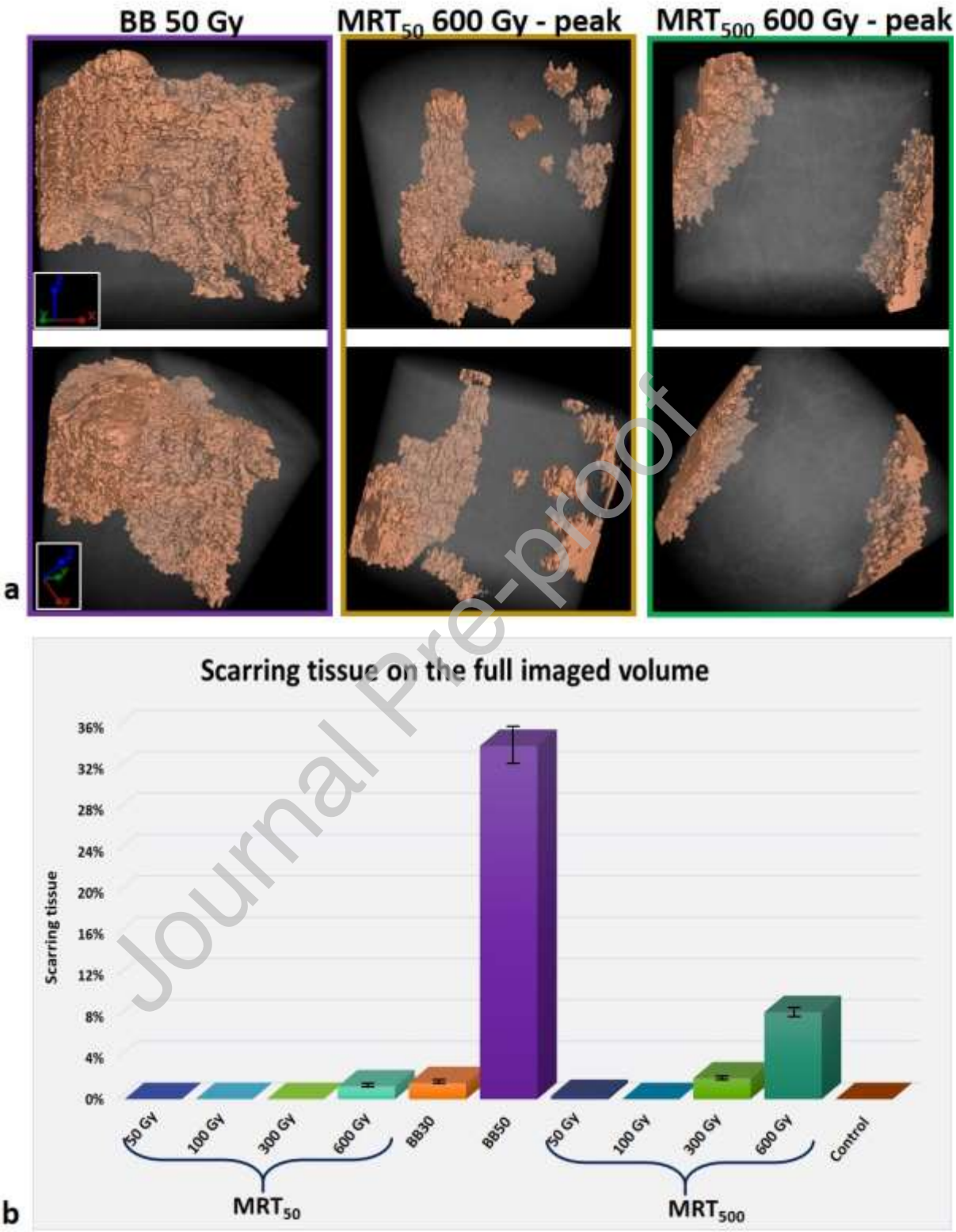

Figure **6**b showing that BB 50 Gy irradiation produces the largest fibrotic content within all the considered cases.

As shown in

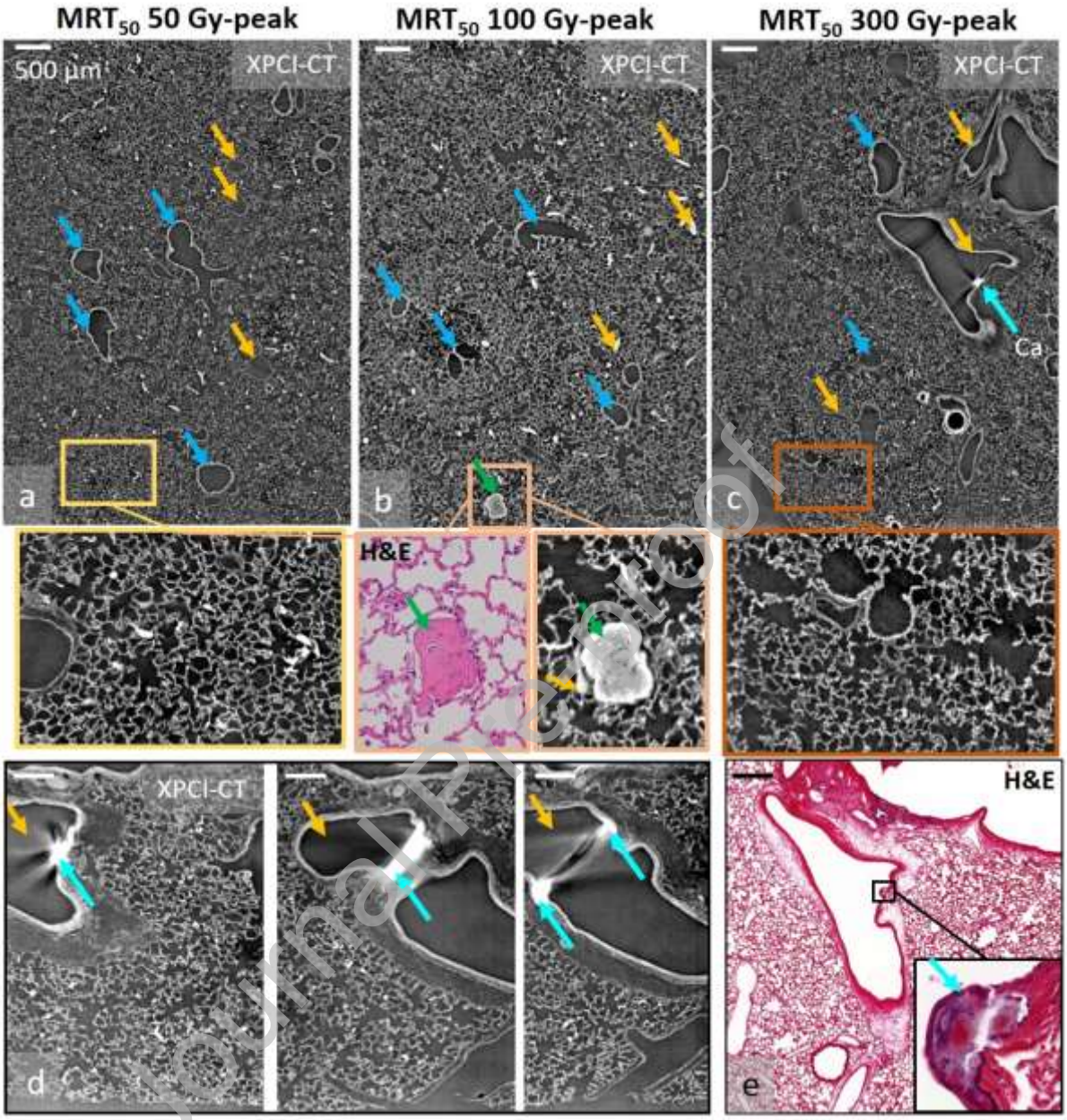

Figure 2 and

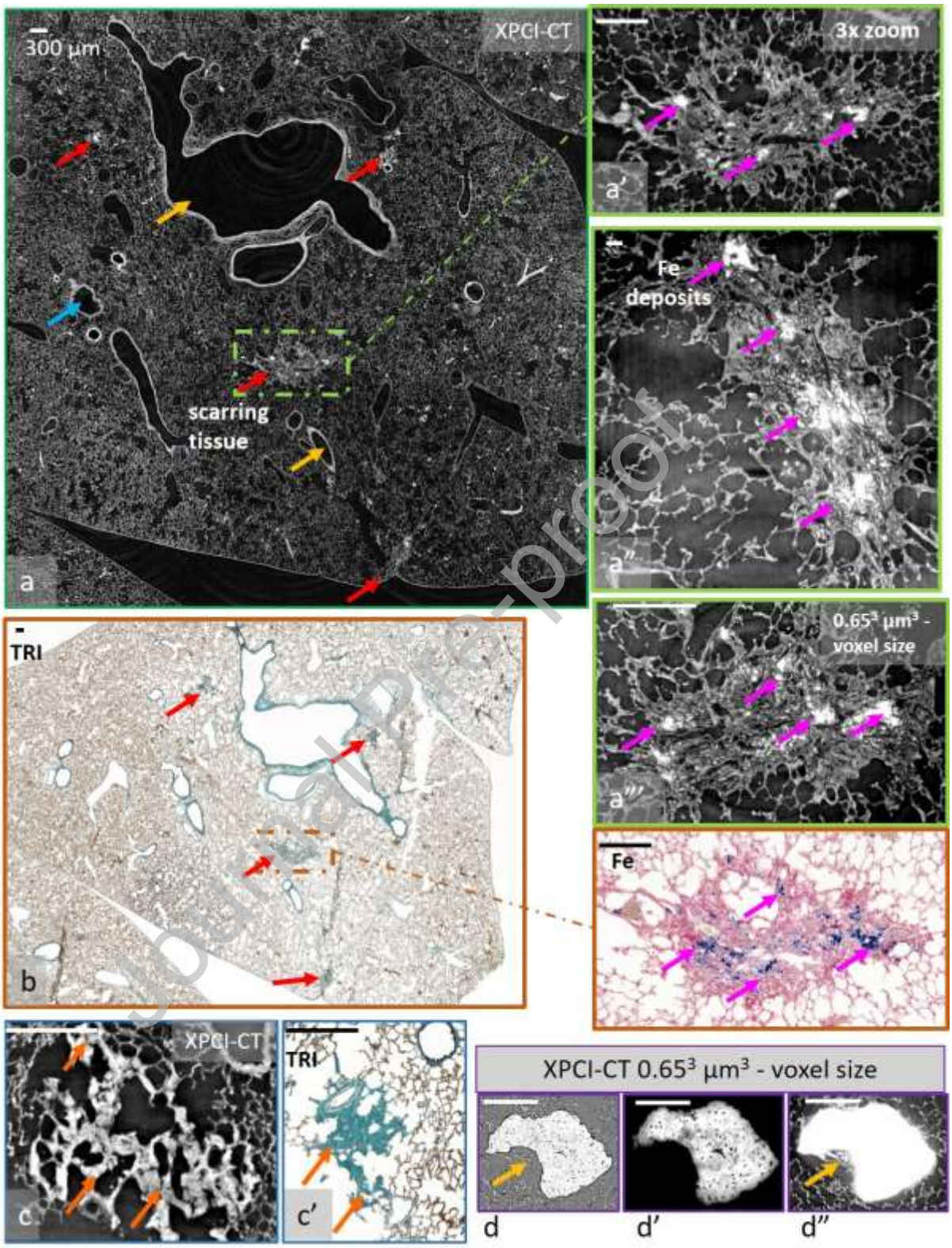

Figure 3, the MRT_{50} irradiation causes isolated scars with Fe deposits and small collagen noduli within the tissue. All the MRT_{50} 50 Gy-peak treated lungs are comparable, in terms of alveolar shape

and dimensions, to the control samples; instead MRT_{50} 100 Gy-peak lungs only show radio-induced collagen noduli. Two out of the three specimens of the MRT_{50} 300 Gy-peak group are also comparable to controls in terms of tissue morphology; only one lung tissue presents an extended calcification that replaced a portion of the endothelium on a blood vessel (

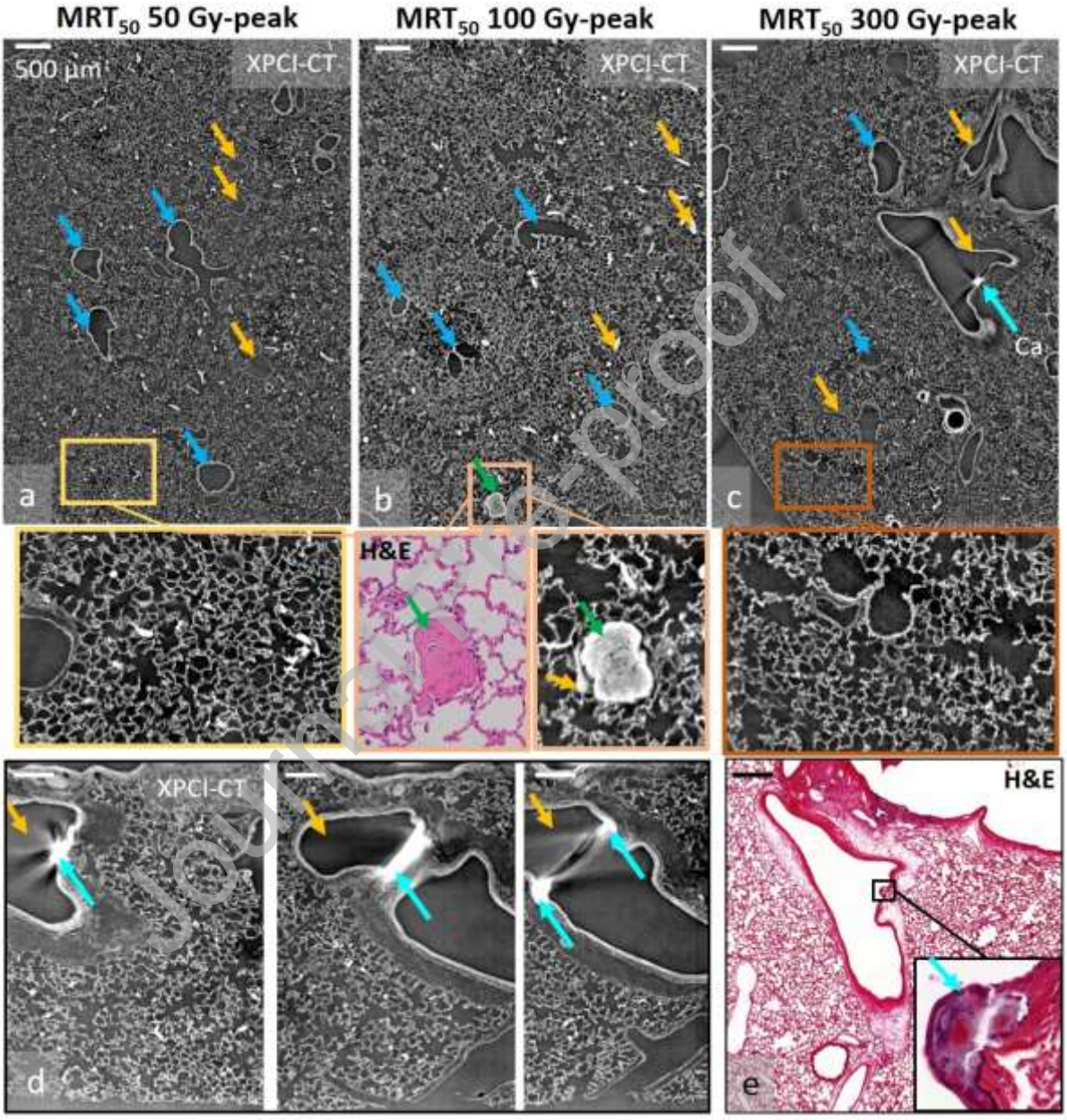

Figure 2d). The three rat lungs irradiated with MRT_{50} 600 Gy-peak contain scars, Fe particles, collagen noduli and thicker alveolar septa appearing in the healthy tissues (

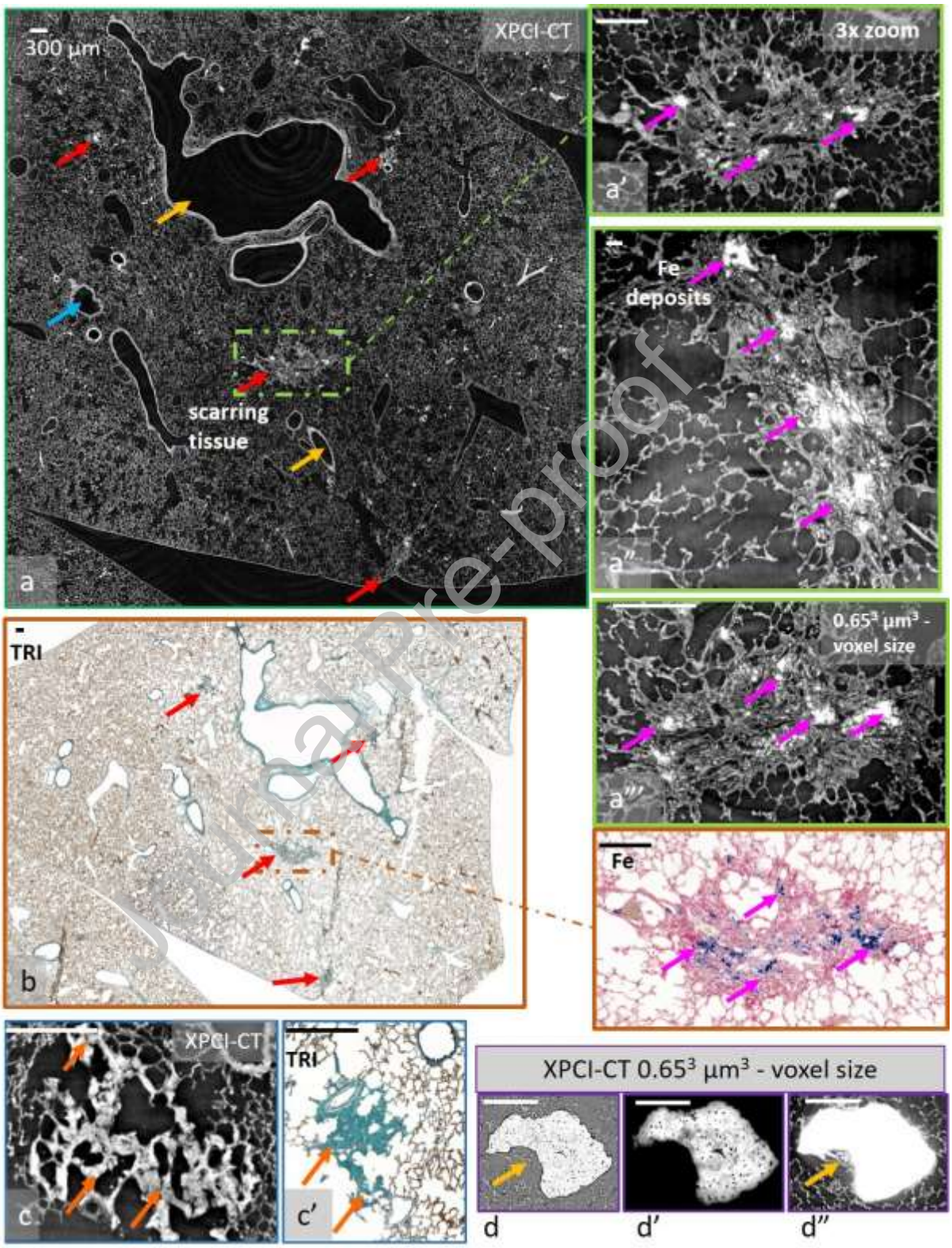

Figure **3**). In none of the MRT_{50}-treated samples the microbeam paths are detected; given the fact that all the animals have been sacrificed 12 months after the irradiation, this could be a sign that lung tissue can repair micrometric damages without showing extended scaring or damaged tissue even if the delivered dose is locally up to hundreds of Gray.

With respect to MRT_{50}-irradiated lungs, the effects of MRT_{500}-treated tissues are found to be more pronounced. Even when using 50 Gy, i.e. the lowest peak dose, collagen noduli, blood vessel calcification and scarring tissue are clearly visible in all the examined specimens and, as the dose

increases, MRT_{500} paths become progressively more noticeable as stripe-shaped scars (

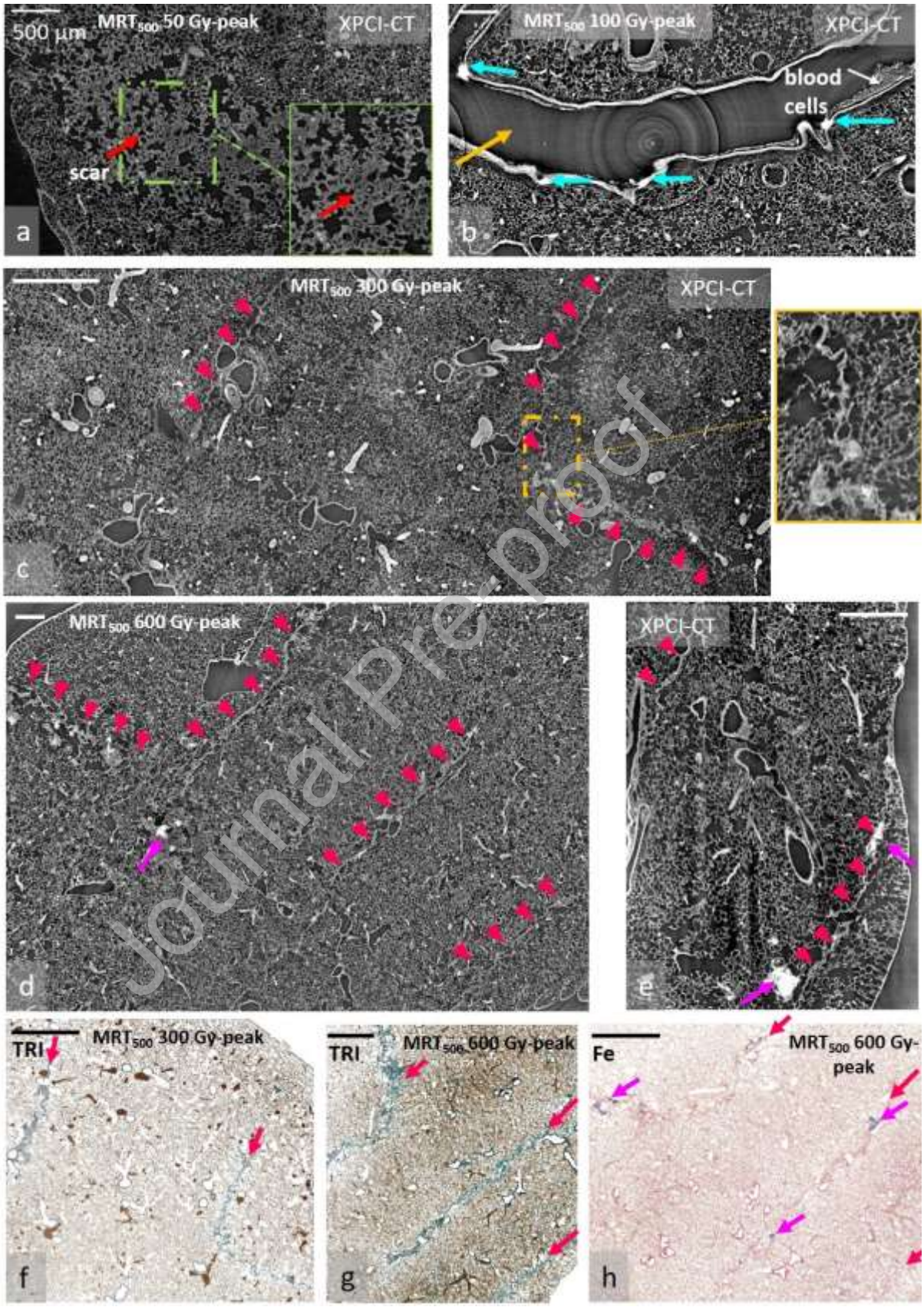

Figure *4*). Here, the scars prevalently have a straight planar shape if visualized in 3D. Nevertheless, in a few cases, it is possible to observe a folded stripe-MRT_{500} path: these distortions are likely due to the sample manipulation during the extraction and fixation procedures. In principle, all the MRT_{500}-induced scars should present planar shape reproducing the straight path of the delivered X-ray beam array. However, in some cases, this forecast is not met for *ex-vivo* images since the sample underwent some local morphological alterations during the extraction and fixing procedures that are detectable with the accuracy provided by XPCI-CT. The great advantage upon histology is that XPCI-CT is a dissection-free technique that does not need further tissue manipulation after the fixing procedure. Hence, the used technique is free from tearing and stretching artefacts caused by the tissue cutting and can retrieve the information of the sample manipulation, while histology, requiring the tissue to be cut in thin slices, is affected by additional artefacts and misses to provide volumetric information. While XPCI-CT technique provides great and highly detailed anatomical representation of full specimens, its signal is biologically nonspecific and can differentiate and delineate with accuracy structures on the basis of their electronic density difference. Correlation with standard histology is a crucial step in the analysis process, which can help identifying the nature of unknown structures. This is important in particular in the training phase of XPCI-CT data interpretation. Furthermore, XPCI-CT can be exploited to identify and accurately localize the region of interest within the fixed samples without sample sectioning. This knowledge could then guide the following examination via histology limiting the sectioning and staining procedures only to the part of interest.

The quantification study based on the segmentation of the fibrotic tissue gives clear evidence on how XPCI-CT enables an accurate 3D rendering of the effects of the radiation on lungs and allows enhanced visualization and characterization of the features of interest e.g. fibrosis within the full organ. Furthermore, this 3D full organ analysis confirms that the irradiation geometries that impact the most the healthy tissue are BB 50 Gy, BB 30 Gy, MRT_{50} 600 Gy-peak and MRT_{500} with 300 and 600 Gy as peak doses, as reported in XXXX et al. (22).

Overall, XPCI appears as a technique that allows imaging soft tissues and especially lungs at high spatial and contrast resolutions; it shows the potential to become a complementary and/or alternative tool to standard histology and premises for *in-vivo,* full organ coverage method for disease and treatment monitoring, thus filling in the gaps of the currently available lung imaging techniques (an overview is provided in the "State of the art on clinical lung imaging" section of the supplementary material).

In-vivo applications of XPCI-CT have started and are running for some specific applications on human and small animals, such as: *i)* for propagation-based XPCI mammography and breast CT with both synchrotron sources and conventional X-ray tubes (30; 31; 32);*ii)* for the diagnosis of arthritis with grating interferometric methods (33; 34); and *iii)* for the detection of lung diseases as fibrosis (35) and emphysema (36; 37) with X-ray dark field grating interferometric imaging.

Conclusions

This study proves that the imaging-based methodology here applied allows visualizing *ex-vivo* with high contrast and detail in 3D radiation-driven features specific of the delivered beam configurations. We could recognize RT-induced stripe-shaped scars, alveolar wall thickening, fibrotic tissue, collagen noduli and hyperdense structures which revealed being Fe deposits and calcifications on blood vessels, as determined by correlation with histology. Furthermore, thanks to the segmentation of the fibrotic tissue, it was possible to clearly highlight that all the irradiation protocols produced a fibrotic content below 10% (with the exception of the BB50 group, for which values reach the 34%). Additionally, the BB50 treatment proved to be highly toxic for the healthy lung structures. All the features detected with high-resolution XPCI-CT were visualized via histology and vice-versa; this study proves that no dose threshold effect is present in terms of radio-induced detectability, at least for the considered irradiation groups. XPCI-based virtual histology could therefore be included in the workflow of pathological assessment of tissue samples, currently performed by means of standard histology, for quantifying fibrotic lesions within the lung organ.

Provided that standard histology allows the identification of the imaged structures, XPCI-CT can give complementary information of detailed anatomical and structural 3D view of the sample and can guide the realization of conventional histology owing to its 3D capabilities and the possibility of virtually navigating within samples. This study puts the basis for an *in-vivo* application of XPCI-CT as an imaging modality for the follow-up of lung radiotherapy. This assertion is founded on the demonstration that XPCI-CT can detect and discriminate the radio-induced effects caused by different irradiation geometries and doses in a small animal model.

References

1. Müller, M., Kimm, M. A., Ferstl, S. et al. Nucleus-specific X-ray stain for 3D virtual histology. *Sci Rep-Uk* 2018 8:17855.

2. Albers, J., Pacilé, S., Markus, M. A. et al. X-ray-Based 3D Virtual Histology-Adding the Next Dimension to Histological Analysis. *Mol Imaging Biol* 2018 20:732-741.

3. Toepperwien, M., van der Meer, F. Stadelmann, C. and Salditta, T. Three-dimensional virtual histology of human cerebellum by X-ray phase-contrast tomography. *P Natl Acad Sci USA* 2018 115(27): 6940-6945.

4. Albers, J., Markus, M. A., Alves, F. and Dullin, C. X-ray based virtual histology allows guided sectioning of heavy ion stained murine lungs for histological analysis. *Sci Rep* 2018 8:7712.

5. Chakravarty, M. M., Bertrand, G. Descouteaux, M., et al. The Creation of a Brain Atlas for Image Guided Neurosurgery Using Serial Histological Data. 2003 Edited by Springer Berlin Heidelberg.

6. Saccomano, M., Albers, J., Tromba, G. et al. Synchrotron inline phase contrast uCT enables detailed virtual histology of embedded soft-tissue samples with and without staining. *J Synchrotron Radiat* 2018 25: 1153-1161.

7. Barbone, G. E., Bravin, A., Mittone, A. et al. Establishing sample-preparation protocols for X-ray phase-contrast CT of rodent spinal cords: Aldehyde fixations and osmium impregnation. *J Neurosci Meth* 2020: 108744.

8. Hooper, S. B., Kitchen, M. J., Siew, M. L. L., et al. Imaging lung aeration and lung clearance at birth using Phase Contrast X-ray Imaging. *Clin Exp Pharmacol P* 2009 36(1): 117-25.

9. Lewis, R. A., Yagi, N., Kitchen, M. J., et al. Dynamic imaging of the lungs using x-ray phase contrast. *Phys Med Biol* 2005 **50**(21): 5031-40

10. Lovric, G., Mokso, R., Arcadu, F. et al. Tomographic in vivo microscopy for the study of lung physiology at the alveolar level. *Sci Rep-UK* 2017 7(1): 12545.

11. Fardin, L., Broche, L., Lovric, G. et al. Imaging atelectrauma in Ventilator-Induced Lung Injury using 4D X-ray microscopy." *Sci Rep-UK* 2121 11 (1): 4236.

12. Broche, L., Pisa, P., Porra, L., et al. Individual Airway Closure Characterized In Vivo by Phase-Contrast CT Imaging in Injured Rabbit Lung. *Crit Care Med* 2019 47 (9) 774-781.

13. Zamir, A., Arthurs, O. J., Hagen, C. K., Diemoz, P. C., Brochard, T., Bravin, A., Sebire, N. J., Olivo, A. X-ray phase contrast tomography; proof of principle for post-mortem imaging *The British journal of radiology* 2016 89 (1058).

14. Bray, F., Ferlay, J., Soerjomataram, I. et al. Global Cancer Statistics 2018: GLOBOCAN Estimates of Incidence and Mortality Worldwide for 36 Cancers in 185 Countries. *Ca-Cancer J Clin* 2018 68 (6): 394-424.

15. Wild, C. P., Weiderpass, E., Stewart, B. W. *World Cancer Report: Cancer Research for Cancer Prevention.* 2020 Lyon, France: International Agency for Research on Cancer. http://publications.iarc.fr/586.

16. Siegel, R. L., Miller, K. D., Jemal, A. "Cancer Statistics, 2019. *Ca-Cancer J Clin* 2019 69 (1): 7-34.

17. Zeman, W., Curtis, H. and Baker, C. Histopathologic Effect of High-Energy-Particle Microbeams on the Visual Cortex of the Mouse Brain. *Radiation Research* 1961 15 (4): 496-514.

18. Fouillade, C., Curras-Alonso, S., Giuranno, L. et al. FLASH Irradiation Spares Lung Progenitor Cells and Limits the Incidence of Radio-induced Senescence. *Clin Cancer Res* 2020 26 (6).

19. Laissue, J. A., Bartzsch, S., Blattmann, H. et al. Response of the rat spinal cord to X-ray microbeams. *Radiother Oncol* 2013 106(1):106-111.

20. Schültke, E., Bayat, S., Bartzsch, S. et al. A mouse model for microbeam radiotherapy of the lung. *Int J Radiat Oncol* 2021 110(2): 521-525.

21. Barbone, G. E., Bravin, A., Romanelli, P. et al. Micro-imaging of Brain Cancer Radiation Therapy Using Phase-contrast Computed Tomography. *Int J Radiat Oncol* 2018 101 (4): 965-984.

22. XXXXXX

23. Mittone, A., Fardin, L., Di Lillo, F. et al. Multiscale pink-beam microCT imaging at the ESRF-ID17 biomedical beamline. *J Synchrotron Radiat* 2020 27: 1347-1357.

24. Regnard, P., Le Duc, G., Bräuer-Krisch, E., et al. Irradiation of intracerebral 9L gliosarcoma by a single array of microplanar x-ray beams from a synchrotron: balance between curing and sparing. *Phys Med Biol* 2008 35: 861-878.

25. Bräuer-Krisch, E., Requardt, H., Brochard, T. et al. New technology enables high precision multislit collimators for microbeam radiation therapy. *Rev sci instrum* 2009 80(7): 074301.

26. Stampanoni, M., Groso, A., Isenegger, A., Mikuljan, G., Chen, Q., Bertrand, A., Henein, S., Betemps, R., Frommherz, U., Böhler, P., Meister, D., Lange, M., Abela, R. Trends in synchrotron-based tomographic imaging: the SLS experience. *Spie 6318* 2006 199-212.

27. Stampanoni, M., Groso, A., Isenegger, A., Mikuljan, G., Chen, Q., Meister, D., Lange, M., Betemps, R., Henein, S. and Abela, R. TOMCAT: A beamline for TOmographic Microscopy and Coherent rAdiology experimenTs. *AIP Conference Proceedings*, 2007 879: 848-851.

28. Miettinen, A., Oikonomidis, I. V., Bonnin, A., Stampanoni, M. NRStitcher: non-rigid stitching of terapixel-scale volumetric images. *Bioinformatics* 2019 35(24): 5290-5297.

29. Lovric, G., Mokso, R., Arcadu, F. et al. Tomographic in vivo microscopy for the study of lung physiology at the alveolar level. *Sci Rep-UK* 2017 7 (1):12545.

30. Dreossi, D., Abrami, A., Arfelli, F., Bregant, P., Casarin, K., Chenda, V., Cova, M. A., Longo, R., Menk, R.-H., Quai. E., Quaia, E., Rigon, L., Rokvic, T., Sanabor, D., Tonutti, M., Tromba, G., Vascotto, A., Zanconati, F., Castelli, E. The mammography project at the SYRMEP beamline *European Journal of Radiology* 2008 68: 58-62.

31. Castelli, E., Tonutti, M., Arfelli, F., Longo, R., Quaia, E., Rigon, L., Sanabor, D., Zanconati, F., Dreossi, D., Abrami, A., Quai, E., Bregant, P., Casarin, K., Chenda, V., Menk, R. H., Rokvic, T., Vascotto, A., Tromba, G., Cova, M. A. Mammography with Synchrotron Radiation: First Clinical Experience with Phase-Detection Technique3. *Radiology*, 2011 259: 684-694.

32. Tanaka, T., Honda, C., Matsuo, S., Noma, K., Oohara, H., Nitta, N., Ota, S., Tsuchiya, K., Sakashita, Y., Yamada, A., Yamasaki, M., Furukawa, A., Takahashi, M., Murata, K. The First Trial of Phase Contrast Imaging for Digital Full-Field Mammography Using a Practical Molybdenum X-Ray Tube. *Investigative Radiology* 2005 40: 385-396.

33. Tanaka J, Nagashima M, Kido K, Hoshino Y, Kiyohara J, Makifuchi C, Nishino S, Nagatsuka S, Momose A. Cadaveric and in vivo human joint imaging based on differential phase contrast by X-ray Talbot-Lau interferometry. *Zeitschrift für Medizinische Physik* 2013 23: 222-227.

34. Yoshioka, H., Kadono, Y., Kim, Y. T., Oda, H., Maruyama, T., Akiyama, Y., Mimura, T., Tanaka, J., Niitsu, M., Hoshino, Y., Kiyohara, J., Nishino, S., Makifuchi, C., Takahashi, A., Shinden, Y.,

Matsusaka, N., Kido, K., Momose, A. Imaging evaluation of the cartilage in rheumatoid arthritis patients with an x-ray phase imaging apparatus based on Talbot-Lau interferometry. *Scientific Reports*, 2020 10.

35. Yaroshenko, A., Hellbach, K., Yildirim, A. Ö., Conlon, T. M., Fernandez, I. E., Bech, M., Velroyen, A., Meinel, F. G., Auweter, S., Reiser, M., Eickelberg. O., Pfeiffer, F. Improved In vivo Assessment of Pulmonary Fibrosis in Mice using X-Ray Dark-Field Radiography. *Scientific reports* 2015 5.

36. Hellbach, K., Yaroshenko, A., Meinel, F. G., Yildirim, A. Ö., Conlon, T. M., Bech, M., Mueller, M., Velroyen, A., Notohamiprodjo, M., Bamberg, F., Auweter, S., Reiser, M., Eickelberg, O., Pfeiffer, F. In Vivo Dark-Field Radiography for Early Diagnosis and Staging of Pulmonary Emphysema. *Investigative Radiology* 2015 50 (7): 430-435.

37. Willer, K., Fingerle, A., Noichl, W. De Marco, F. Frank, M. Urban, T. Schick, R. Gustschin, A. Gleich, B. Herzen, J. Koehler, T. Yaroshenko, A. Pralow, T. Zimmermann, G. Renger, B. Sauter, A. Pfeiffer, D. Makowski, M. Rummeny, E. Grenier, P., Pfeiffer, F. X-ray Dark-Field Chest Imaging can Detect and Quantify Emphy-sema in COPD Patients. *medRxiv* 2021.01.15.21249798 2021.

Figures and Tables captions

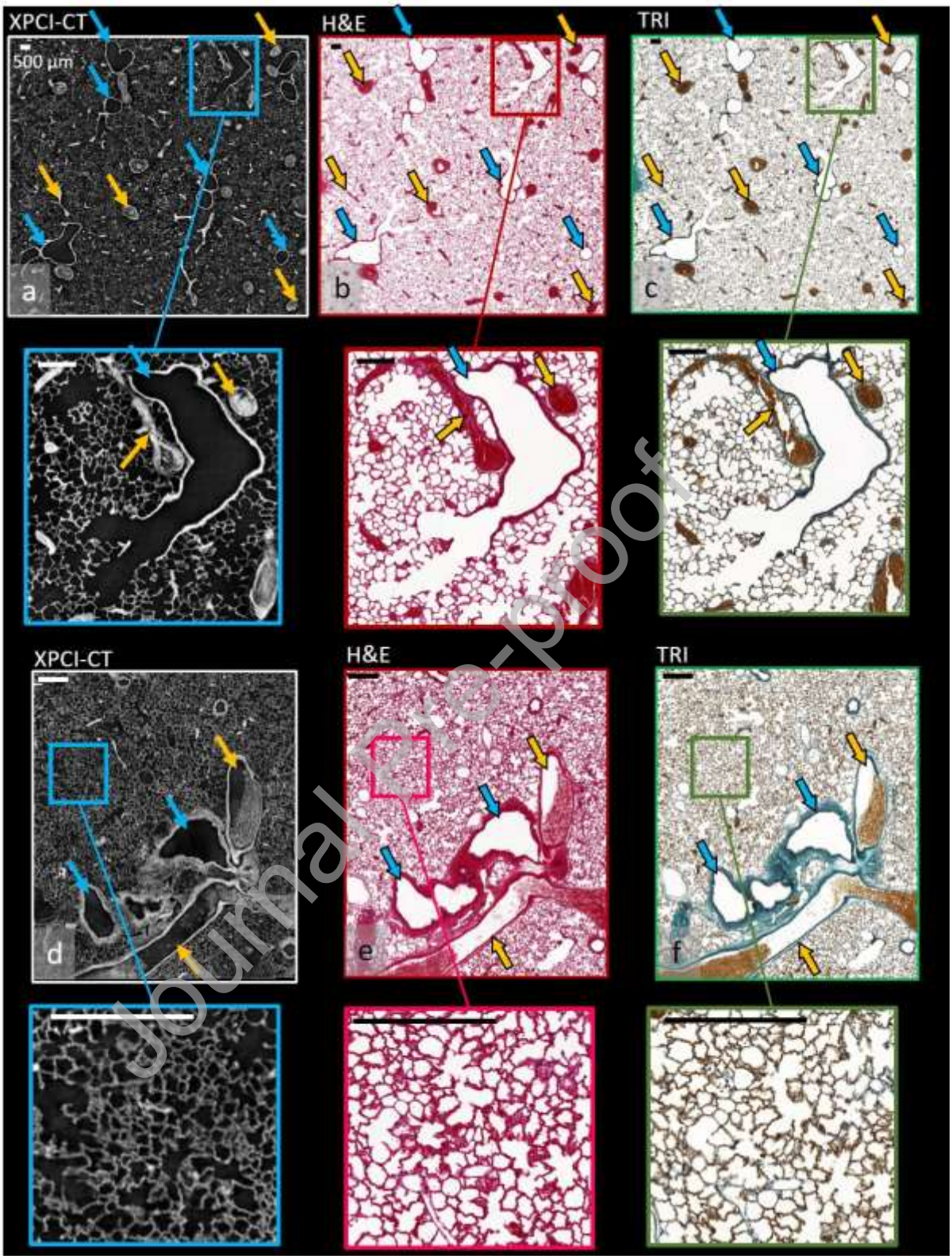

Figure 1: *XPCI-CT images at 1.63^3 µm^3 voxel size and histologic comparison for two control, untreated, healthy lungs. Sky-blue arrows point at the airways while yellow arrows indicate the filled blood vessels. (a)-(c) are a portion of a 3x3 stitched, 1.63^3 µm^3 – voxel XPCI-CT coronal image displaying vessels and airways of different dimensions on a regular alveolar pattern, the correspondent H&E and TRI histologic slices. Each inset shows, in a magnified view, the development of the*

bronchioles and the transversal views of capillaries. (d)-(f) represent another healthy sample in a portion of a 4x2 stitched, 1.63^3 µm^3 – voxel XPCI-CT coronal image, H&E and TRI histologic stainings. Here the entanglement of a big blood vessel and an airway is shown, while the insets zoom in the regular alveolar pattern of the sample. This figure allows the validation of the XPCI-CT signal for alveoli, blood vessels and bronchi.

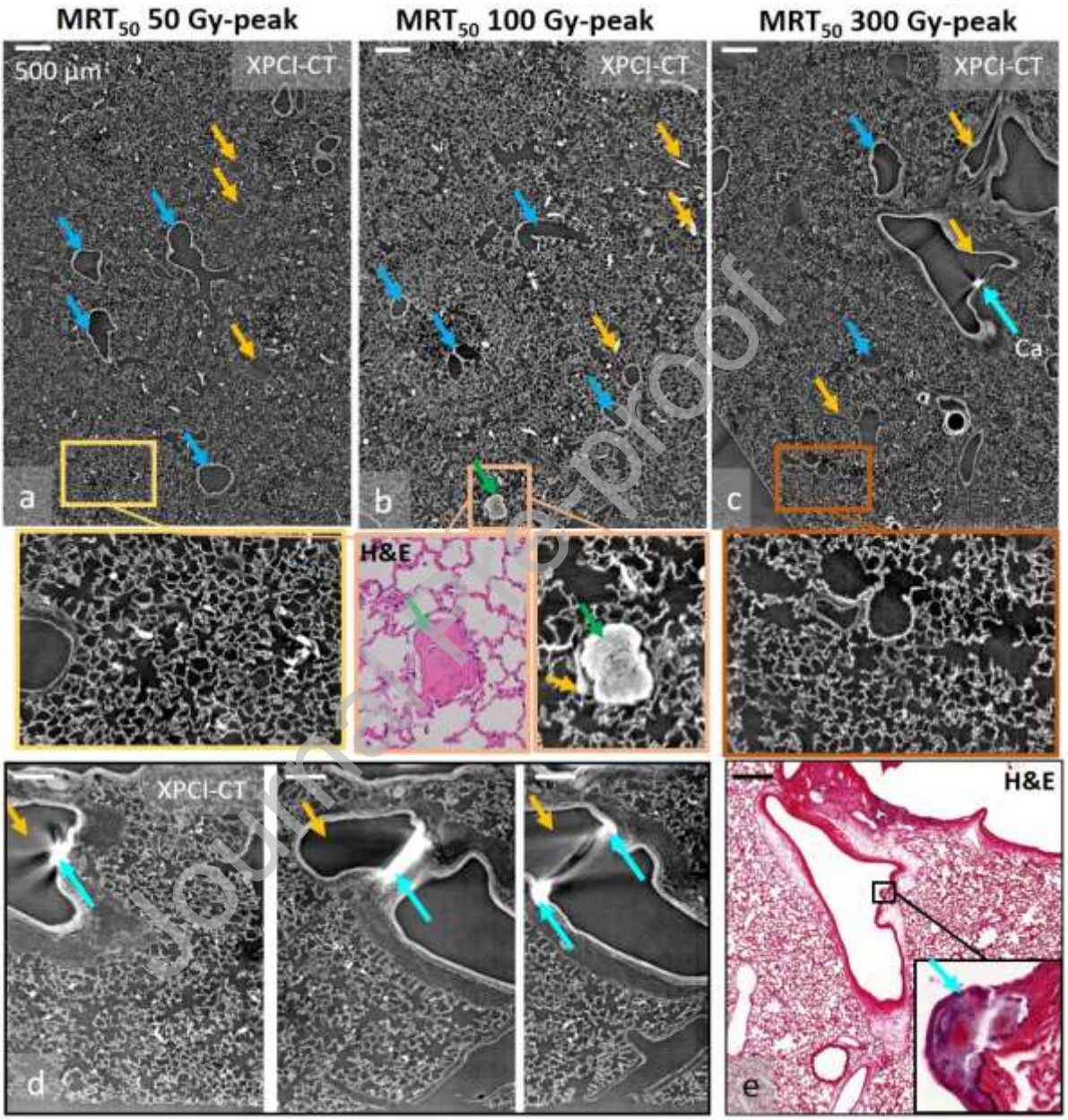

Figure 2: *MRT$_{50}$ irradiated samples with 50, 100 and 300 Gy as peak dose imaged at 1.63^3 µm^3 voxel size. Subfigure (a), (b) and (c) show portions of a stitched, 1.63^3 µm^3 – voxel XPCI-CT coronal image of MRT$_{50}$ 50, 100 and 300 Gy-peak dose samples respectively. The tissue structures of the three samples are comparable with the healthy ones, exception made for a specific feature for the last two ones. The insets of each figure show a normal alveolarization in all the cases and a collagen nodulus found in the 100 Gy-dose peak sample pointed by a green arrow and validated with its respective H&E*

histology. The blood vessel, it is entangled with, is indicated with a yellow arrow. The inset of (c) reports the replacement of a portion of endothelium by a calcification. (d) shows the same feature at three different depths on the sagittal plane. The H&E histology in (e) confirms that the structure found in (c) is a calcium deposit produced by the radiation having targeted a blood vessel. Cyan arrows indicate the calcification, yellow and sky-blue ones are for the blood vessels and airways.

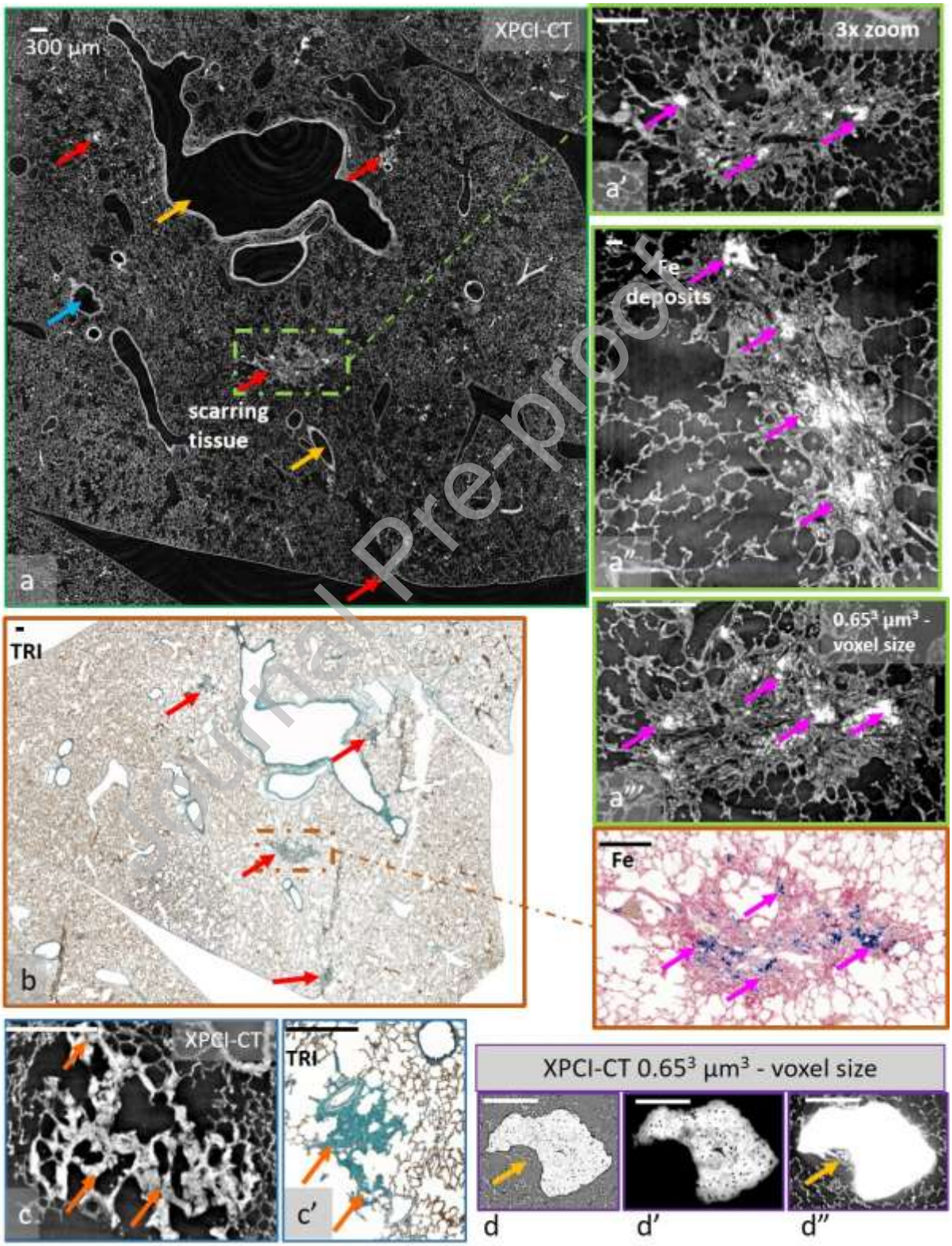

Figure 3: *MRT_{50} treated rat with 600 Gy as peak dose. All the CT images are taken with 1.63^3 μm^3 voxel size, if not differently specified. (a) is a 3x3 stitched, 1.63^3 μm^3 – voxel XPCI-CT coronal image: the tissue has only few signs of the irradiation as isolated scars indicated by the red arrows. The central scar englobes some hyperdense structures as shown in the 3x zoom in (a") and pointed out by the magenta arrows in its 3x zoom (a'), reslice along the axial plane (a") and a 0.65^3 μm^3 voxel size coronal image of the same scar at a different. The Masson-Goldner trichrome (TRI) histology (b) of the same lung tissue area of (a) shows collagen structures, and thus fibrotic tissue, where XPCI reveals scars. Its inset is a Fe-stained histology labelling the hyperdense structured detected by XPCI-CT images as Fe deposits. (c) reports the thickening of the alveolar walls as confirmed by the Masson-Goldner trichrome histology (c') while (d), (d') and (d") are respectively the reconstruction in absorption mode and XPCI-CT with two different grey scale windowing of a collagen nodulus, where the small dark spots are cells or cluster of cells. Sky-blue and yellow arrows are for the airways and blood vessels.*

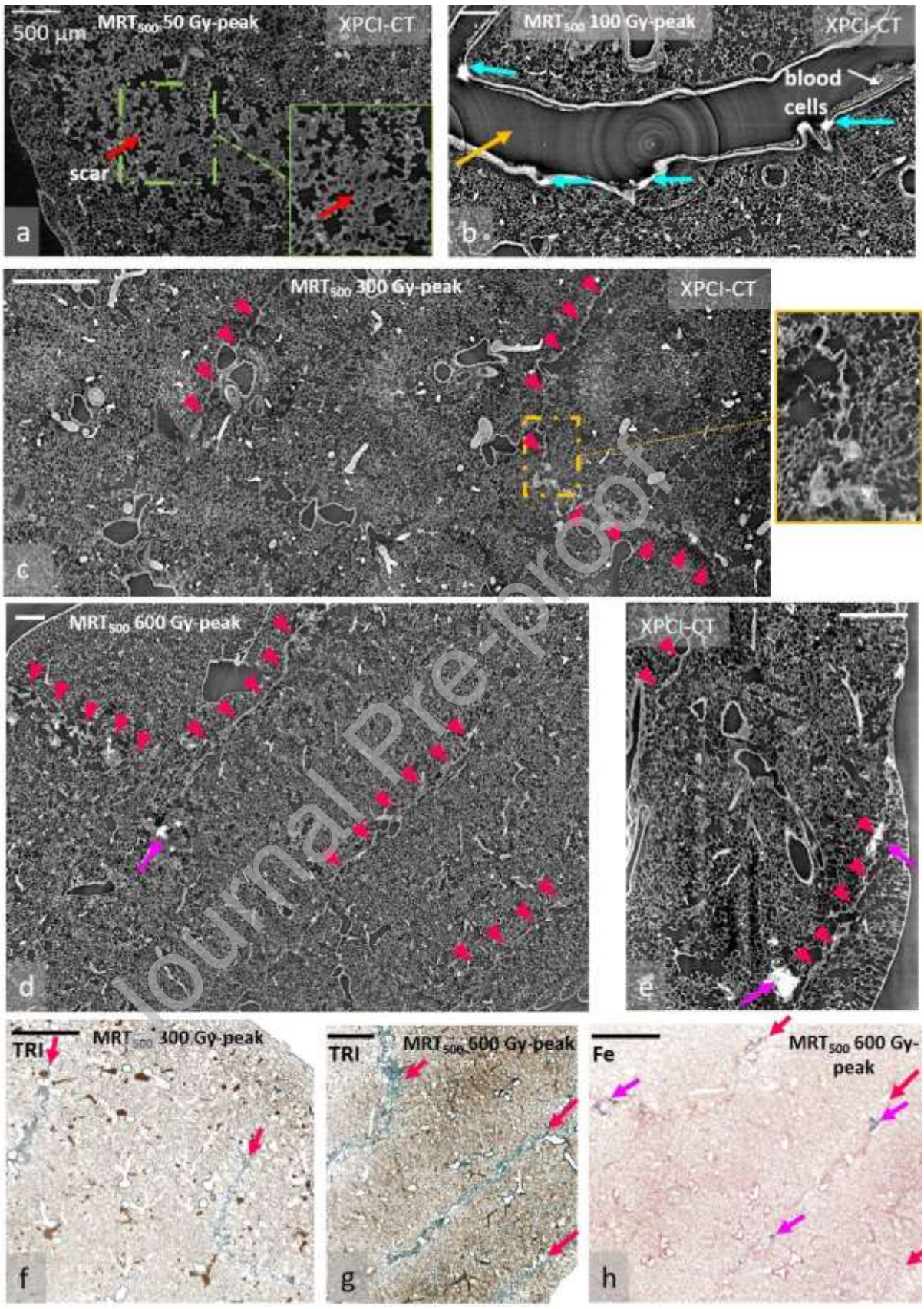

Figure 4: *MRT_{500} treated samples. (a) is a portion of a 6x4 stitched, 1.63^3 μm^3 – voxel XPCI-CT coronal image of a MRT_{500} 50 Gy irradiated sample. The red arrow indicates an extended scar on the tissue and its 2x zoom in the inset better shows the*

thickening of the alveoli septa. The calcifications of a blood vessel caused by a 100 Gy-peak microbeam on the epithelium layer is reported in (b) on a portion of a 4x3 stitched, 1.63^3 μm^3 – voxel XPCI-CT coronal image. Each calcification is pointed put by a cyan arrow indicating the direction of the beam delivery. The white arrow shows some blood cells left inside the vessel. (c) is a portion of a 2x4 stitched, 1.63^3 μm^3 – voxel XPCI-CT coronal image of an MRT_{500} 300 Gy treated lung showing two of the three microbeam paths as stripe-shaped scars. The 3x zoom inset is a magnification of the scarring tissue produced by a 500 µm-wide microbeam. (d) depicts a MRT_{500} 600 Gy treated sample with a 3x2 stitched, 1.63^3 μm^3 – voxel XPCI-CT coronal image where the three MRT_{500} paths are visible; (e) is its oblique reslice that clarifies how the scars develop in depth throughout the sample. Some Fe contents are visible and indicated by a magenta arrow. The amaranth arrowheads are placed next to the stripe-scars to help their visualization. (f) and (g) are the TRI histology of the XPCI-CT images of (c) and (d), respectively, confirming the presence of fibrotic tissue in the scars. (h) validates the presence of intra-scar Fe deposits in the MRT_{500} 600 Gy-peak dose treated sample.

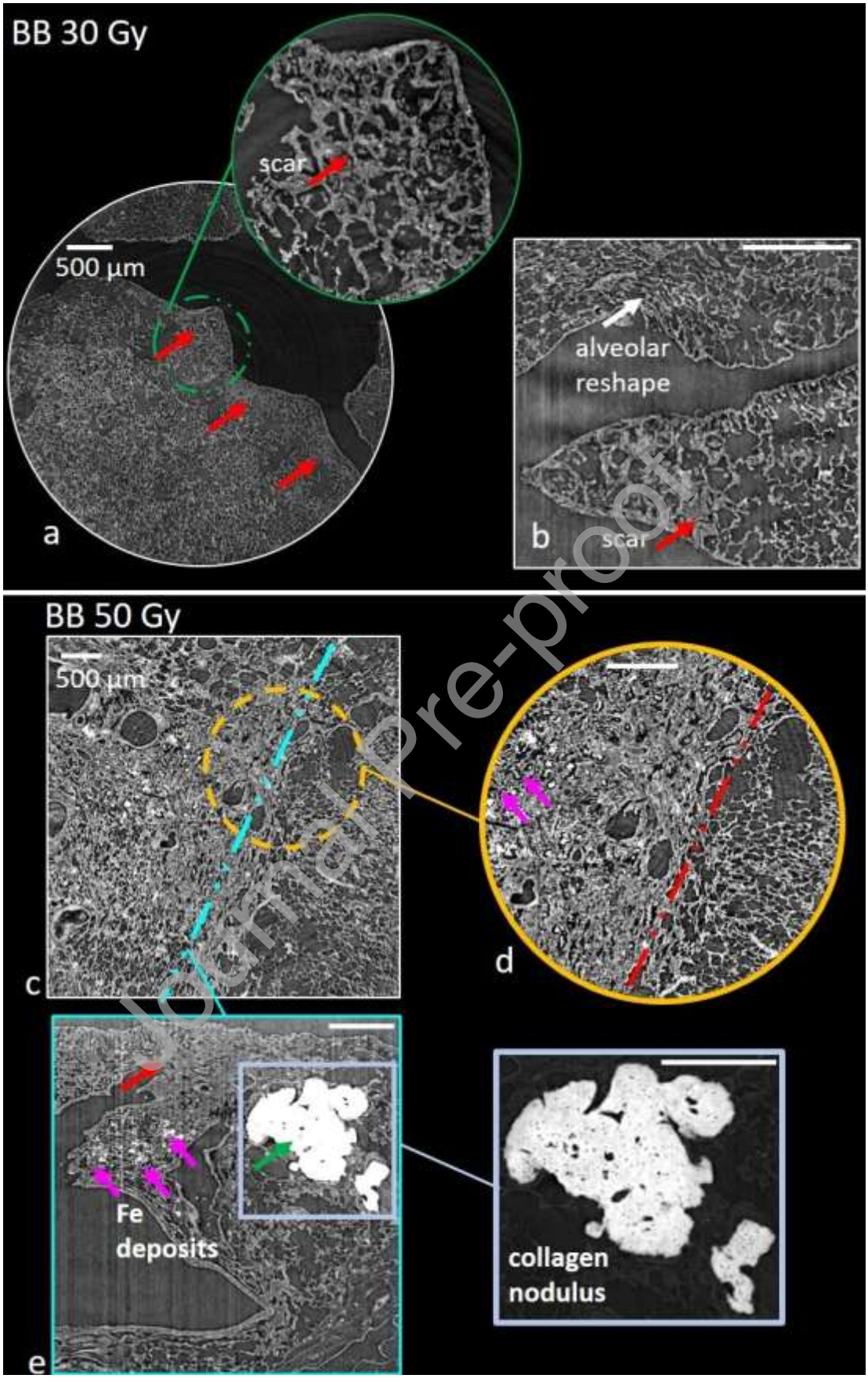

Figure 5: *BB irradiated lungs imaged at 1.63^3 μm^3 voxel size. The subfigures show (a) the coronal and (b) the sagittal views of a BB 30 Gy irradiated sample. The scarring tissue is pointed out by the red arrows and emphasized in the 3x zoomed inset, while the white arrow indicates a general alveolar rearrangement. In the 50 Gy irradiated sample (c), a sharp discontinuity between irradiated and not irradiated tissue is visible. The 2x zoom (d) goes into the details of the edge between the two zones, which is identified by the red dashed line, and of the presence of Fe deposits indicated by the magenta arrows. (e) is the reslicing of (c) along the cyan line and reveals the presence of a collagen nodulus (green arrow), fibrotic tissue (red arrow) and several Fe deposits distributed in depth (magenta arrows). The collagen nodulus is reported in the inset of (e) with a different grey scale windowing to reveal its inner structure.*

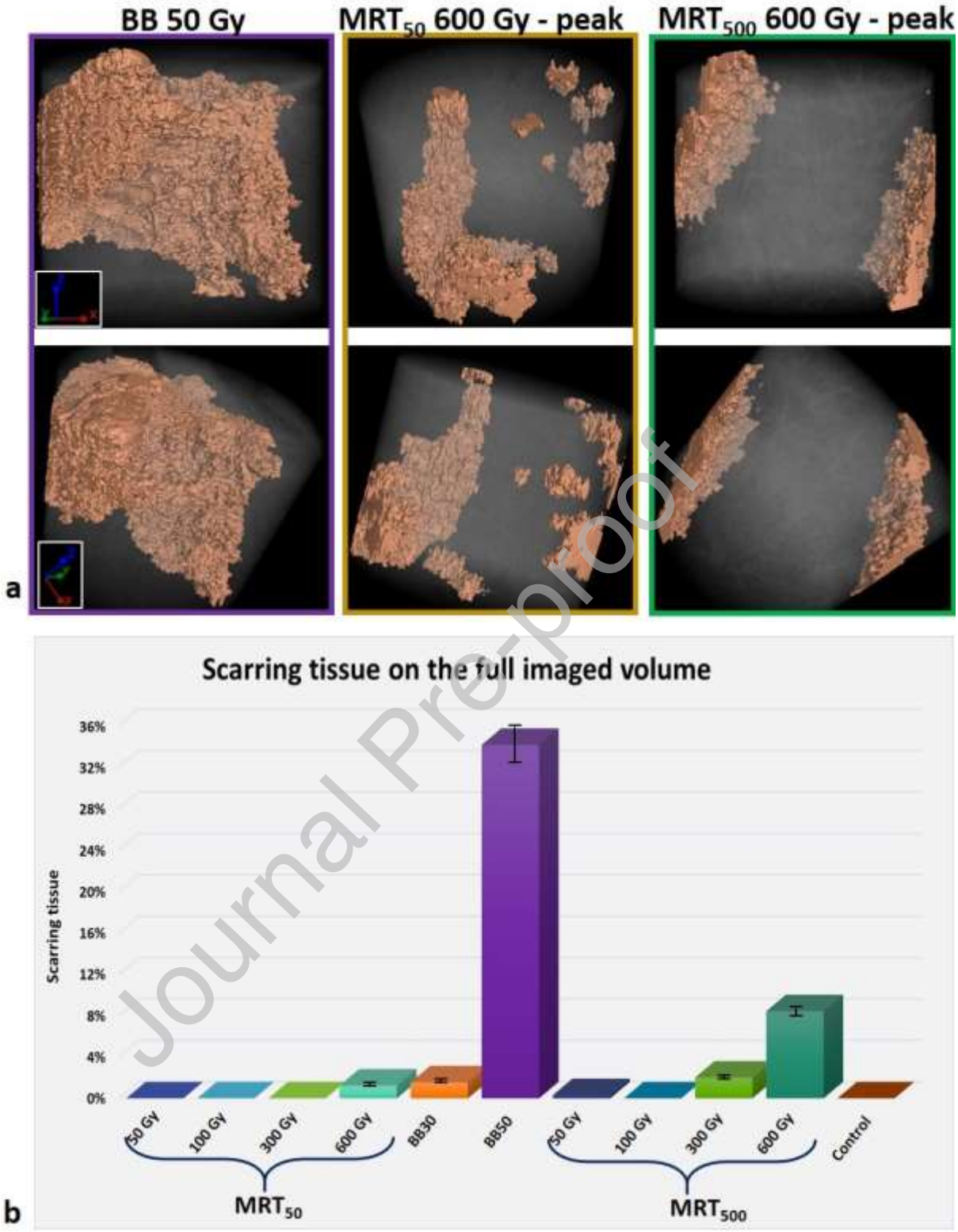

Figure 6: *scarring tissue 3D representation and graph of the total fibrotic tissue quantification for a representative sample for each radiotherapy protocol. (a) 3D rendering of BB 50 Gy, MRT_{50} and MRT_{500} 600 Gy-peak dose lung specimens showing how the fibrotic tissue is distributed within the imaged lung portions for the different cases. The fibrotic content is displayed as solid and coloured feature, while the rest of the sample is shown in a transparent grey modality. BB only produces one extended clustered scar, MRT_{50} treated lung shows isolated small scars while for the MRT_{500} specimen the planar shape of*

the fibrotic tissue is visible. (b) reports the total amount of segmented fibrotic tissue as a percentage of the total available volume. One representative sample was chosen for each group to build the graph. Errors were assessed by repeating the segmentation for one sample per each RT geometry (BB, MRT_{50} and MRT_{500}) for three times during different days. The error was estimated to be the 5% of the segmented volume in all cases.

***Table 1**: irradiation parameters for Broad Beam (BB) and Microbeam Radiation Therapy (MRT). MRT50 and MRT500 are used to distinguish between the two MRT beamlets widths, which are 50 and 500 µm, respectively.*

Group name	Beamlets' width (µm)	Centre to centre distance (µm)	Peak dose (Gy)	Valley dose (Gy)
BB30	--	--	30	--
BB50	--	--	50	--
MRT_{50}	50	400	50	1.2
	50	400	100	2.4
	50	400	300	7.3
	50	400	600	14.6
MRT_{500}	500	4000	50	0.7
	500	4000	100	1.3
	500	4000	300	4.0
	500	4000	600	7.9
Control	--	--	--	--